Aalto University
School of Engineering

Atte Korhonen

A method for estimating ice phenology of Finnish waterbodies using Sentinel-1 IW mode data and in-situ wind observations

Master's thesis
Department of Built Environment
School of Engineering

Espoo, Finland 24.11.2018

Supervisor: Professor Miina Rautiainen
Advisor: D.Sc. (Tech.) Sari Metsämäki

Aalto University
School of Engineering

Aalto-university, P.O. 11000, 00076 AALTO
www.aalto.fi
Abstract of master's thesis

Author Atte Korhonen

Title of thesis A method for estimating ice phenology of Finnish waterbodies using Sentinel-1 IW mode data and in-situ wind observations

Degree Programme Master's Programme in Geoinformatics

Thesis supervisor Professor Miina Rautiainen

Thesis advisor(s) Doctor of Science (Tech.) Sari Metsämäki

Date 24.11.2018 **Number of pages** 91 + 5 **Language** English

Abstract

The subject of this thesis was to find a method for determining ice phenology, or ice freeze-up and break-up dates, in Finnish waterbodies using Sentinel-1 C-band synthetic aperture radar images. The method should minimize manual steps to make it suitable for automatic processing. Though possibilities for detecting these changes are presented by optical earth observation satellites, optical images are often limited by cloud cover and darkness over autumn-winter months in the northern hemisphere. A great advantage of synthetic aperture radars as active sensors is their capability to penetrate through cloud cover and their independence of sunlight to operate. For specific advantages of the Sentinel-1 constellation, data is gathered with a very high acquisition rate near polar regions and all data is openly accessible since 2014.

As this thesis is written, few studies have been conducted on observing inland waterbodies' ice using Sentinel-1 IW mode radar images. To gather data from local wind conditions, lake water / ice / snow surface and temperatures in preparation for the thesis to determine and develop the final method, an automatic sensor station was built to a lake shoreline in southern Finland.

The method developed and presented in this thesis is based on the similarity of Sentinel-1 IW mode radar images produced by water surface waves in similar wind conditions. By classifying radar images using similar wind conditions determined by weather station measurements, then estimating a numerical value for the difference between the radar images, waterbodies with open water will feature higher similarity with each other than frozen waterbodies with open water. The difference in similarity is used to determine the dates when changes in ice phenology, freeze-ups and ice break-ups, occur.

Calculated by the method, lake freeze-up and break-up periods were determined to be accurate to within few satellite flyovers for select four lakes of different sizes in southern Finland which included the lake with the sensor station. For river portions few hundred meters wide and long, the method was found to distinguish changes in ice phenology for inland river portions better than portions near the sea discharge location. As the method could be used for estimating ice phenology for a variety of waterbodies in Finland not being routinely observed, it will offer possibilities in expansion of freeze-up and break-up models for such waterbodies. There are also potential applications for other watershed models, as seasonal ice can affect certain types of data used to calibrate these models.

Keywords Remote sensing, lake ice phenology, Sentinel-1, IW mode, SAR

Aalto-yliopisto
Insinööritieteiden korkeakoulu

Aalto-yliopisto, PL 11000, 00076 AALTO
www.aalto.fi

Diplomityön tiivistelmä

Tekijä Atte Korhonen

Työn nimi Menetelmä Suomen vesistöjen jääfenologian määrittämiseen perustuen Sentinel-1 IW -moodin satelliittidatan yhdistämiseen tuulennopeusmittauksiin

Koulutusohjelma Master's Programme in Geoinformatics

Työn valvoja Professori Miina Rautiainen

Työn ohjaaja(t) Tekniikan tohtori Sari Metsämäki

Päivämäärä 24.11.2018 **Sivumäärä** 91 + 5 **Kieli** Englanti

Tiivistelmä

Tämän diplomityön aiheena on löytää ja kehittää menetelmä Suomen sisävesistöjen jäätymis- ja sulamisajankohtien määrittämiseen hyödyntämällä Sentinel-1 C-taajuuden tutkasatelliittien keräämää dataa. Optisia satelliittikuvia voidaan käyttää jääfenologian määrittämisessä, mutta ovat pohjoisessa rajoittuneita etenkin loppuvuoden jäätymisajankohtien määrittämisessä johtuen pilvisyydestä sekä pimeydestä. Synteettisen apertuurin tutka (engl. SAR) on aktiivinen sensori mikä kykenee toimimaan ilman auringonvaloa sekä pilvipeitteiden läpi. Jääfenologian määrittämisen osalta Sentinel-1 tutkasatelliitit hyötyvät lisäksi korkeasta ylilentotaajuudesta pohjoisilla alueilla sekä vuodesta 2014 asti kerätystä avoimesti saatavilla olevasta tutkakuva-arkistosta.

Työn kirjoitushetkellä tutkimuksia Sentinel-1:n IW -moodin tutkahavaintojen hyödyntämisestä sisävesistöjen jääfenologian tulkinnassa ei ole juurikaan laadittu. Tästä syystä työn yhteydessä on rakennettu mittausasema Etelä-Suomessa sijaitsevan järven rantaan, jonka kautta erilaisten menetelmien kehittämiseen vaadittavaa tietoa on kerätty sekä vaihtoehtoja karsittu johtaen nykyiseen versioon menetelmästä. Tässä diplomityössä esitetty menetelmä hyödyntää vesistöjen aaltojen samankaltaisuutta kun tuuliolosuhteet ovat vesistön osalta liki identtiset. Kun tutkakuvassa sulaa vesistöä samoissa tuuliolosuhteissa verrataan sulaan vesistöön, ne eroavat vain vähän toisistaan ja vastaavasti jäätynyt vesistö eroaa tyypillisesti sulasta vesistöstä. Tuuliolosuhteiden samankaltaisuus määritetään hyödyntämällä Ilmatieteen laitoksen sääasemien tuulihavaintoja.

Menetelmällä määritettiin jäätymis- ja sulamisajankohdat neljälle järvelle Etelä-Suomessa mukaanlukien sensoriaseman mittaama järvi. Vertaamalla ajankohtia saatavilla oleviin manuaalisiin havaintoihin, menetelmä määritti ajankohdat oikein muutaman satelliittin ylilennon tarkkuudella. Menetelmän soveltuvuus muutaman sadan metrin pituisille ja leveille jokiosuuksille todettiin olevan parempi sisämaassa kuin sijainnissa jossa joki laskee mereen. Menetelmän todettiin tarjoavan mahdollisuuksia sellaisten sisävesistöjen jääfenologian seurantaan joissa jäätymis- ja sulamisajankohtaa ei mitata, tarjoten dataa kyseisten vesistöjen jääolojen mallintamiseen. On myös mahdollista että vesistömalleissa voidaan hyödyntää tietoa jääfenologiasta, koska kausiluontoinen jää vaikuttaa muunmuassa näiden mallien kalibroinnissa käytettyihin mittauksiin.

Avainsanat Kaukokartoitus, jääfenologia, Sentinel-1, IW-moodi, SAR

Table of Contents

Abstract
Tiivistelmä

Table of Contents 4
Abbreviations 6
1 Introduction 7
  1.1 Motivation 7
  1.2 Objectives of the study 7
    1.2.1 General objective 7
    1.2.2 Specific objectives 7
    1.2.3 Research questions 8
    1.2.4 Hypotheses 8
2 Literature review 9
  2.1 Inland waterbodies in Finland 9
    2.1.1 Overview of different Finnish waterbodies 9
    2.1.2 Freshwater lake and river phenology 10
    2.1.3 Ice phenology observations in Finland 12
    2.1.4 Ice phenology modelling 14
    2.1.5 Waterbody areas and DEMs available for Finland 15
  2.2 Wind and waves in waterbodies 16
    2.2.1 Water surface waves 16
    2.2.2 Wind-wave interaction in waterbodies 18
    2.2.3 Wind and rain radar measurements in Finland 21
  2.3 Spaceborne radar 21
    2.3.1 Synthetic Aperture Radars 21
    2.3.2 Radar signal backscattering 24
    2.3.3 SLC conversion to GRD 27
    2.3.4 Common processing steps for GRD-products 29
    2.3.5 Water, ice and snow backscattering on C-band 32
    2.3.6 Methods for classifying lake ice in C-band SAR data 35
    2.3.7 Copernicus Sentinel-1 mission, the related products and applied tools ... 37
3 Methodology 40
  3.1 Overview of the study area, waterbodies and used data 40
    3.1.1 Overview of meteorological data used for the studied waterbodies 41
    3.1.2 Regarding the selection of IW-mode over EW-mode 42
  3.2 Ice phenology measurements at lake Pannujärvi 43
    3.2.1 Background and system overview 43
    3.2.2 Timeline on ice phenology events of lake Pannujärvi 47
    3.2.3 Wave similarity in similar wind conditions at lake Pannujärvi 48
  3.3 Data pre-processing 51
    3.3.1 DEM and Jarvi-10 polygon preparation 51
    3.3.2 Pre-processing Sentinel-1 data 52
    3.3.3 In-situ weather data 54
    3.3.4 Accumulating degree-day calculations 55
  3.4 Calculating lake phenology from pre-processed data 55
    3.4.1 Wind raster to a similarity matrix for each waterbody 55
    3.4.2 Converting VV-polarity sigma0 rasters to similarity matrices 57
    3.4.3 Calculating similarity value in comparison to open water 59
    3.4.4 Using similarity values to determine ice phenology dates 61

4 Results 64
  4.1 Lake study area 64
    4.1.1 Lake Pääjärvi 65
    4.1.2 Lake Suolijärvi 68
    4.1.3 Lake Pannujärvi 69
    4.1.4 Lake Lovojärvi 71
    4.1.5 FDD and TDD comparison for each ice year 72
  4.2 River study area 73
    4.2.1 Portion A 74
    4.2.2 Portion B 75
5 Discussion 77
  5.1 Outliers in results of studied lakes 77
  5.2 Differences in the two river portions 79
  5.3 Identifying limitations and improvements of the method 79
  5.4 Advantages and potential applications of the method 82
6 Conclusion 85
7 References 86
List of appendices 91

Appendices

Abbreviations

AC	Alternating Current
CLIME	Climate and Lake Impacts in Europe
DC	Direct Current
DEM	Digital Elevation Model
ERS	European Remote Sensing
ESA	European Space Agency
ESA PDGS	ESA Payload Data Segment
ESA SNAP	ESA Satellite Application Platform
EW-mode	Extra Wide Mode
FDD	Freezing Degree-Days
FMI	Finnish Meteorological Institute
FOV	Field of View
GLAWEX´97	Great Lakes Winter Experiment ´97
GMES	Global Monitoring for Environment and Security
GNSS	Global Navigation Satellite System
GPS	Global Positioning System
GRD	Ground-Range Detected
GRS-80	Geodetic Reference System 1980
H	Horizontal
HIGHTSI	High-Resolution Thermodynamic Snow and Sea-Ice Model
HIRLAM	High-Resolution Limited Area Model
InSAR	Interferometric Synthetic Aperture Radar
IW-mode	Interferometric Wide Mode
LFM	Linear Frequency Modulation
NLS	National Land Survey of Finland
NRT	Near Real Time
NTC	Non Time Critical
OCN	Ocean Mode
S-1	Sentinel-1
S1TBX	Sentinel-1 Toolbox
SAR	Synthetic Aperture Radar
SLC	Single-Look Complex
SNR	Signal to Noise Ratio
SYKE	Suomen Ympäristökeskus (Finnish Environment Institute)
TDD	Thawing Degree-Days
TOPS	Terrain Observation with Progressive Scans
V	Vertical
WGS84	World Geodetic System 1984

1 Introduction

1.1 Motivation

Ice phenology means studying the timing of ice freeze and breakup for waterbodies. These two in combination indicate the ice cover duration of the waterbody. Long records of ice phenology, going as far back as 17th century in Finland, are useful indicators of monitoring climate change and understanding the various underlying processes in freezing and thawing of waterbodies. Accurate freeze-up and break-up date observations of seasonal ice are useful for creating and improving modelling and monitoring of ice phenology and ice thickness, in addition to having practical applications for river flood forecasting.

As compared to traditional manual observations of ice phenology, recent years have introduced new possibilities using data provided by Earth observing satellites. Optical satellites such as NASA Landsat's and the new ESA Sentinel-2's are capable of ice monitoring applications but may be limited by clouds and lack of sunlight, as compared to spaceborne synthetic aperture radars as active sensors not featuring such limitations. With various applications in high latitudes such as the mapping of sea ice for sea routes, use of radar images for classifying sea-, glacial- and polar ice has been studied extensively. Fewer studies have however been conducted on classifying seasonal inland waterbody ice in lakes and rivers, especially for the new ESA Sentinel-1 constellation Interferometric Wide swath mode data.

The focus of this work is to find a method for estimating the freeze-up date and break-up date of ice using Sentinel-1 data. This method would use the full extent of Sentinel-1 radar images at its spatial and temporal coverage, and the developed method would feature minimal number of manual steps to enable potential future development of a version capable of more scalable use. Due to Sentinel-1 Extra Wide swath mode's acquisition coverage being less optimal for inland study areas in Finland and the lower resolution being not usable for small to very small waterbodies, Interferometric Wide mode was chosen for the research at an early stage.

Using the developed method, a few selected waterbodies from southern Finland including both lakes and river areas are studied. The method-acquired dates of freeze-up and break-up of ice are compared to manual observations where applicable, and accumulated sums in thawing degree days and freezing degree days are calculated for each waterbody for comparison when and where manual observations are not available. The overall suitability for different waterbodies is assessed while listing features inherent to the used method and its potential limitations.

1.2 Objectives of the study

1.2.1 General objective

The general objective of this thesis is to assess the potential of Sentinel-1 SAR-imagery for inland waterbody ice phenology monitoring using a newly developed method of utilizing radar image similarity in similar wind conditions during open water period.

1.2.2 Specific objectives

- Measuring lake ice phenology dates accurately for a single lake with using a sensor station

- Using the sensor station data for identifying similarities in lake waves during similar wind conditions
- Developing and documenting a method to study the similarity in wind conditions to use it for ice phenology assessment
- Applying the method for various waterbodies in southern Finland, including river portions and lakes of different sizes
- Comparing the findings to air temperatures and ice phenology observations available for the studied waterbodies and assessing the usability of the method

1.2.3 Research questions

- How accurately can the method be used to calculate freeze-up and break-up dates of waterbodies different in size, shape and type?
- What factors may negatively impact the accuracy the method, and how the method could be improved?
- What are the advantages and disadvantages of the method as compared to alternative ways to determine waterbody ice phenology?
- How could the method be used in practical applications?

1.2.4 Hypotheses

- Similarities in local wind conditions can be estimated with non-local wind measurements for waterbodies using a network of weather stations
- Wave conditions in waterbodies are repeated each time a similar wind conditions are reached
- Similarities in near-identical waterbody wave conditions are non-discernible in corresponding radar images but discernible in close-to-similar waterbody wave conditions
- The lack of similarity in radar images between open water and frozen water in near-identical wind-wave conditions can be used to distinguish changes in ice phenology

2 Literature review

2.1 Inland waterbodies in Finland

2.1.1 Overview of different Finnish waterbodies

Finland has a variety of different freshwater waterbodies, the largest of which by area and water volume are rivers and lakes. Most Finnish lakes have been formed into bedrock-reservoirs carved by continental ice or into depressions formed between moraine formations and eskers. Some lakes near the shorelines are former sea gulfs engulfed by the post-ice age land rise (Helminen 1977). Lakes are generally defined as having a diameter of more than 200 meters, with smaller waterbodies that are not defined as rivers with a diameter of 10 – 200 meters being called ponds or lakelets and smaller than 10 meters being called puddles (Helminen 1977).

The average depth of the lakes in Finland has been determined to be around 7 meters, resulting in a total volume of water being only around 230 km^3. For comparison, the largest lake in Sweden called Vänern has a water volume of around 150 km^3 (Helminen 1977). A broad categorization of lakes by their area from the study of Raatikainen et al. (1990) is found in table 2. It is to be noted that despite the high number of very small lakes, such as having an area of less than 0.01 km^2, their total area is only a fraction of the total area of the 50 largest lakes with areas of 100 km^2. There are three lakes in total exceeding an area of 1000 km^2 in Finland (Raatikainen & Kuusisto 1990). The latest official estimation of the percentage of the total area covered in Finland by lakes is around 9.4% of the total area 31 600 km^2, with Finnish lake water being generally humic and slightly acidic (Kettunen et al. 2008).

Table 1 *Finnish lakes divided to categories by their areas (Raatikainen & Kuusisto 1990).*

Lake size in km^2	*Amount*	*Total area of the lakes km^2*
> 1000	3	3 303
100-1000	44	10 825
10-100	279	7 227
1.0-10	2 283	5 703
0.1-1.0	13 114	3 934
0.01-0.1	40 309	1 330
0.0005-0.01	131 876	341

Lakes are often broadly categorized by their lateral and vertical dimensions – or their diameter and depth (Leppäranta 2015). The category "medium deep" is generally not used. The categories are shown in table 2.

Table 2 *Lake categorization by diameter and average depth (Leppäranta 2015).*

Lateral (diameter) class	Very large	Large	Medium	Small	Very small
Lateral size	1 000 km	100 km	10 km	1 km	100 m
Vertical (depth) class	Very deep	Deep		Shallow	Very shallow
Vertical size	1 000 m	100 m		10 m	1 m

By official specifications in Finland (Vesilaki 2011), a river is a flowing body of water with a watershed area of at least 100 km^2. A flowing waterbody with a watershed area between 10 – 100 km^2 is a streamlet and even smaller flowing waterbodies are called rills. By additional definitions related to rivers in the Finnish nature dictionary written by Helminen (1977), portions of rivers with a relatively steep gradient has caused turbulence and higher than average water velocity are called rapids. River basins are areas defined by the specific river into which the water from the area ultimately flows into and later discharges to a larger river, a lake or the sea (Helminen 1977). The largest river basins in Finland by their river basin surface area are shown in table 3.

Table 3 *Ten largest river basins by surface area in Finland (Ekholm 1992).*

River basin	*Surface area in km^2*	*Lake percentage of the basin*	*Discharges to*	*Mean flow m^3/s 1961-1990, (location)*
Vuoksi	68 501	19.8	Lake Ladoga	596 (Tainionkoski)
Kemijoki	51 127	4.3	Bothnian Bay	553 (Isohaara)
Tornionjoki	40 131	4.6	Bothnian Bay	387 (Karunki)
Kymijoki	37 159	18.3	Gulf of Finland	300 (Anjala)
Kokemäenjoki	27 046	11.0	Bothnian Sea	231 (Harjavalta)
Oulujoki	22 841	11.5	Bothnian Bay	259 (Merikoski)
Teno	14 891	3.1	Arctic Ocean	177 (Alaköngäs)
Paatsjoki	14 512	12.4	Arctic Ocean	153 (Kaitakoski)
Iijoki	14 191	5.7	Bothnian Bay	181 (Raasakka)

2.1.2 Freshwater lake and river phenology

Lakes are found in all climate zones, with the possibility of freezing defined by both the climate and the lake features. In cold climate zone, of which Finland is part of, freshwater lakes freeze in normal years. The cold climate zone is determined as an area where average temperatures being below zero Celsius during January in the northern hemisphere, and July in the southern hemisphere (Leppäranta 2015). Seasonal freshwater ice is formed over winters in inland waterbodies but will melt over summer, and several cycles of seasonal ice freeze-up and break-up can occur when temperature fluctuates below and above 0 °C (Leppäranta 2015). Though not present in Finland, multi-year or in other words perennial freshwater lake ice can be encountered in high elevations and near the poles and is formed when first-year ice survives over a summer and gains thickness in the following winters, eventually becoming up to several meters thick (Leppäranta 2015).

For this thesis, various periods and transitions in ice phenology of a waterbody are defined by applying the terminology from the work of Leppäranta (2015) and Tedesco (2014), compiled visually in Fig. 1. After a waterbody starts to freeze, the date at which the transition occurs from ice-free lake to a frozen is called the *freezing date*. A waterbody can be partially frozen before becoming fully frozen, and the transition between the two is called the *freeze-up date*. As ice has become thin enough over late winter and spring, lake and river ice often falls apart to ice-floes under stresses from the wind and other stresses. The date when this occurs is called the *break-up date*. The *clear of ice date* indicates when a waterbody has first become fully open water.

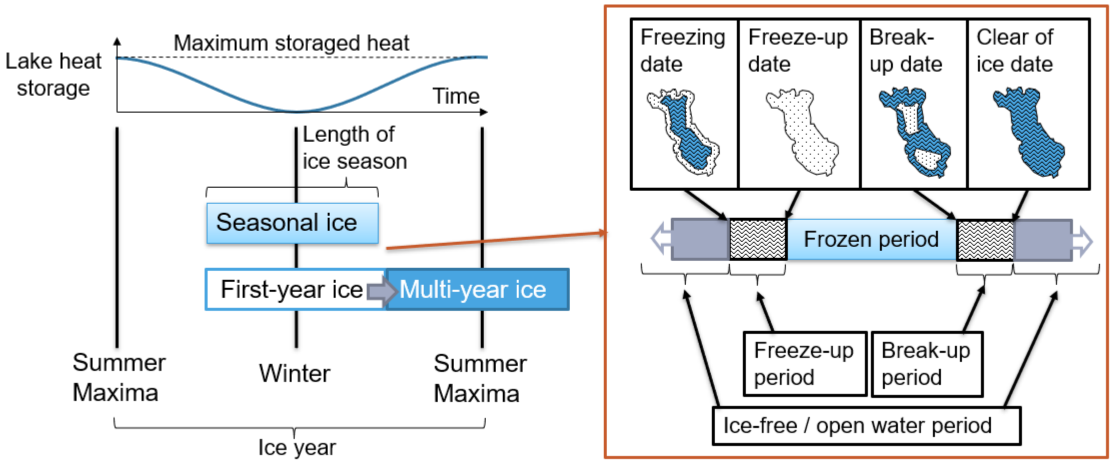

Figure 1 *Left: formation of seasonal ice during an ice year; right: stages of freezing and thawing of a waterbody (Leppäranta 2015), (Tedesco 2014).*

Evolution of lake and river ice is primarily a thermodynamic process (Leppäranta 2015). The various heat fluxes controlling water temperature are listed in the book by Maidment (1993) as short-wave and long-wave radiation heat fluxes, heat flux from the air and from precipitation, geothermal and sediment heat flux and latent heat flux from evaporation, with water friction and ground water heat fluxes being significant for some waterbodies. In shallow and clear lakes, it also is possible for sunlight to directly heat river or lake bottom sediment, storing heat and therefore affecting the later freezing process. Due to the heat-exchanging area being greater, shallow waterbodies cool faster as compared to same-volume but low surface area waterbodies, and in general the most rapid heat losses in inland waterbodies are caused by snowfall as energy is required for the snow to melt into liquid water (Maidment 1993).

As the seasonal temperature for surface water layer becomes lower during autumn and winter, it is possible for waterbodies to freeze in northern hemispheres when waterbody temperature falls below water freezing point. The freezing point for fresh water is approximately zero Celsius (Leppäranta 2015). Some waterbodies do not freeze fully or even partially in cold climate zones even if conditions generally allow other waterbodies to freeze over, such as rapids and streamlets being kept open by a constant flow of water. Certain large and very large lakes feature a thermal time scale longer than the winter resulting in them remaining either partially or fully open, with also some deep lakes not freezing due to being heated by geothermal energy (Leppäranta 2015).

The freezing process typically starts in riverbanks or lake shores instead of central areas, since the water flow is slower and less turbulent. Shallower water also cools faster. This creates suitable conditions for formation of frazil-crystals, which in turn grow and congregate to eventually become a thin layer of ice. The thin ice layer later bridges itself across a waterbody, while gaining more thickness, and eventually covering the whole waterbody becoming the primary ice layer (Maidment 1993). Secondary ice layers increase the thickness of the primary ice either below the ice via freezing water, or above the ice such as freezing slush becoming snow ice. A slush layer between the snow and ice can either be formed by melting snow, or water seeping through the ice layer (Leppäranta 2015).

The ice-sheet formed on top of the water is typically covered by a layer of snow for the duration of winter season. The snow accumulated above the ice layer is affected by the near-freezing point water underneath the ice, as the water is providing heat to the snow.

Snow may not adhere to the ice surface well in very cold climates and in certain situations wind can clear snow off the ice layer. Ice breakage and mechanical displacements are possible in very large lakes, and in smaller ones while the ice is weak (Leppäranta 2015). It is possible for seasonal ice in shallow areas of rivers or lakes, or even shallow waterbodies, freezing all the way to the bottom during the winter. This type of a phenomenon is dependent on the ice thickness growth below the primary ice, with the growth being slowed by snow acting as an insulator for heat-flux losses from the ice (Maidment 1993).

During spring, snow typically melts off either fully or partially off the ice sheet until the ice eventually breaks up and melts (Maidment 1993). A scenario where the snow layer above ice melted without ice break-up is also possible and was as an example observed mid-December 2017 as a part of this study from lake Pannujärvi (Fig. 2).

Figure 2 *Melted water on top of lake ice, lake Pannujärvi in mid-December 2017.*

As the temperature changes over seasons in Finland, water temperature changes considerably near the surface but remains approximately 4 °C in the deepest points over all seasons except for shallow lakes (Helminen 1977). Water layers will cycle over autumn and springtime as water temperatures near the surface are close to the temperatures in the depths. Over winters, water temperature in the depths is to be considered at around 4 °C, with the layer beneath the ice being close to the freezing point. Water temperature of large rivers remaining unfrozen over winters vary between +0.1 - +0.2 °C (Helminen 1977).

Decay of lake and river ice is a thermomechanical process. Melting of lakes typically begins from the shorelines, releasing a floating ice layer from its restricting boundaries. This allows the ice-layer to be shifted by wind and currents, leading to the ice breaking up to ice floes and eventually melting, leading to the waterbody becoming free of ice. Heat flux from solar radiation to ice becomes greater as a snow-layer melts off and bare ice is exposed. Any impurities in the ice surface will increase the solar heat flux (Leppäranta 2015).

2.1.3 Ice phenology observations in Finland

Periodic observations on lake and river ice phenology are carried out in Finland by various agencies under Finnish environmental administration. These observations include river and lake ice freeze-up and break-up dates, ice type and thickness measurements and various others (Kettunen et al. 2008). Observations are stored within the Finland's environmental information system and the data can be openly accessed via a REST API hosted by Finnish Environment Institute.

Each repeated observation is performed in the same location, specified by coordinates in the environmental information system. Freeze-up and break-up observations are generally done around the same locations where water levels, ice thicknesses and surface water temperatures are measured (Korhonen 2005). Oldest continuous observations of ice break-ups exist from river Tornionjoki since 1693, though portions of these observation time series since are missing and have been estimated using other information. First extensive lake ice phenology observations and measurements have been conducted since the 1800's for lakes Kallavesi, Näsijärvi and Oulujärvi. In total observations from 114 different locations have been recorded in the information system, out of which around sixty observation locations are currently actively updated (Korhonen 2005).

Both the freezing process and the thawing process in observations have been divided into four distinct categories for manual observations, matching the different stages of the progress (Laasanen 1982). For freezing, shores of the waterbody freeze first, progressing until the whole shoreline including bays becomes frozen. Next, a waterbody can be observed to either partially, then fully, frozen within the field of view of the observer. Thawing process can be observed to first begin in the shores, then progressing until open water is visible in any areas beside the shoreline. Later the ice sheet becomes loose from the shores and breaks up, eventually leading to the whole lake becoming free of ice. It is possible that especially different stages during freezing and thawing can occur between the manual observations (Laasanen 1982).

In a study related to lake ice decay conducted by Bilello (1980), accumulated thawing degree-days (TDD's), were found to correlate with lake ice decay date especially for waterbodies without water currents or external actions to mechanically break the ice cover. Accumulated freezing degree days (FDD's) have been found to be useful in estimating lake ice growth (Ashton 1989). FDD is calculated by summing each average temperature that is negative starting from a date generally selected in autumn, and TDD is calculated by summing each positive average temperature starting from a selected date some time during mid-winter.

The observations for lakes in Finland using FDD's for lake freeze-up and TDD's for lake ice break-up in a report written by J. Korhonen (2005), where as an example statistically significant correlation between the latitude was found for both the dates of whole lake freezing and the dates of ice break-up (Fig. 3). Comparing accumulated FDD's of each freeze-up with lake depth showed clear correlation between the average lake depth. Shallow lakes of around 2 m average depths froze after around 20 FDD day-degrees, lakes with around 5 meters of average depth required around 40-60 FDD day-degrees (Korhonen 2005).

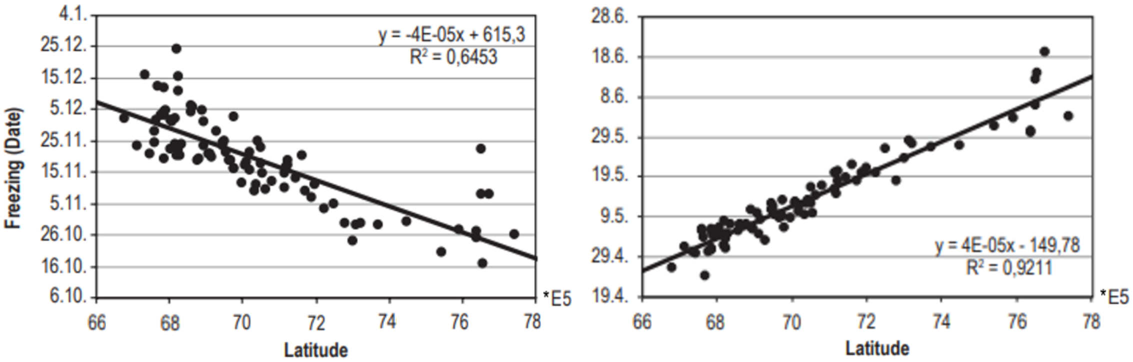

Figure 3 *Scatterplots between the latitude in KKJ coordinate system and ice phenology observations of select lakes. Left: break-up dates; right. freeze-up dates (Korhonen 2005).*

In the same report by J. Korhonen (2005), FDD's and TDD's have been used to filter clearly erroneous observations of freeze-up and break-up dates, as within reasonable range of error these should be the same for a waterbody between consecutive years. It is however to be mentioned that temperatures varying between positive and negative will delay both the freeze-up and break-up, therefore resulting in increased FDD and TDD values for the same waterbody. Other agencies such as harbour offices also make observations on ice freeze-ups and break-ups, and such observations for certain waterbodies were used in the report when official historical observations were unavailable (Korhonen 2005).

2.1.4 Ice phenology modelling

As the ice phenology observations can cover only a portion of waterbodies, models have been created for estimating lake ice freeze-up and break-up dates in lakes without physical in-situ observations. Ice phenology is generally modelled either using semi-analytic or numerical methods. Semi-analytic methods provide first order approximations of freezing – ice growth – melting cycles and are generally based on degree-days. Numerical models include full ice physics in their analytics, such as mechanical factors and thermodynamic fluxes (Engman 1993).

Using a numerical CLIME (Climate and Lake Impacts in Europe) ice model, the timing of freeze-up was found to be mostly dependent on the air temperatures and timing of snowfalls over autumn and early winter (Leppäranta 2009). Especially the timing of snowfalls affected the timing of ice formation by cooling lake water, while afterwards the timing of snowfall affected the growth of ice thickness accumulation. In turn the timing of ice break-up was affected by the snow cover via reduced solar heat flux and the thickness of accumulated lake ice. The study concluded that in order to fully explore the variability of lake ice break-up dates, a physically realistic model including ice stratigraphy data would be required (Leppäranta 2009).

In another study using a one-dimensional numerical model by Martynov et al. (2010), two competing effects were found to greatly influence the exact date of ice break-up – the thermal insulation of snow layer over the course of winter insulating the ice resulting in a thinner ice layer until spring, and snow albedo over spring decreasing absorbed solar radiation. Solar heat flux effects on water were dependent on water opacity. Improvement on simulations were considered from gaining a better understanding for each studied lake on physical processes such as seiches, convection of heat in water under the ice cover and properties of the snow cover during the winter.

A study was conducted by Yang et al. (2012) where one-dimensional modelling was applied on lake Vanajavesi. Weather station data was used in the HIGHTSI model (High-Resolution Thermodynamic Snow and Sea-Ice model), where surface temperature and heat-mass balance, snow cover changes and ice thickness evolution were modelled. Calculated dates for freeze-up and break-up of ice fitted well with manual observations of the lake. The timing of snow onset based on weather data, along with improving the estimated autumn freezing date for each year, were found in key role to also improve the modelling of ice thickness of lake Vanajavesi.

The watershed simulation and forecasting system, WSFS, has been developed by Finnish Environment Institute for modelling and forecasting various hydrological events in Finnish drainage basins and waterbodies. In total, the system contains more than 20 fully automatic watershed models, as an example modelling lakes and river discharge, precipitation, snow, soil moisture, subsurface and groundwater storage. For input, the model mainly uses weather observations and forecasts of the Finnish Meteorological Institute and for calibration a variety of both automatic and manual hydrological observations (Vehviläinen 1994). The model has been expanded in the 2000's to also use precipitation data from weather radars and optical satellite data for snow covered areas and flooded areas (Vehviläinen & Huttunen 2001).

WSFS offers forecasts for ice break-up date for a selected number of waterbodies based on temperature sums and historical break-up observations. One example of the ice break-up of river Tornionjoki being forecasted using the model 1-2 weeks in advance usually within a 1 to 3-day error (Vehviläinen & Huttunen 2001). Seasonal ice can also impact watershed modelling and waterbody observations. As an example, snowfall accumulates both on the ice and the surrounding area during wintertime, meaning wintertime precipitation cannot be corrected to water level observations and water discharge as the effects of snowfall are not realized prior to the snow and ice melting (Vehviläinen 1994).

2.1.5 Waterbody areas and DEMs available for Finland

Finnish Environment Institute provides the Jarvi-10 database containing all Finnish lakes and JokiAlue10 database containing Finnish rivers as high-detail polygon areas. The data is based on the topographic data of National Survey of Finland, NLS, from years 2000-2008, to which reclassification and topological corrections have been made by the Finnish Environment Institute.

Jarvi10 contains all Finnish natural and artificial lakes as polygon features (Fig. 4). Even waterbodies technically classified as ponds or lakelets are included, with smallest individual polygon sizes with lake coding being less than 0.1 hectares. JokiAlue10 contains river polygons that are 5 m or wider. Another dataset called the JokiViiva10 contains flow paths for even the smaller streams, as narrow as two meters, using lines instead of polygons. Each dataset's polygons are associated with the waterbody identification numbers which are unique for each Finnish waterbody, and the same values are used by other environmental information systems. Jarvi10 and JokiAlue10 data is downloadable from Finnish Environment Institute's website in a shapefile format.

Produced by the National land survey of Finland, NLS, the 10m digital elevation model or DEM10 (Fig. 4) is one of the most accurate sources of terrain elevation data available for Finland, with the error in elevation being less than 1.4 meters for 95% of the covered area. The elevation model is accessible from the NLS download-service. Height values are in accordance with the N2000 system, and these can be converted to the GRS80 ellipsoid heights by using the FIN2005 geoid (Saaranen et al. 2006). The elevation data also contains the approximate water surface elevations of rivers and lakes, which is useful for use in analysis of waterbodies since changes in terrain elevation mean the elevation of inland waterbodies' water surfaces also vary in Finland.

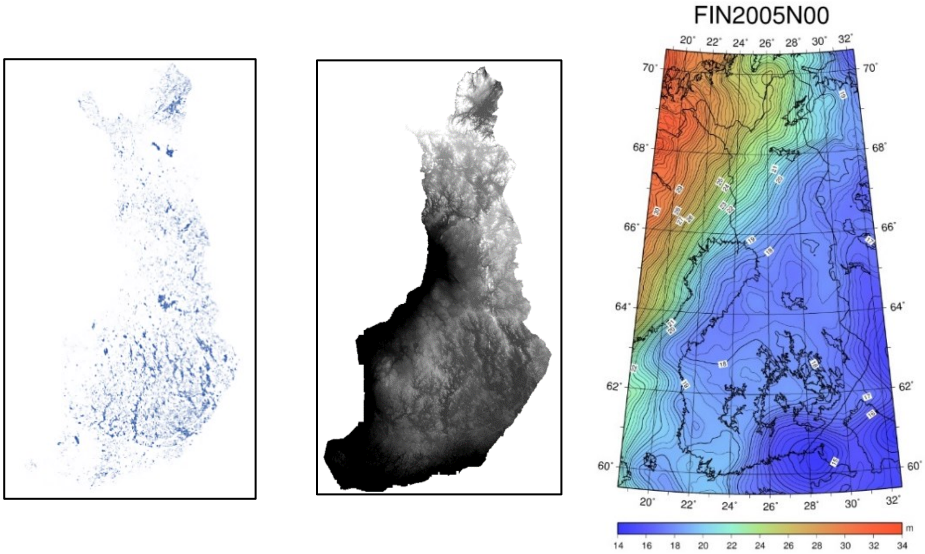

Figure 4 *Left: Jarvi-10 polygons; middle: DEM-10; right: FIN2005 geoid, from http://coordtrans.fgi.fi/*

2.2 Wind and waves in waterbodies

2.2.1 Water surface waves

Lake water can be divided to three different vertical layers due to their differing properties in various natural physical and chemical phenomena observed in lakes – the top layer epilimnion, the middle layer metalimnion and bottommost layer hypolimnion (Leppäranta et al. 2017). The movements of water can be divided to waves that are rhythmical movement and flows which are non-rhythmical. Further, there are two types of waves – standing waves and moving waves (Särkkä 1996). Finnish lakes are too small to be significantly affected by tides. Any tidal changes in water level and tidal currents are small enough to be masked by greater fluctuations due to barometric pressure and wind (Ward 1979).

For non-rhythmical flows, seasonal temperature changes cause vertical water movement called turnover over autumns and springs. Non-rhythmical horizontal flows can also be considerable in lakes where water passes through the lake. An example lake was presented in Finnish Environment Institute report by Kettunen et al. (2008) with horizontal flows in different parts of a lake (Fig. 5). Points A and C have a slow, laminar flow but point B in a narrowed location can feature a faster turbulent flow.

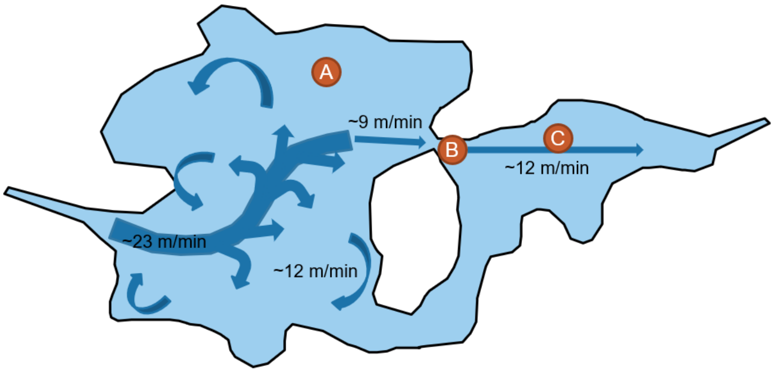

Figure 5 *Example of horizontal, non-rhythmical flow in a lake (Kettunen et al. 2008).*

Horizontal flows are also affected by the wind conditions. Continuous wind to a certain direction causes a slow flow of water to occur near the surface. This is a fraction of the wind speed, such as measured to be around 15 centimetres per second at wind speeds of 6 m/s for lakes (Särkkä 1996). This flow can however cause the water surface to become skewed as relative level of water surfaces falls against the direction of the wind and rises along the wind. As the phenomenon continues, a counter-flow of water evening the difference in the level of water will occur above the metalimnion layer. In shallow waterbodies without a distinct metalimnion layer (Fig. 6), the flow occurs along the bottom of the waterbody (Järnefelt 1958).

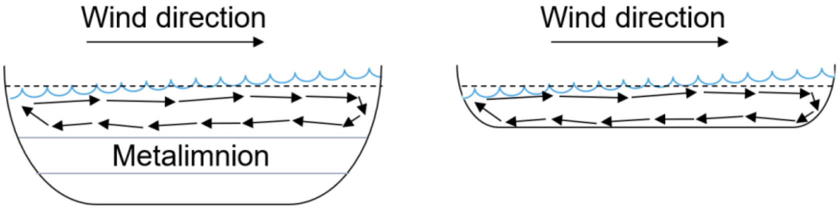

Figure 6 *Left: example of horizontal flows in a lake caused by wind in a deep lake; right: similar flows in a shallow lake (Järnefelt 1958).*

Standing waves in lakes are called *seiches*. Formed by sudden changes in air pressure, rainfall or gusts of wind, seiches form an oscillating wave movement with a minimum of single knot in the wave (Fig. 7). Internal seiches can be formed below the surface, via layers being formed by water differing in density. Standing waves can be found in all lakes, although they are much more discernible in lakes with a rounded surface and round geometry. For Finnish lakes that generally have an uneven bottom surface and feature irregular geometry with islands, capes and bays, so the phenomenon has rarely been observed (Särkkä 1996).

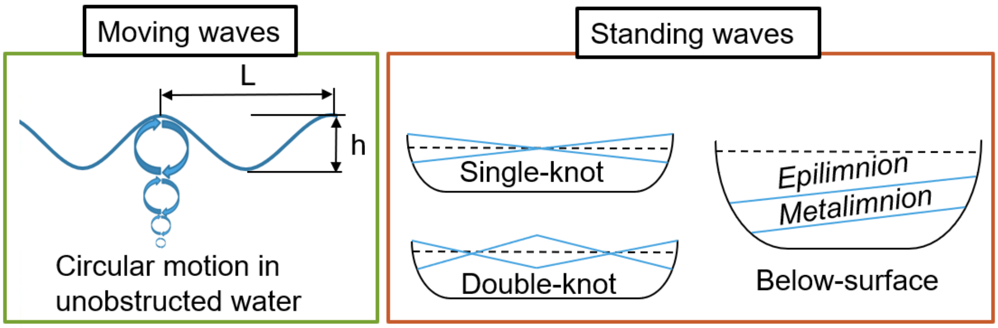

Figure 7 *Moving waves and standing waves (Järnefelt 1958), (Wetzel 1983).*

Moving waves feature repeating circular shaped motion patterns relatively near the surface. The circular movement amplitude, or circle diameter, becomes less the deeper they are observed (Fig. 7). Water forms surfs in case water depth is less than half of the wavelength of water waves, as an example seen in areas where rocks are present near the surface under the water (Särkkä 1996). Langmuir circulations are counter rotating vortices near a water surface aligned in wind direction, formed by steady wind. These spirals turn direction around their axis by every second turning counter-clockwise and are the cause of whitecaps in water as counter-flowing spirals collide. White-caps or breaking waves have been observed in inland waterbodies starting from wind speeds of 5 m/s and are covering most of the water surface at wind speeds exceeding 15 m/s (Särkkä 1996). Coriolis-effect, caused by Earth's rotation, can rotate surface flows of water causing Ekman-spirals, present mainly in large to very large lakes (Goldman & Horne 1983).

2.2.2 Wind-wave interaction in waterbodies

Winds are formed by atmosphere pressure differences causing air to move from high-pressure areas to low-pressure areas. As pressure gradients form along the Earth's surface, the greater the pressure difference between two points at the same elevation the greater the wind response. Frictional drag effects winds by reducing their speed and the Coriolis effect deflects wind directions especially in larger scale winds (Petersen et al. 2016).

Winds can be categorized by a multitude of factors, such as their pressure system they are part of, the scale of local surface winds as compared to global wind patterns and whether they are geography-specific winds such as mountain-induced foehn-winds. Surface winds occur low enough to the surface to effect waterbodies. It is to be noted that wind directions are typically indicated as from what direction wind is flowing from (Petersen et al. 2016).

The formation of waves is a complex interaction between the overlying air and the water. Wind speed, wind duration and the distance over which wind travels all affect the wind formation. Small ripples are formed when turbulent pressure fluctuations in the air initiate changes in the water surface. As wind continues to affect the small ripples, fluctuations in velocity and pressure of overlaying air becomes synchronized with the ripples. Over time the ripples gain enough wave height to be considered waves (Fig. 8) and grow further in size as wind flow begins to affect upwind wave faces (Hristov et al. 2003).

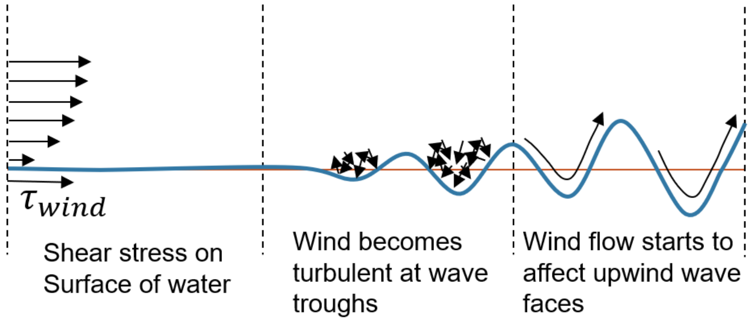

Figure 8 *Wind formation from laminar wind conditions to fully developed waves (Paquier et al. 2016).*

Even for moderate wind velocities, flow of air near the water surface is turbulent and causes slight ripples on the surface (Paquier et al. 2016). At wind speeds of 2.5 m/s and below the surface is approximately aerodynamically smooth. Above 2.5 m/s and below 10 m/s the surface becomes rough with occasional whitecaps and above 10 m/s it is fully rough (Charnock 1955). An important characteristic for turbulent surface fluxes in the wind is the *aerodynamic roughness length* which can be generalized for surface objects with varying geometry. As a laminar wind flow meets an aerodynamically smoother surface, it is less affected by the surface friction. Surface roughness lengths are as an example used by the HIRLAM, High-Resolution Limited Area Model, which models and extends in-situ measurements for various weather phenomena in Finland (Tammelin et al. 2011).

To estimate the probable wind speed at heights above the surface, a wind speed gradient can be estimated (Fig. 9). At the exact surface, wind speed equals to zero. The greater the obstruction height, the greater turbulence and lower wind speed near the surface, and wind speed begins to be affected higher from the obstruction (Charnock 1955).

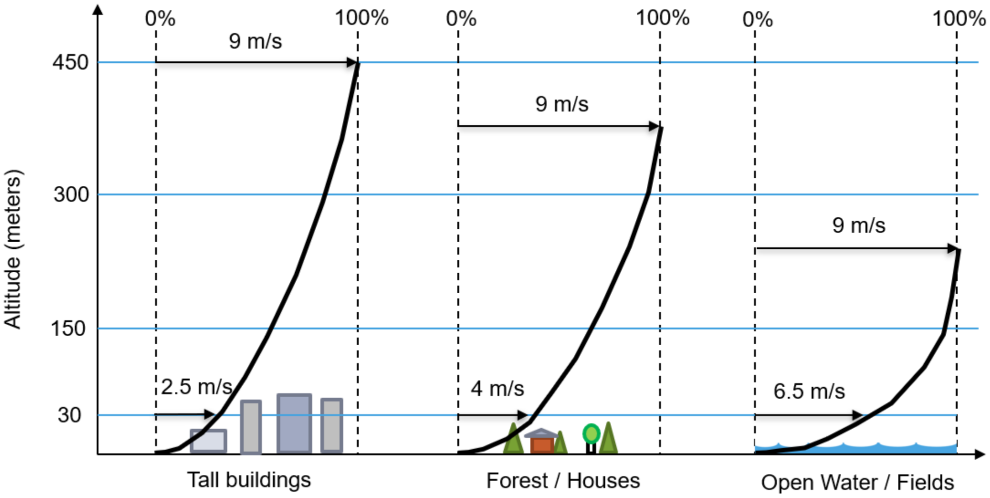

Figure 9 *Example of wind speeds above different surfaces (RLS Energy 2018).*

Near the surface wave height, or amplitude, can be estimated to around 1/20th of the wave length. Wave height grows over a freely travelled distance over water. Wind-induced wave amplitude will be at approximately the wind height h when the distance is x (Särkkä 1996).

$$h = 0.105\sqrt{x} \tag{1}$$

A clear majority of Finnish lakes by total count are between very small and medium sizes, resulting in maximum diameter of around ten kilometres at most. However, for the largest of waterbodies in Finland with diameter long enough in the corresponding wind-direction can form large enough waves to result in next to loss water vegetation at shorelines (Helminen 1977).

A phenomenon called wind sheltering is caused by the surrounding area terrain around lakes. As the wind flows above surrounding terrain, a sheltered area with considerably lower wind speeds is formed near the shore. This area has little to no waves or ripples due to the decreased shear stress. Outside the sheltered area, the flow of wind becomes re-attached to the water surface, forming a new boundary layer with shear stresses and resulting waves. The distance at which the re-attachment occurs at a distance determined by the properties of the surrounding terrain (Markfort et al. 2010). In Finland, forests can be considered the main type of terrain surrounding lakes and rivers.

Wind sheltering for different canopy covers was studied in by Markfort et al. (2012) via both wind tunnel experiments and field measurements from natural waterbodies (Fig. 10). Less dense and low-porosity forests were found to cause less sheltering as the flow of wind can go through them. Taller forest canopies were found to create a longer sheltered area for waterbodies towards the wind direction (Markfort et al. 2012). Wind sheltering effect has also been observed on island-based canopies, and surface wave patterns change around islands due to the waves impacting the island (Aurthur 1951).

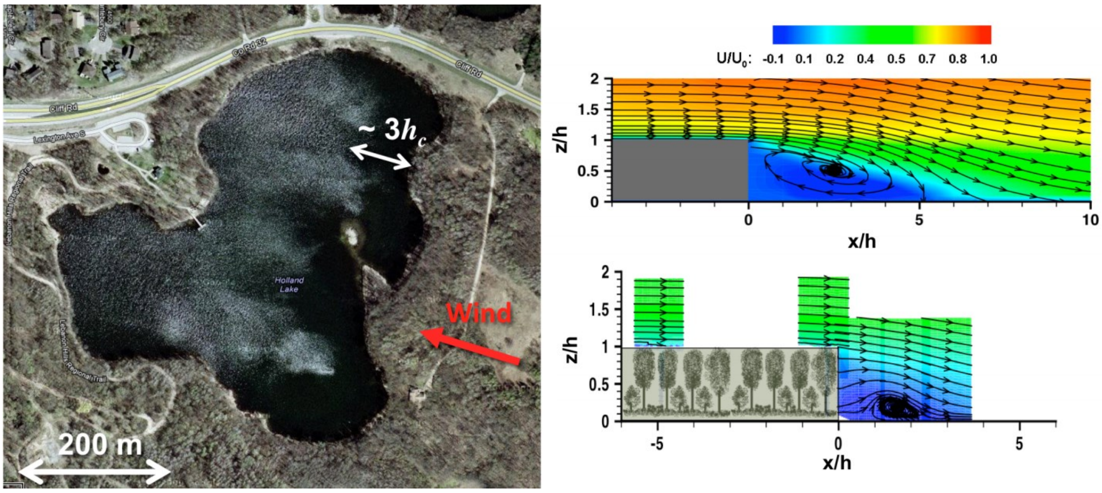

Figure 10 *Left: very small lake with wind sheltering affecting the eastern side; right: wind tunnel testing of simulated forest canopy with normalized mean velocities for the wind field (Markfort et al. 2012)*

Rainfall causes changes to the water surface waves by three main mechanisms (Alpers et al. 2016). Rain droplets impacting a water surface will generate splash products impacting radar signatures, while the droplets will also create ring waves via their impact with the water surface both affecting backscattering and the way the waterbody surface is affected by wind. Downdrafts of rain cells can also cause the wind shear stresses of the water surface. The combined effect in C-band synthetic aperture radar images (Fig. 11) can either increase or decrease the backscattered signal (Alpers et al. 2016).

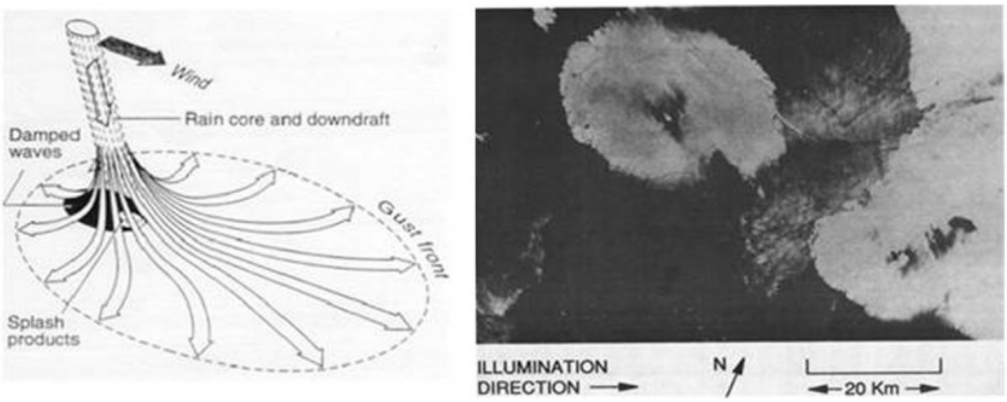

Figure 11 Left: *Wind downdraft phenomenon as a graph on the left; right: Effect of rain and wind downdraft on a waterbody in a C-band radar image (Alpers et al. 2016).*

2.2.3 Wind and rain radar measurements in Finland

Finnish Meteorological Institute (FMI) gathers various weather measurements from a network of a total of 400 weather stations in Finland. The instruments on each station vary, meaning that the available measurements from the stations varies. There are ten microwave weather radars operated by FMI. Both the radar data and wind observations can be accessed via a WFS 2.0 service, after registering to the service and receiving an api-key.

Weather observations are saved for a single observation station and sampled every 10 minutes. Location of the station is also received in the specified coordinate system. The stations conducting wind measurements offer the average wind speed, greatest measured wind speed or gust speed, and wind direction. Wind speed and direction measurements were collected continuously on 95 unique stations as of spring 2018.

Radar data is formatted in a raster for either the dbz, decibel relative to Z, or rr values, rainfall intensity, in 10-minute intervals. This data is offered in different raster formats and different combinations of weather radars. Data is openly accessible for 6 days from the currently operating weather radars in Finland.

2.3 Spaceborne radar

2.3.1 Synthetic Aperture Radars

Microwave remote sensing uses microwaves for estimating the properties of the measured surface. There are two types of microwave instruments – active, where the instrument is called a radar, and passive where instruments are called radiometers. A radiometer merely measures the emitted energy within its region of the electromagnetic spectrum, while radars send radio pulses and “illuminate” measured areas, then receive and measure the returning radio signals that are reflected back. Microwave radar remote sensing is not dependent on sunlight as compared to optical sensors, making it highly useful for making observations of the Earth’s surface in darkness of both nights and winter months. A typical modern spaceborne microwave radar instrument is a synthetic aperture radar, SAR (McCandless & Jackson 2004).

The SAR was first patented in the 1960’s by Carl Wiley (1965). The first civilian SAR earth observation satellite, NASA’s SEASAT, being launched in 1978 (Doerry & Dickey 2004). A history of spaceborne SAR satellites intended for civilian use are provided in table 4.

Table 4 *History of spaceborne SAR sensors (Gade 2015).*

Year	*Satellite*	*Organization*	*Band*	*Incidence Angle*	*Polarization*
1978	SEASAT	USA	L	23°	HH
1981	SIR-A	USA	L	50°	HH
1984	SIR-B	USA	L	15°-65°	HH
1991	ERS-1	Europe	C	23°	VV
1991	ALMAZ-1	USSR	S	30°-60°	HH
1992	JERS-1 (Japan)	Japan	L	39°	HH
1994	SIR-C/X-SAR	USA, Germany	L,C,X	15°-55°	HH, HV, VV, VH (Sir-C), VV (X-SAR)
1995	ERS-2	Europe	C	23°	VV
1995	Radarsat-1	Canada	C	20°-50°	HH

2000	SRTM	USA, Germany	C, X	54°	HH, VV (C), VV (X)
2002	ENVISAT	Europe	C	15°-45°	HH, HV, VV, VH
2006	ALOS-1	Japan	L	8°-60°	HH, HV, VV, VH
2007	TerraSAR-X	Germany	X	15°-60°	HH, HV, VV, VH
2007	Radarsat-2	Canada	C	10°-60°	HH, HV, VV, VH
2007…10	COSMO-SkyMed 1-4	Italy	X	10°-60°	HH, HV, VV, VH
2010	TanDEM-X	Germany	X	20°-59°	HH, HV, VV, VH
2014	ALOS-2	Japan	L	15°-60°	HH, HV, VV, VH
2014	Sentinel-1A	Europe	C	8°-70°	HH/HV, VV/VH
2016	Sentinel-1B	Europe	C	20°-45°	HH/HV, VV/VH

The advantage of a SAR system comes from utilizing the doppler shift phenomenon, greatly increasing the azimuth resolution of a side-looking radar while allowing for antenna sizes only a fraction at the same angular resolution as real aperture radars (McCandless & Jackson 2004). SAR's predecessor, real aperture radar, relies only on transmit-receive delay to create radar images while moving over and illuminating a measured surface. To reach range-resolution low enough to be useful, they will require a pulse to be transmitted in a very rapid interval, with the interval is often too rapid for the transmitter to provide enough power to produce a useful signal-to-noise ratio or SNR. Real aperture radar azimuth resolution is also limited by its beam width since returning echoes from the same distance are all received at once within the illuminated area. The azimuth resolution can only be improved by either using a longer antenna or a shorter wavelength, leading to a poor azimuth resolution from orbital altitudes as practical antenna size in satellites is limited to few meters (McCandless & Jackson 2004).

While moving at a constant velocity, a SAR-instrument's transmitter sends radio pulses towards the reflecting object and the system measures the instantaneous Doppler shift and delay of the reflected signal via its' receiver (Doerry & Dickey 2004). As compared to a real-shift aperture radar, this allows for a higher azimuth resolution along flight direction projected on the ground (McCandless & Jackson 2004). Modern SAR-instruments, such as the Sentinel-1 C-SAR, transmit a chirp signal where the signal is frequency modulated during a single pulse. A chirp-based SAR systems' data is faster to process, and the transmitter can generate longer chirps easier as compared to non-chirped pulses. One common chirp method is called LFM (linear frequency modulation), where the pulse's signal is either increased or decreased in a linear fashion over the course of a pulse (Moreira et al. 2013).

While moving along its path, a SAR instrument illuminates the same measurement target several times by transmitting the pulses and receiving the backscattered signal (Fig. 12). By accumulating the history of backscattered signals from the measurement targets as the antenna has moved along its path, the radar data can be reconstructed into a radar image (Mott 2007).

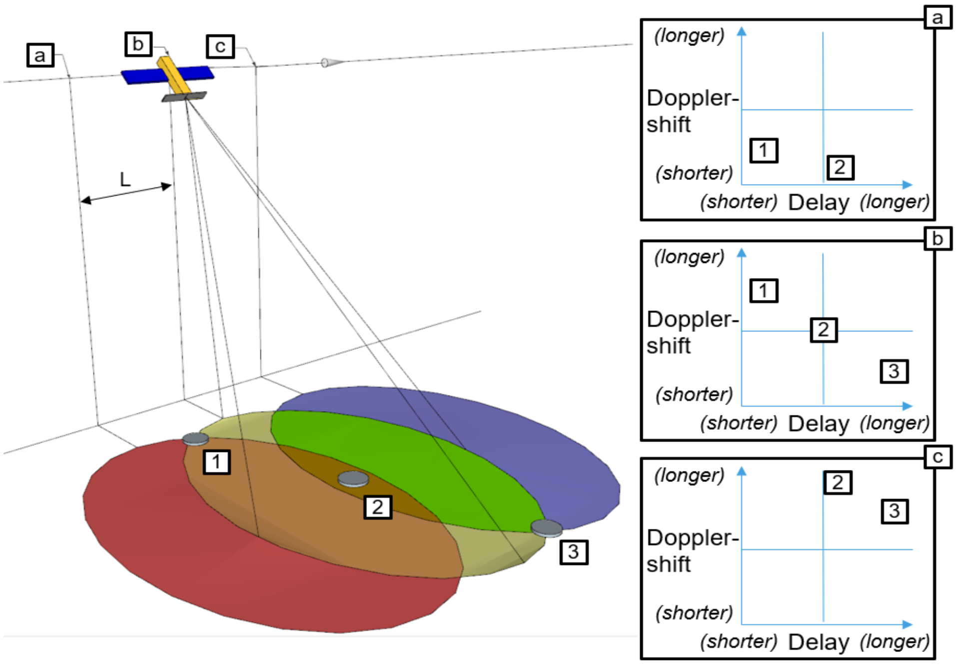

Figure 12 *A simplified scenario of SAR pulse doppler shift and delay for three targets; a, b and c. Applied from the article of Doerry and Dickey (2004).*

The signals collected by a spaceborne SAR are generally computed to a raw-file within the satellite, referred to *level-0* products, and sent to the ground segment for further processing and distribution. A process called radar image focusing (Fig. 13) is required prior to them being converted to usable *level-1* products (ESA 2018). Considered a two-dimensional focusing operation, the first step is to de-chirping the received echoes which focuses the range-direction of the radar image. Second, azimuth-direction focusing is applied based on the Doppler-shift data (Johannessen & Collard 2013). Additional corrections may be needed in focusing to compensate spacecraft motion, Earth's rotation and other factors (Rabus et al. 2002). For Sentinel-1, the primary Level-1 product after focusing is called single look complex (SLC) which contains the amplitude, wave height of the returned signal, and phase of the returned signal (ESA 2018).

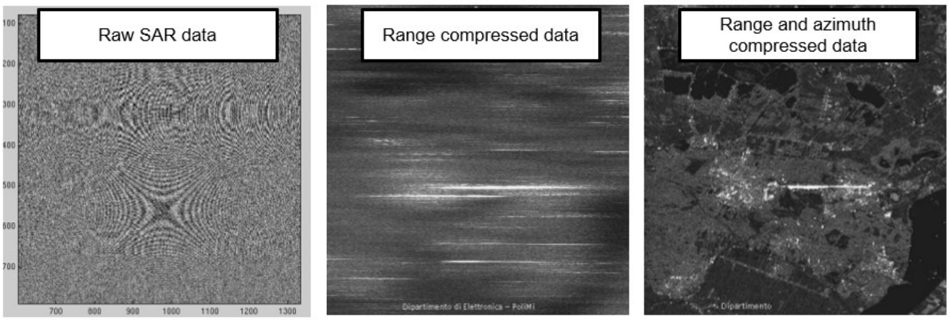

Figure 13 *How raw radar images look like during each step of focusing (Johannessen & Collard 2013).*

Before saving the data in a digital raster format, the pixels from the data acquisition must be resampled to a uniform grid due to the range-resolution varying with the radar incidence angle. Often the final format is selected by a multiple or a discrete divisor of 100 meters as per conforming to standard map scales (ESA 2018). Range-resolution for the processed SAR radar image is determined by the SAR's transmitted chirp bandwidth and the azimuth resolution is determined by the radar's azimuth antenna length, being half of the length of the aperture antenna (Moreira et al. 2013).

Phase information in focused radar images is useful in interferometry, such as producing interferograms, though not necessary for all types of analytics performed on radar images. Therefore, radar products can merely feature the backscattered amplitude with loss of the phase information, as with Sentinel-1 ground-range detected (GRD) products. The main type of utilized data in this thesis is on backscattered amplitude without the phase information by using GRD products, with one benefit offered are considerably smaller file sizes as compared to SLC (ESA 2012).

2.3.2 Radar signal backscattering

Backscattered signal amplitude indicates the received signal strength from the measured target or region, also called the target "brightness" in a radar image. The portion of the energy scattered back to the SAR receiver is influenced by a wide variety of factors.

- Microwave frequency
- Radar transmission power, instrument transmission line losses
- Free space propagation, atmospheric signal attenuation and scattering
- Incidence angle
- Polarization
- Physical factors of the measured surface, such as the dielectric constant
- Geometric factors such as surface slope, roughness
  (Campbell & Wynne 2011)

Spaceborne SAR's use frequencies that are outside the specific resonation wavelengths of atmospheric gas molecules and lower than 12Ghz, above which atmospheric attenuation becomes significant. In general, the lower a signal frequency is, the less it is affected by physical obstacles, causing the low-frequency L-band SAR's to penetrate vegetation and even soil better than C- or X-band radars (Richard 2008). Different band designations area shown in table 5.

Table 5 *Radar frequency designations (Campbell & Wynne 2011).*

Band	*Wavelengths*	*Frequencies*
P	107-77 cm	0.28 – 0.4 GHz
L	30 – 15 cm	1.0 – 2.0 GHz
S	15 – 7.5 cm	2.0 – 4.0 GHz
C	7.5 – 3.75 cm	4.0 – 8.0 GHz
X	3.75 – 2.40 cm	8.0 – 12.5 GHz
Ku	2.40 – 1.67 cm	12.5 – 18.0 GHz
K	1.67 – 1.18 cm	18.0 - 25 GHz
Ka	1.18 – 0.75 cm	25.0 – 40.0 GHz
VHF	100 – 1000 cm	0.3 - 0.03 GHz
UHF	100 – 10 cm	0.3 – 3.0 GHz

Radar signal scattering means the reflection of radar pulse from the illuminated surface. Scattering can also occur in the atmosphere in case hail or rain droplets are present (Alpers et al. 2016). Surface scattering occurs from a boundary surface where the dielectric constant changes – such as radar signal travelling through the air, then scattering from an ice surface. Surface scattering generally is reflected to a different direction from the incident wave, but in some cases a double bounce instead of single-bounce (Fig. 14) can occur from two surfaces (Andre et al. 2008).

For volume scattering (Fig. 14), a radar signal does not scatter from the surface, but instead penetrates the material and scatters multiple times within the material prior to either bouncing back or becoming fully attenuated. This can occur within materials with low dielectric constants, such as snow, or complex geometric structures such as forests (Andre et al. 2008).

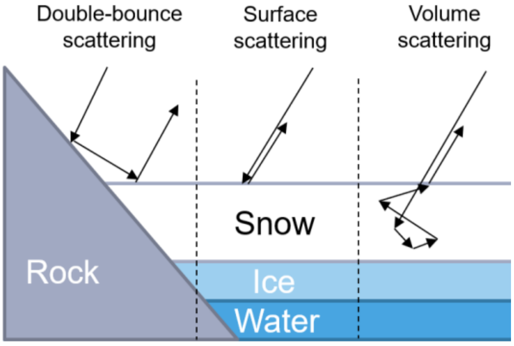

Figure 14 *Radar signal scattering types (Andre et al. 2008).*

As the incidence angle of the radar signal decreases, or satellite is closer to flying directly above the pulse-illuminated surface, there is generally an increase in the backscattering intensity depending on the surface scattering properties at different incidence angles (Jackson & Apel 2005). The slope of the surface has a similar effect as the angle changes, by determining the local incidence angle. Using a DEM and knowing the satellite trajectory, the local incidence angle (Fig. 15) can be calculated which takes into accord the local surface slope (Jackson & Apel 2005). Ground-projected range-resolution of radar images is affected by the surface geometry, since for the same orthogonal distance a slope towards the radar has a proportionally higher area in non-projected SAR-images while comparing to the opposite slope. If the opposite slope is steeper than the incidence angle, it becomes shadowed (Fig. 15) and cannot be imaged using SAR (Henderson & Lewis 1998).

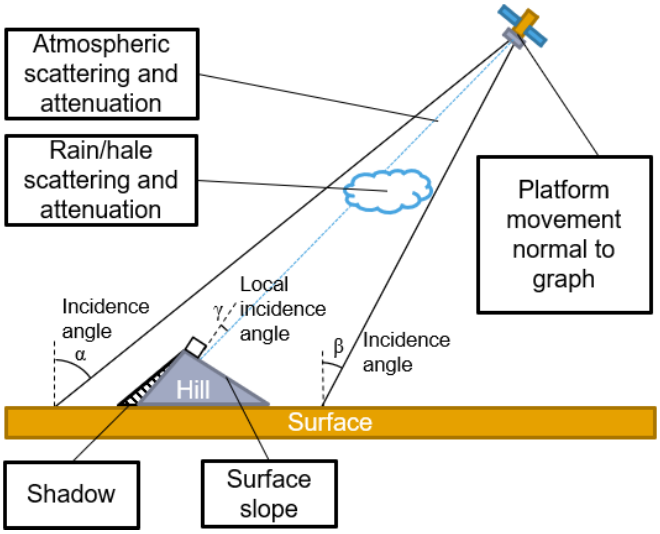

Figure 15 *Showing radar interaction with the atmosphere, radar shadow and the concepts of radar shadow, surface slope and incidence angles (Jackson & Apel 2005).*

Radio signal attenuation, affected by the dielectric permittivity of the medium where the signal travels, means that a radio signal loses energy over its path through the medium. Signal attenuation determines the maximum penetration depth when traversing through surface mediums – signals penetrate substances with relatively low dielectric permittivity further such as snow as compared to substances with high dielectric constant such as water (Henderson & Lewis 1998).

Signal path traverses through the atmosphere twice for spaceborne SAR's, after being transmitted and after being backscattered and returning to the receiver. The atmospheric composition of gases such as water vapour and oxygen cause signal loss via molecular absorption of energy of the pulse. Atmospheric losses are always present, and they cannot be avoided (Jackson & Apel 2005). For clouds with high-water content, water droplets can cause radar backscatter to either gain intensity or lose intensity via volumetric scattering (Fig. 15) while the intensity gain is more common (Ulaby et al. 1981). It is to be noted that a radio signal refraction of SAR pulses can occur in the atmosphere, especially when traversing through the ionosphere. This can cause a delay in the radio signals, affecting the phase-based SAR-interferometry (Phan et al. 2014).

For surfaces, backscattering will change as their surfaces' properties change, including the dielectric constant, surface coarseness and surface geometry (Henderson & Lewis 1998). As an example, if a forest area vegetation or soil moisture changes, this will also change the dielectric properties of surface while manmade ploughing of agricultural fields or water surface waves changing backscattering via changing surface geometry. As another example, a coarse ice surface generally features a stronger backscattering when compared to a smooth ice surface of same type (Henderson & Lewis 1998).

A specular reflector, such as a still water surface (Fig. 16), reflects most of the radar pulse's energy to the specular direction from the pulse instead of returning the pulse towards the SAR instrument. A diffuse reflector instead reflects the signal in a more even pattern (Fig. 16), though natural surfaces such as a rough, wavy water surface always features a stronger reflection in the specular direction. Mixed reflectors (Fig. 16) are reflectors with both diffuse and specular reflecting properties (Campbell & Wynne 2011).

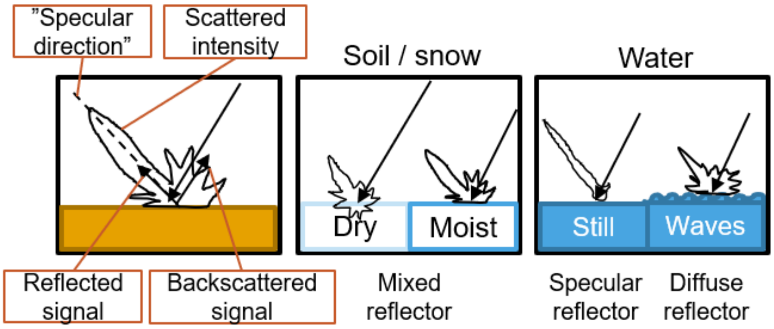

Figure 16 *Exaggerated radar scattering examples for various surfaces (Campbell & Wynne 2011).*

As the surface dielectric constant changes from low to high, such as dry soil becoming wet (Fig. 16), the signal penetrates the surface material less decreasing attenuation, and more of the radio pulse energy is transmitted back to the receiver increasing the backscatter. The same phenomenon occur as snow begins to melt, as wet snow has a higher dielectric constant than dry snow (Campbell & Wynne 2011). On the other hand, if a soil or ice layer is fully covered by water, it would become a specular reflector resulting in decreased backscattering (Jackson & Apel 2005). It is to be noted that especially for water surfaces, Bragg scattering will affect the signal by increasing the backscattering. Bragg scattering occurs when reflecting surface geometry are geometrically in phase, amplifying the backscattering from the surface (Ulaby et al. 1981).

SAR instruments can feature different polarizations. As electromagnetic signals, including radio pulses from the transmitter, can be polarized either vertically (V), horizontally (H), at an angle between the two or using circular polarization (Ulaby et al. 1981). Use of different polarizations is beneficial when using both equal polarity HH or VV radar images in conjunction with VH or HV, indicating polarimetric properties of the measured surface (Mott 2007). Though some satellites feature four different polarization modes for single radar image acquisitions, Sentinel-1 uses two polarities at once, VV/VH in IW-mode and HH/HV in its EW-mode (Gade 2015).

All SAR images regardless of the resolution and frequency feature an effect called speckle. Speckle is inherent to imaging of radar scatters due to SAR being a coherent imaging sensor (Moreira et al. 2013). There are a variety of elemental scatters within a resolution cell, distributed randomly. Summing their amplitudes and phases coherently will result the backscattered signal to fluctuate significantly between different cells, causing speckle. An increase in signal power does not remove speckle effects, instead merely increasing the variance of speckle’s intensity (Moreira et al. 2013).

SAR-receivers will also receive noise from external and internal sources. Thermal noise is produced by the internal electronics of a radar due to microscopic motion of electrons due to temperature, with most of the thermal noise is generated by the first amplifier after the receiving antennae (Barton 2005). To list external sources of noise, satellite-based instruments will receive noise from the space via solar or galactic noise. As no antenna pattern is completely ideal, featuring so called side-lobes, ground noise will be produced to the SAR-data by the energy sent by side-lobes being backscattered from the ground surface. Manmade interference at the same frequency used by the receiving antenna also has potential to cause external noise to the data (Barton 2005).

Combining all noise sources determines the noise-floor of SAR-data. If a backscattering signal’s intensity is too low to fall below the noise floor, only noise is present in a SAR-image. The ratio between a received signal and the noise floor is called the noise-to-signal ratio – SNR (Barton 2005). Especially for targets with low backscattering intensity, it is crucial to note the effects of noise not being prevalent over the actual received target backscattering (Park et al. 2017).

2.3.3 SLC conversion to GRD

As the information from backscattered radar pulses are processed from level-0 raw data product to a level-1 data product, such as GRD and SLC for Sentinel-1, it is commonly required to perform a few more steps prior to analysing the data (Jackson & Apel 2005). These steps depend on the final application. As an example, speckle can be reduced using speckle filtering, various sources of noise can be removed, and data can be georeferenced.

GRD products are generated from SLC products. Following processing steps are briefly explained, as they are of importance for understanding on how Sentinel-1 operates.

- Debursting and merging of swaths
- Multilooking
- Slant Range to Ground Range Operator
- Resampling

Sentinel-1 is capable of operating in TOPS-mode, or Terrain Observation with Progressive Scans-mode. The satellite rotates its' antennae in the azimuth direction, collecting several subswaths of data which can later be assembled to a full acquisition (Fig. 17). IW-mode features 3 swaths, where every focused burst last ~2.75 seconds and the bursts overlap for ~0.4 seconds. EW features 5 swaths and a focused burst lasts for ~3.19 seconds, overlap is around ~0.1 seconds (Miranda & Rosich 2011). The swath-beams also overlap in the the range-direction, with the ground projected distance depending on the incident angle. Though a process with various steps, the overlapping is essentially is used to match both the phase and the amplitude to create a combined image of the focused images of subswaths (De Zan & Guarnieri 2006).

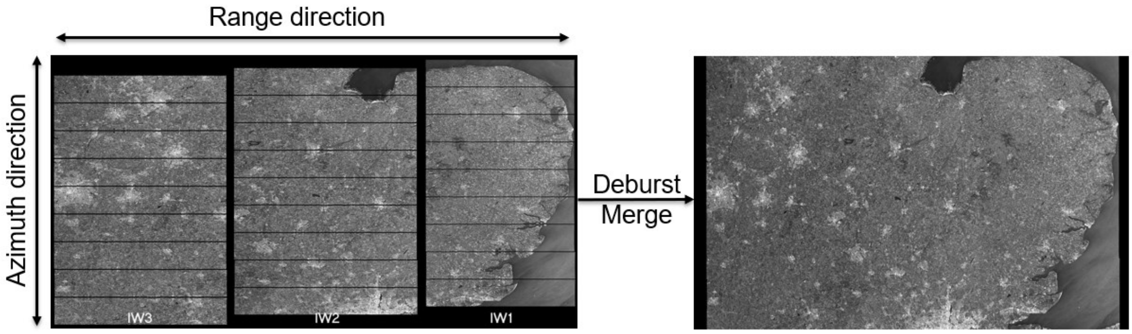

Figure 17 *SLC Debursting and swath merging (De Zan & Guarnieri 2006).*

The azimuth direction pixel spacing of the SLC product is considerably lower than spacing in range-direction. As most applications do require equal pixel spacing in azimuth and range, multilooking (Fig. 18) can be applied in range-direction to create a more equal pixel spacing in both directions (ESA 2018). Multilooking is a process where space-domain averaging is applied to a pre-set window size of azimuth and range pixels (Small & Schubert 2008). Multilooking also filters some of the speckle in the radar images, though also reduces radar image resolution (Moreira et al. 2013).

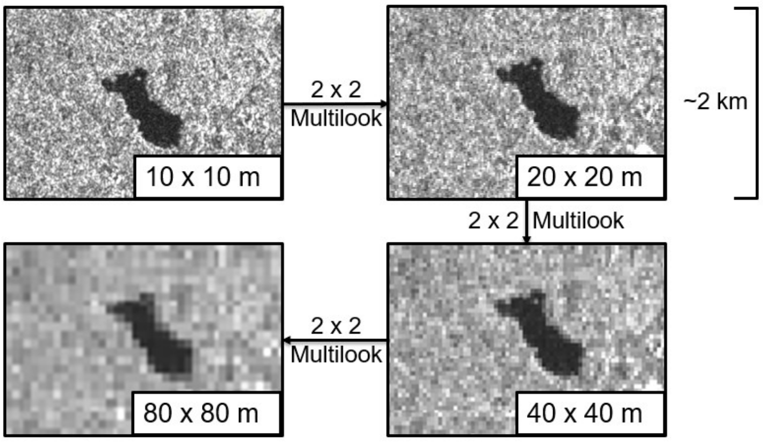

Figure 18 *SAR product multilooking with different resolutions using equal range-azimuth windows. Applied to a Sentinel-1 GRD product in ESA SNAP around Lake Pannujärvi.*

Slant-range to ground-range correction corrects the range detected by a radar to a ground-range. As a SAR is typically pointed sideward, not directly downwards, so ground-projected resolution changes especially in range-direction as incidence angle changes (Greer 1975). For processing SLC products to GRD products, this happens by converting the echo-delay range spacing to range-spacing proportional to distance from nadir along a WGS84 ellipsoid, then performing ground-projection resulting in 10 × 10-meter pixel spacing (Fig. 19). It is to be noted that changes in ground elevation are not taken into accord in slant-range to ground-range operator (Miranda & Rosich 2011).

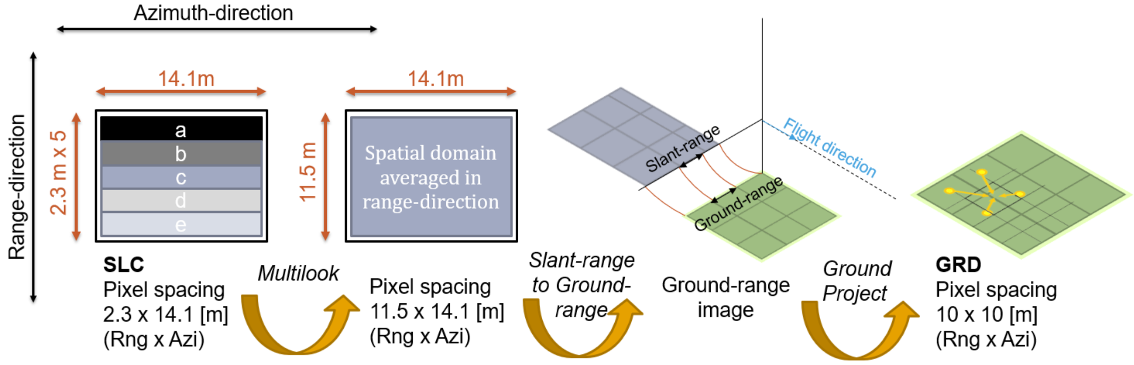

Figure 19 *Visualizing multilooking, slant-to-ground range correction and ellipsoid-ground, or terrain-, projection (Moreira et al. 2013).*

2.3.4 Common processing steps for GRD-products

For processing a GRD-products to sigma0 values (dB) in a suitable coordinate reference system for the intended use, following common processing steps in are introduced in this section.

- Calibration
- GRD border noise removal
- Thermal noise removal
- Speckle-filtering
- Terrain-Correction and applying precise orbits
- Resampling and subsetting

The *radar backscattering coefficient*, *sigma0* (σ^0), is conventionally used in SAR-data analytics indicating the backscattering properties of a measured surface. To calculate this value, backscattered signal intensity is normalized to a dimensionless number in respect to a nominally horizontal plane to indicate the signal strength expected from an area of one square meter (Henderson & Lewis 1998). The coefficient varies considerably as the radar incidence angle, wavelength, polarization and the properties of the measured surface itself. The backscattering coefficient's intensity value is often expressed in decibel scale (ESA 2018).

The processing step where the GRD or SLC radar image values are converted to sigma0 values is commonly referred to as calibration (Laur et al. 2004). Calibration vectors for the SAR sensor are required for the conversion, and for Sentinel-1 these are included in the data products by default (Miranda & Rosich 2011). It is possible to use either an ellipsoid to calculate the radar scattering coefficient or alternatively to use DEM-based local incidence angle for indicating a normalized radar backscattering coefficient, shown in Eq. (2) (Laur et al. 2004). As the radar backscattering coefficient is an intensity value, it can be converted to decibels by multiplying a base ten logarithm of the value by ten (Roberts 1984, Rev. 2003).

An antenna thermal noise pattern from the S-1 acquisition swaths is present in GRD radar images (Fig. 20). Thermal noise removal aka thermal noise correction can be done by subtracting the noise from a radar image. All GRD products contain thermal noise vectors, which enables users to remove the noise, as an example using the S1TBX (Ali et al. 2018).

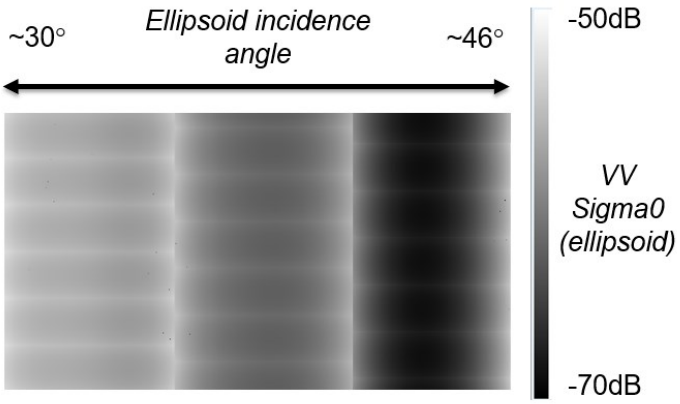

Figure 20 *Sigma0 equivalent antenna noise pattern in Sentinel-1 GRD product, calculated in ESA SNAP from S1A product S1A_IW_GRDH_1SDV_20180403T04494…*

GRD border noise on the other hand are considered artefacts, either erroneously high or low values, near the edges of GRD rasters. Removing these values to proper no-data values is called border noise removal (Fig. 21), which is useful when radar images are analysed near their maximum and minimum incidence angles, or edges in range-direction (Hajduch 2018).

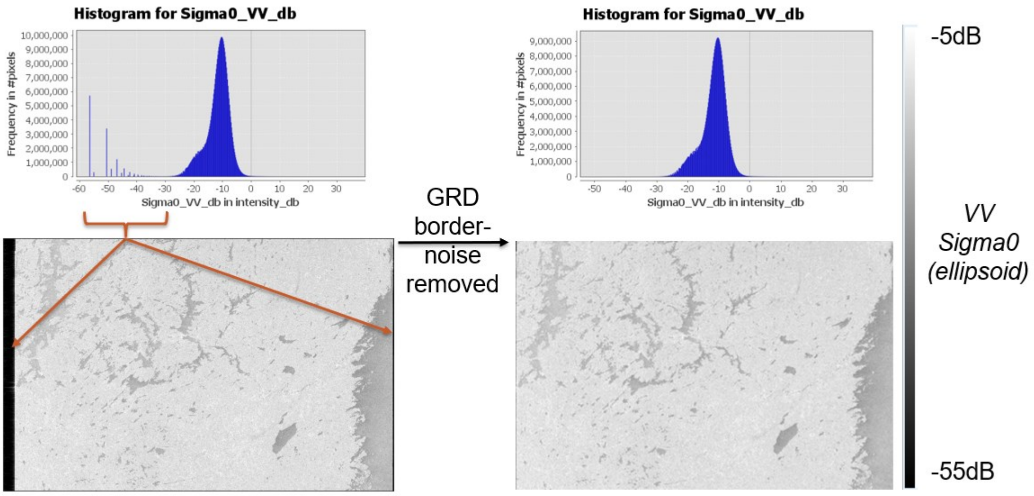

Figure 21 *Border noise removal using S1TBX in ESA SNAP, from S1A product S1A_IW_GRDH_1SDV_20180403T04494… with a histogram and radar image from prior GRD border noise removal on the left, after border noise removal on the right.*

As speckle is still present in the radar image from multilooking, additional speckle filtering can be applied to radar images (Moreira et al. 2013). The simplest speckle filtering method is the mean filter aka Boxcar filter, which works by replacing a centre pixel with a mean value from surrounding values of pixels within a scanning window. This filter smoothens images well but causes resolution loss near the vicinity of sharp edges, so small window sizes such as 3 × 3 or 5 × 5 are generally used (Lee et al. 1994).

A median filter that works in a similar fashion as a mean filter but uses the median value of the pixels within the scanning window. It does however cause blurring of edges, erasure of thin linear features and shape distortions in addition to being computationally demanding for large window sizes (Lee et al. 1994). Refined Lee filtering will form individual directional masks around each pixel value being filtered (Fig. 22), then determines the unspeckled intensity estimate with minimized mean squared error within the window. Sharp edges are better preserved as compared to mean and median filters, though results are not as smooth in comparison (López-Martinez et al. 2015).

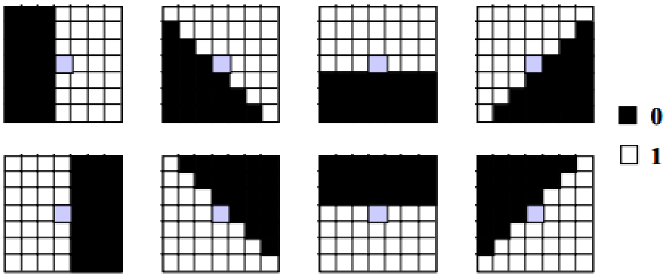

Figure 22 *Example of directional masks for refined-lee filtering (López-Martinez et al. 2015).*

Terrain correction using a DEM can be applied to a GRD product for improving geolocation accuracy of the radar image (Fig. 23), as GRD is by default projected using WGS84 ellipsoid which does not take into accord the actual surface elevation. Additionally, in case the ellipsoid is used as the incidence angle in calibration, the backscattering coefficient sigma0 can be normalized by using Eq. (2) first presented by J. M. Kellndorfer (1998).

$$\sigma^0_{NORMLIM} = \sigma^0_{NORMLIM} \frac{\sin \vartheta_{DEM}}{\sin \vartheta_{Ellipsoid}} \qquad (2)$$

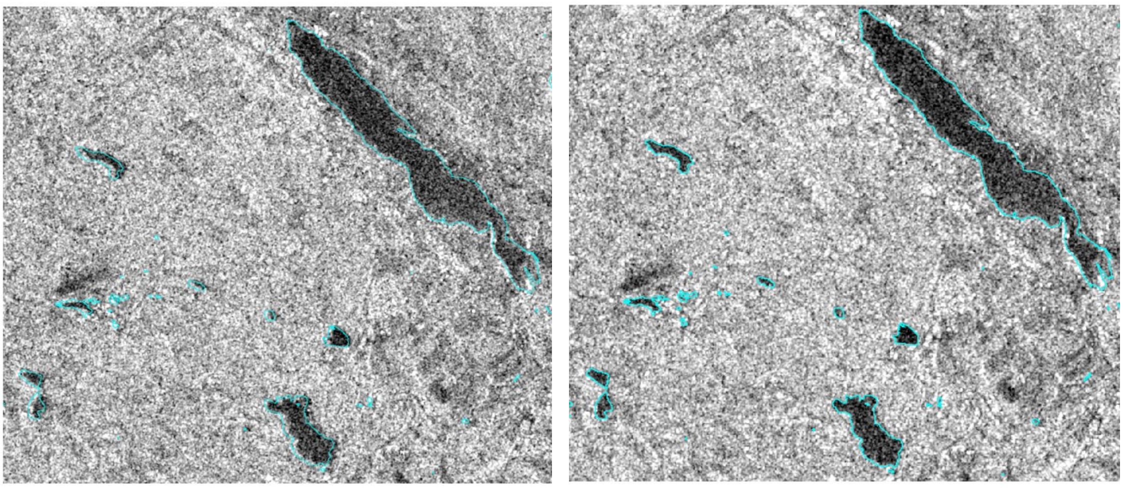

Figure 23 *Left: non-terrain-corrected ellipsoid projection; right: DEM terrain corrected radar image. Using radar image S1A_IW_GRDH_1SDV_20180403T044946…*

It is possible to add precise orbit ephemerides to the radar image metadata prior terrain correction, making the geolocation accuracy of the correction more accurate. These orbits are calculated based on the satellite GNSS-receiver data post-flight (Greidanus & Santamaria 2014). Orbit position accuracy does affect the absolute location accuracy of radar images directly, with the orbital state vectors included in GRD and SLC products that have been determined “on-the-fly” using the onboard GNSS being significantly less accurate than precise orbits (Bourbigot et al. 2016). The accuracy of precise orbit ephemerides increases over time, being initially within 3 hours being near-real time, NRT, with 2D accuracy of < 10 cm, then within 20 days of measurement full precision non-time critical, NTC, ephemerides with 3D accuracy of 5 cm (Greidanus & Santamaria 2014). The precise orbits can be downloaded from ESA PDGS service, a process which S1TBX can do automatically (Guarnieri et al. 2015).

Radar images can be resampled either prior or after range-doppler terrain correction. GRD products are already resampled to a 10 × 10 m pixel spacing (Franceschetti & Lanari 1999). In downsampling, the raster pixel spacing becomes longer and the new pixel value is determined by aggregation methods such as first-, min-, max-, mean- and median. In oversampling a coarser grid becomes finer, and to determine each pixel's value methods such as bilinear interpolation and nearest neighbour can be used (Ulaby et al. 1981).

In a process called subsetting, a certain region of the radar image can be selected at any stage of the data processing chain, and the rest of the data is masked/removed or not processed further in later processing steps (Foumelis 2015). By subsetting only the area of interest, the amount of processing required is significantly reduced. In ESA SNAP, subsetting can either be applied for non-terrain corrected radar images and terrain-corrected rasters by either latitude-longitude coordinate bounds or pixel coordinate bounds (Foumelis 2015).

2.3.5 Water, ice and snow backscattering on C-band

For water surfaces without any heterogeneities such as oil or vegetation, backscatter signal is determined by water surface geometry (Shi et al. 2012). As inland waterbodies rarely feature long waves, the backscattering from lake and river surfaces is due to Bragg or resonance scattering. Due to water being a high dielectric medium, the penetration depth for C-band radar is only within a few millimetres and volume scattering is non-existent as compared to surface scattering (Jackson & Apel 2005).

Bragg scattering occurs on all water surfaces with a surface roughness meeting the relation of Eq. (3), by radio pulse undergoing resonant addition from returns from adjacent waves. Bragg scattering is not limited to water surfaces as compared to soil and manmade objects – in fact it was first discovered for radar remote sensing when backscattering from recently ploughed agricultural fields pointed at a right angle towards the radar having higher intensity than anticipated (Jackson & Apel 2005). Eq. (3) can be used to estimate the length of water surface waves in different incidence angles and SAR frequencies.

$$\lambda_B = \frac{\lambda_r}{2 * \sin(\theta)} \tag{3}$$

Where λ_B is the Bragg scattering short wave component of the water surface, λ_r the radar wavelength and θ the incidence angle (Fig. 24) (Jackson & Apel 2005).

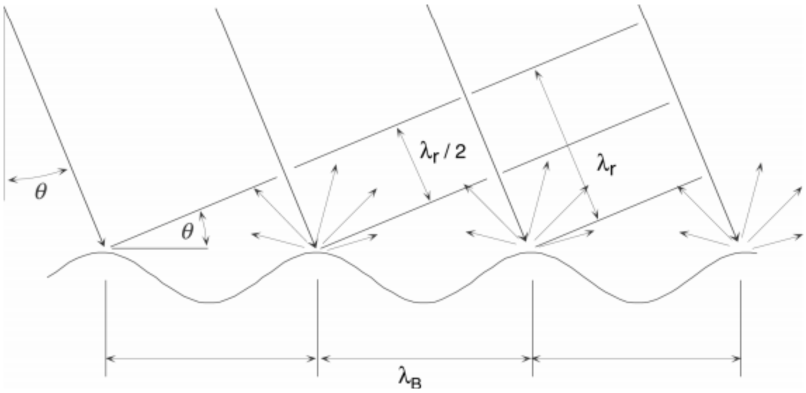

Figure 24 *Bragg scattering illustration (Jackson & Apel 2005).*

Waves caused by wind are however rarely discreetly distributed, featuring also resonant waves leading to most water surfaces affected by wind within the approximate threshold of Bragg scattering to feature the resonance. Also, for lakes wind speed varies along the water surface meaning even at higher wind speeds the Bragg scattering wind speed could be met at some point of the lake. As wind speed and directions vary along with the radar direction, shorter waves at an angle compared to the radar can also manifest Bragg scattering (Jackson & Apel 2005). Though resonant addition is the strongest in case Bragg waves are aligned along the radar direction, it can also occur at other wave directions in relation to the range-direction of the SAR satellite. As the water wave angle as compared to the range-direction of the SAR-illuminated area increases the wavelength required for Bragg scattering decreases (Jackson & Apel 2005).

For Sentinel-1 IW-mode, at the typical minimum incidence angle 29° Bragg scattering occurs at for waterbody wavelengths in varying direction in relation to the range-direction is around 6 cm or less, and for the maximum incidence angle 46° around 4 cm or less (Fig. 25). An incidence angle 30° has a water wave-length of ~5.5 cm and an incidence angle of 45° is around wave length of ~4 cm. For an incidence angle of 20° where corresponding Bragg-wavelength is around 7 cm, the threshold for wind speed to generate large enough ripples has been found to be equal or above 2.2 m/s (Jackson & Apel 2005).

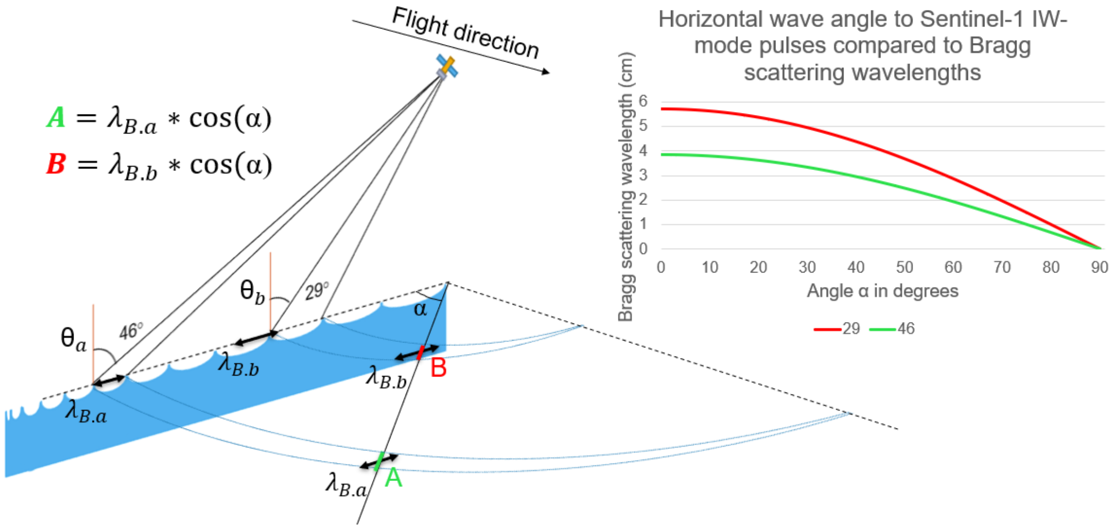

Figure 25 *Bragg scattering limits for Sentinel-1 lowest and highest incidence angles as the wave-angle changes as compared to range direction.*

During low winds at particularly at larger incident angles, C-band backscattering often falls below the noise floor for sigma0 for C-band returns. Horizontal polarization (HH) returns are several decibels lower as compared to vertical polarization (VV) returns except for lowest incidence angles (Jackson & Apel 2005). HV and VH backscattering from waterbodies on C-band has been found to be uniformly 5dB lower than HH, resulting in the backscattered signal to often fall below the noise floor (Jackson & Apel 2005).

As the season changes and lakes freeze, frozen waterbodies are generally covered either by snow or ice. Lake ice can be classified to several different types such as brash ice, pancake ice or new lake ice, though the distinction between snow and ice types is not always clear (Jackson & Apel 2005). Typically, more of the different types are featured in larger lakes (Nghiem & Leshkevich 2007). Ice type is mainly determined by how it is formed, such as present stresses by wind and temperature during freeze-up period (Leppäranta 2015).

Depending on the thickness, compactness, dielectric constant and other properties of ice, the relative contributions of radar scattering mechanisms such as rough surface scattering, specular reflections and volume scattering will vary (Dierking et al. 1997). Ice surface coarseness, crystalline features and gas bubbles greatly affect C-band backscattering (Nghiem & Leshkevich 2007). Ice can form ridges, changing the surface geometry of the ice and resulting in backscattering intensity typically higher than that of flat ice (Jackson & Apel 2005).

Dry snow layer can be penetrated by a radar pulse, and the dominant scattering mechanism may in fact be at a lower interface such as within the ice layer. Snow mass for dry snow has been found to feature little effect to C-band backscatter. For refrozen snow, volume scattering is the dominant scattering mechanism whereas for wet snow surface scattering is dominant. If a snow layer is inhomogeneous with varying densities and dielectric constants, volumetric scattering can be greatly increased as compared to homogenous snow (Schwaizer 2017). Scattering mechanisms for snow are shown in Table 6.

Table 6 *Radar scattering mechanisms for snow surfaces (Schwaizer 2017).*

Surface type	Dominant scattering mechanism	Dominant scattering factor	Less dominant scattering factors
Wet snow	Surface scattering	Liquid water content	Surface roughness (important), grain size (small effect)
Dry seasonal snow	Volume scattering and/or lower interface scattering	Medium below snow	Grain size
Refrozen snow	Volume scattering	Volume inhomogeneities, snow interfaces, for layers with different density	

In a scenario where scattering occurs from multiple layers such as a snow-ice-water layer present over frozen lakes, the scattering mechanism will be a combination of snow-surface scattering, snow volume scattering, ice-water interaction terms and snow-ice interactions (Duguay et al. 2015). One way of modelling this complex interaction can be modelled using radiative transfer equation (Phan et al. 2014). A phenomenon called frost flowering has been observed to increase C-band radar backscattering significantly, formed at temperatures significantly below zero above thin frozen freshwater or sea ice when ice is still thin (Isleifson et al. 2010).

2.3.6 Methods for classifying lake ice in C-band SAR data

In a study conducted by Los et al. (2016) comparing polarimetric X-band and C-band classification for freshwater ice, the two were considered to have similar capabilities for ice monitoring. In another study by Wakabayashi et al. (2015) comparing L-bands and C-bands for lake ice classification, C-band was found better at distinguishing lake ice. It was however concluded that lake ice types are difficult to distinguish using C-band SAR observations during significant ice melt in the top surface layer partially masking backscattering signatures from different ice types.

Based on the data gathered during the GLAWEX'97, Great Lakes Winter Experiment ′97, and later compiled by Nghiem et. al. (2007), different types of lake ice and calm water backscattering on C-band were measured at incidence angles between 14-62°. The study showed that calm water was well below the noise floor of both the Envisat and ERS (Fig. 26). As a target backscattering falls below the noise floor, its backscattering signature for the two would only feature the noise instead of actual measurements of the surface (Nghiem & Leshkevich 2007).

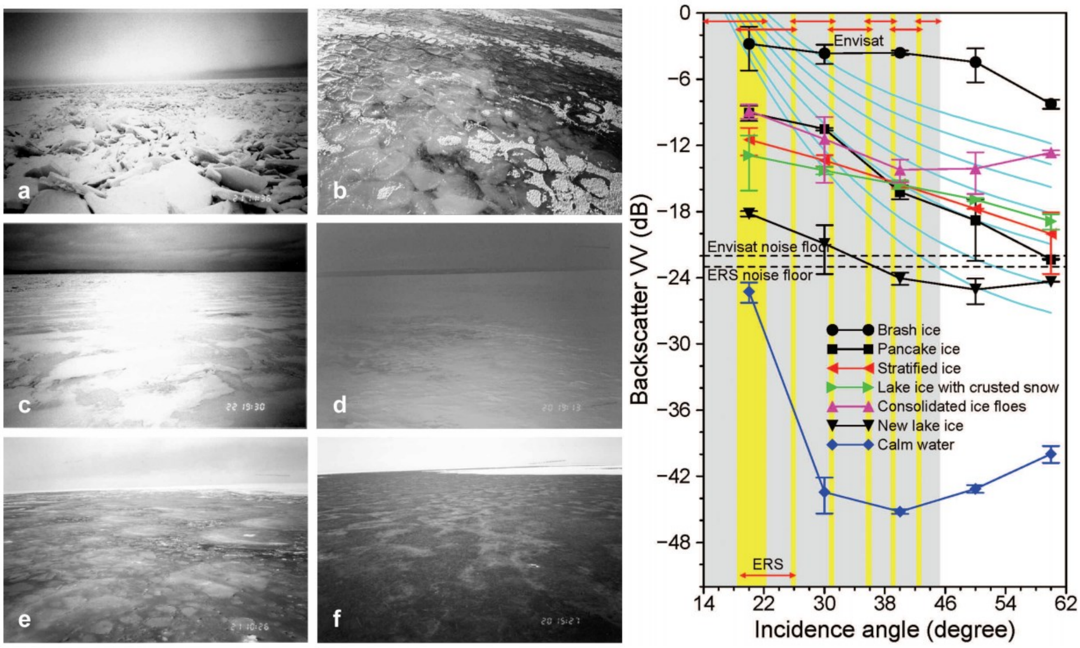

Figure 26 *Left: photographs of (a) brash ice, (b) pancake ice, (c) stratified ice, (d) lake ice with crusted snow, (e) consolidated ice floes, (f) new lake ice; right: corresponding backscattering at various incidence angles (Nghiem & Leshkevich 2007).*

Interferometric SAR or InSAR techniques can be used for monitoring snowmelt in addition to both glacial and sea-ice movement by using the phase information of two radar images from the same relative orbit (Schwaizer 2017). Snowmelt, or more accurately changes in snow cover resulting in return-phase to shift, can be detected by InSAR coherence changing over repeat pass satellite measurements. Ice movement is measured by phase-changes over repeat passes due to movement. The use of coherence is however limited for estimating ice phenology, as changes in the snow layer above seasonal ice are likely between radar image acquisitions, resulting in a high coherence that is indistinguishable from the coherence between open water and ice (Schwaizer 2017).

In a study conducted in 2013 by Sobiech and Dierking, C-band RADARSAT-2 were used to classify areas of lake and river ice decay. Based on backscattering intensity on HH, HV and VV polarizations, processed into geocoded sigma0 radar images with a 3 × 3 Lee-filtered pixel spacing of ~10 × 10 m, k-means based classification was found to be suitable to spatially classify between a water surface and an ice surface during the ice-decay period. The study however revealed that the method for classification was limited for both between wet ice and calm water, and with water surfaces with increased backscattering due to wind similar to that of the ice. RADARSAT-2 radar images in the study were also limited to a maximum incidence angle of 35° to avoid falling below the noise floor for the different polarizations (Sobiech & Dierking 2013).

For Sentinel-1 based sea ice concentration classification of the Baltic sea, a study was conducted by Karvonen et. al. (2017). Using Sentinel-1 EW-mode radar image HH and HV polarizations with removed thermal noise footprints were calibrated to sigma0. Several different grey-level co-occurrence matrix features were calculated at a grid of 100 meters and then resampled to a 500-meter grid and an automated classification was applied based on a neural network that was taught using operational ice-maps from FMI. Wind speeds for studied sea surfaces were 5 m/s and above. A good overall accuracy was reached, though some overestimation of ice concentration occurred over open water.

A study was conducted using radiometrically calibrated ERS-1 C-band data for small Alaskan lakes by Jeffries et al. (1993). The study found that sigma0 values are strongly dependent on whether a lake has frozen to the bottom or afloat – with a lake frozen to the bottom featuring considerably lower backscattering. When ice is afloat, the specular ice-water interface and vertically aligned tubular ice bubbles cause a strong backscatter. Thin and smooth lake ice caused a specular reflection away from the radar antenna and a weak backscatter. Dry snow was found to have little effect on backscattering, with underlying ice backscattering being dominant even when covered by a dry snow layer of 20 - 80 cm.

A study by Surdu et al. (2015) was conducted on shallow Alaskan lakes, where combined C-band sigma0 radar images from ASAR and RADARSAT-2 were used to measure ice phenological events. K-means based classification was shown to be generally suitable for discriminating between ice and open water. Freezing onset detection was found challenging due to effects of wind on radar backscattering and similarity of sigma0 on new lake ice and open water, while detection of complete freeze-over of lakes was found to be complicated for the variability of backscattering from both ice and snow. Reliable wind data observations were proposed for taking wind speed and direction effect on open water into account for improving freeze-onset detection. Use of future Sentinel-1 data were proposed for complementing other satellite missions by combining observations.

Use of RADARSAT was studied by Nghiem et al. (2007) for SAR remote sensing of large to very large lakes, where using only a single polarization in radar images was found to have limitations in distinguishing between different lake ice types and open water. This was due to the varying backscattering of open water via different wind speeds and directions, overlapping with range of backscattering expected of lake ice. In a study conducted by Geldsetzer (2010), combining VV and HH polarizations in a co-pol ratio was proposed for autumn freeze-up detection when using RADARSAT-2 data. Another study by Hindberg et al. (2013) found cross-polarity based RADARSAT-2 classification of smooth lake ice and open water to be prone to misclassifications, even when using in combination with co-polarized data.

2.3.7 Copernicus Sentinel-1 mission, the related products and applied tools

Sentinel-1 mission consists of a constellation of several C-band SAR-satellites to meet the observational needs of the European Union ESA Copernicus programme, formerly Global Monitoring for Environment and Security, GMES. Sentinel-1 mission is planned to maintain the levels of spatial resolution, accuracy, sensitivity, polarization and wavelength of the ESA’s successful ERS-1, ERS-2 and Envisat missions. Some of the crucial requirements for operational services based on the SAR data of Sentinel-1 constellation are data continuity, frequent revisits, geographical coverage and timeliness (Gade 2015). Detailed specifications for the satellites are shown in table 7.

Sentinel-1 provides near real time data delivery within an hour after reception, and data delivery via archive within 24 hours. Currently there are two satellites in the Sentinel-1 constellation, Sentinel-1A launched 2014 and Sentinel-1B launched 2016 (Gade 2015). All current Sentinel-1 satellites carry a payload called C-SAR payload developed by Astrium UK, operating at a frequency of 5.405 GHz (ESA 2007).

A wide variety of data is available from various measurements completely free, openly accessible to programme’s data users. To list a few monitoring and emergency applications for the satellites – monitoring sea-ice zones and the Arctic, marine environment surveillance, land movement mapping, land surface mapping such as water and soil, agriculture, forests and humanitarian aid related mapping in crisis situations (ESA 2007).

Table 7 *Sentinel-1 specifications* (ESA 2007).

Characteristic	*Values*
Lifetime	7 years (consumables 12 years)
Launcher	Soyuz from Kourou (baseline), Zenith-2 (backup)
Orbit	Near-polar Sun-synchronous 693 km, 12-day repeat cycle, 175 revs per cycle
Mean Local Solar Time	18:00 at ascending node
Orbital Period	98.6 minutes
Attitude stabilization	3-axis
Attitude accuracy	0.01 deg (each axis)
Orbit knowledge	10 m (each axis, 3-sigma) using GPS
Operating autonomy	96 hours
Launch mass	2300 kg (including 130 kg monopropellant fuel)
Size (stowed)	3900 × 2600 × 2500 mm

Solar array average power	4800 W (end-of-life), battery capacity >300 Ah
Spacecraft availability	0.998
Science data storage capacity	900 Gb (end-of-life)
S-band TT&C data rates	4 kbit/s telecommand, 16/128/512 kbit/s telemetry (programmable)
X-band science data rate	600 Mbit/s

Sentinel-1 has four standard operational modes.

- Strip Map Mode (SM), 80 km swath and 5 × 5 m spatial resolution. SM is normally used to image small islands.
- Interferometric Wide Swath Mode (IW), 250 km swath and 5 × 20 m spatial resolution, burst synchronization for interferometry. IW mode uses three subswaths using Terrain Observation with Progressive Scans or TOPSAR. IW is the default acquisition mode over land.
- Extra-Wide Swath Mode (EW) with a 400km swath and 25 × 100 m spatial resolution. EW is primarily used for monitoring coastal areas.
- Wave mode (WV), varying swath at 5 × 20 m spatial resolution. This mode samples images of 20 × 20km at 100 km intervals along the orbit, resulting in a low data rate. Default mode for acquiring data over the ocean, using VV-polarization.
  (ESA 2012)

Sentinel-1 products are offered in three different levels of processing and four product types. First of the product types is the level-0 raw-data, including non-compressed and non-focused raw SAR data. Metadata includes data regarding the noise, internal calibration and echo packets, the orbit and the attitude during acquisition. All other products are processed from this data, and some of the metadata such as the orbit and attitude are inherited to later level-1 products (Miranda & Rosich 2011).

- Level-1 SLC, Single-look Complex products are compressed and focused SAR-data featuring a single look in each dimension using complex samples (real and imaginary) to conserve phase information, using full signal bandwidth. Data has been georeferenced using satellite orbit and attitude data.
- Level-1 GRD, Ground Range Detected data are also compressed and focused SAR-images. The main difference between SLC is that GRD has been both multilooked and projected using WGS-84 ellipsoid model, resulting in square pixels. Phase information is lost, with only backscattered amplitude remaining as a value for each pixel.
- Level-2 OCN, Ocean products offer geolocated geophysical products for Ocean surfaces derived from level-1 products. Typically, this consists of ocean wind, wave and currents, with product components varying by the used acquisition mode.
  (Miranda & Rosich 2011)

Except for Wave-mode, all three product types are offered for all four operating modes. All products offer metadata, such as data acquisition parameters, and level-1 products include calibration vectors for radiometric backscatter calibration (Miranda & Rosich 2011).

Single Sentinel-1 satellite has a 12-day repeat orbit. As polar-orbiting satellites, their orbits will intersect near the poles, providing a higher revisit time around the poles as compared to lower latitudes (Fig. 27). As an example, using an IW-mode 250 km swath width the revisit period will be less than a day for a single satellite near the northern and southern poles (ESA 2007).

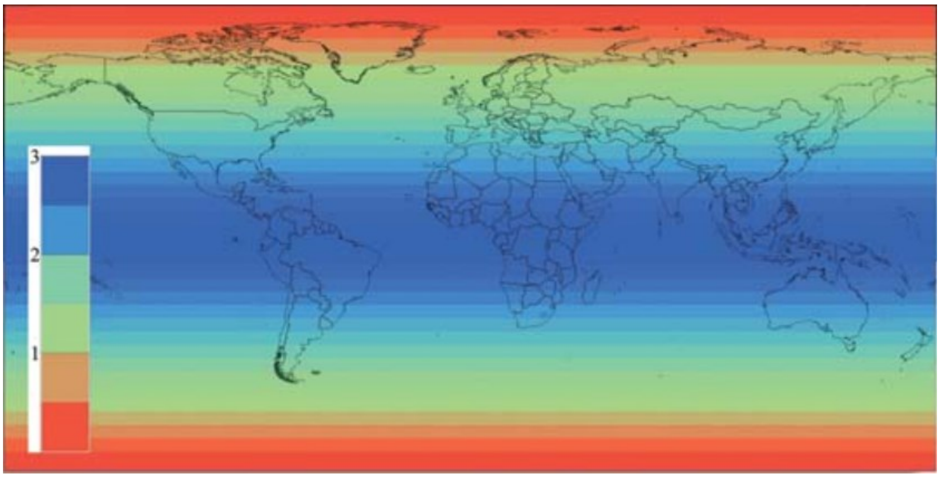

Figure 27 *Worldwide repeat orbit interval of a single Sentinel-1 satellite (ESA 2007).*

ESA SNAP is an open-source application for processing remote sensing data. The development is funded by ESA Scientific Exploitations of Operational Missions department or SEOM. An optional plugin with radar processing tools available for the ESA SNAP is the S1TBX, which includes a wide variety of tools specific for radar image processing (Brockmann & Fomferra 2015).

The official Copernicus Programme data archive for accessing Sentinel-1 data is called the *Copernicus Open Access Hub* (accessible at https://scihub.copernicus.eu/). The archive service allows users to specify and download any number of datasets available in the archive. As searched in mid-September 2018, the amount of Sentinel-1 GRD-products exceeds as many as one million with all available archived EW, IW, SM datasets combined.

3 Methodology

3.1 Overview of the study area, waterbodies and used data

Two separate study areas (Fig. 28) are used for assessing the developed lake phenology method presented in this thesis. Sides of these two areas cover few tens of kilometres in latitude and longitude, with lake study area located near Hämeenlinna city with four lakes and river study area containing two river portions of Kokemäenjoki near Pori city. All above lakes belong to the main catchment area of Kokemäenjoki. Freeze-up and break-up observations vary between the waterbodies, listed in table 8.

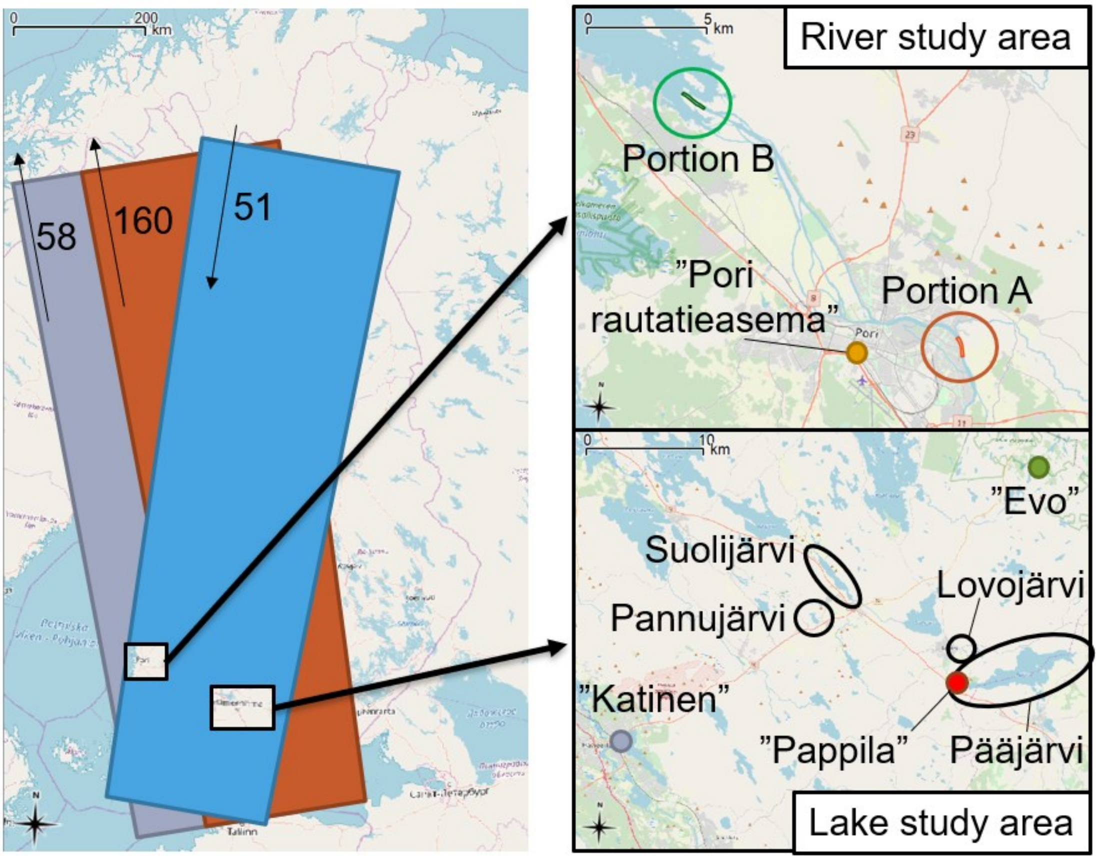

Figure 28 *Left: relative orbit footprints and study areas located in Finland; right: study areas with studied waterbodies circled and closest weather stations marked as dots. Background maps using OpenStreetMap.*

Lake Pääjärvi is the largest of the studied lakes with an area of 13.5 km^2 and is considered a medium size lake in Finland. It is one of the deepest lakes in Finland with a maximum depth of 87 meters, with average depth being 14.4 meters (Lake and Sea Wiki 2018). In a study related to Lake Pääjärvi ice phenology by Kärkäs (2000), the lake was observed to freeze near its shorelines before the whole lake freezes, a phenomenon which is due to the lake’s depth and size. Ice break-up and freeze-up observations have been conducted at the lake in 1910-1930, 1971-1988 and briefly in winter of 1992-1993, though break-up and freeze-up data are not currently being collected. Ice thickness measurements are currently being made during the frozen period of the lake in its’ westernmost part every tenth day of winter months (Kärkäs 2000).

Lake Suolijärvi is located North-West from lake Pääjärvi, has maximum depth around 10 meters and average depth around 4.7 meters. Its total area is around 2 km^2. The lake has a distinct, elongated shape being around 4.5km long but only around 700m at its widest. By its diameter, it falls in a category between the medium-size and small-size lakes (Lake and Sea Wiki 2018). Detailed third party ice freeze-up and break-up observations conducted by Vanajavesikeskus from lake Suolijärvi found in appendix 3.

Lake Pannujärvi is a small lake with a total area of 36 ha and its' deepest point around 12 meters. It is a headwater and is located at a higher elevation than nearby lakes (Lake and Sea Wiki 2018). Pannujärvi was observed using cameras and other sensors over autumn 2017 - spring 2018, presented in section 3.2. An oxidization pump was installed to the southern end of the lake during February 2016 (Mäkelä 2016). Ice near the pump has been observed to cause a large open water area in late spring during the observation period of the Pannujärvi measurement station in winter 2017-2018.

The fourth and last studied lake called Lovojärvi or Lovonjärvi is the smallest single waterbody area and smallest lake studied in this thesis, with a total area of only 4.5 ha. There are no ice phenology observations conducted at this lake (Lake and Sea Wiki 2018). By its size, its classified as a very small lake.

There are two river portions being analysed (Fig. 30), both being part of river Kokemäenjoki located in western Finland near Pori city. Kokemäenjoki has a total length of around 121 km and an average volumetric flow rate of 240 m^3/s. Its widest portions near its discharge to the Baltic sea are up to 400 meters wide (ELY-keskus, kalatalouspalvelut 2018). The river has a tendency for flooding over springtime during ice break-up period (Vuola 2013).

River portion B is located at the location where the river discharges to the sea, while portion A is located inland at a relatively wide portion of the river around 20 km inland from portion B. Both portions are around 100-150 meters wide and around one kilometre long, shown in figure 28. No freeze-up and break-up data is available for the two river portions.

Table 8 *Ice phenology observations and their source for each waterbody.*

Study area	*Waterbody*	Observation type	*Freeze-up and break-up date accuracy*	Source
Lake	Pääjärvi	Ice thickness	Not directly applicable	Finnish Environment Institute API
Lake	Suolijärvi	Third party freeze-up/break-up	Within a few days	Vanajavesikeskus
Lake	Pannujärvi	Pictures from sensor station	Within minutes (excluding data gaps)	Sensor station as part of this thesis
Lake	Lovojärvi	None	None	-
River	Portion A	None	None	-
River	Portion B	None	None	-

3.1.1 Overview of meteorological data used for the studied waterbodies

Different meteorological observations are used either from few select FMI weather stations in close proximity of the studied lakes (Fig. 30) or all available stations in Finland. The data is initially acquired from the FMI api via the WFS-service encoded as GML.

FMI weather station wind sensors are placed at sufficient heights from the ground level in order to minimize the effects of vegetation and manmade structures in the wind measurements, generally at least at 10 meters. Temperatures at FMI stations are measured at a height of 2 meters, within a screen that protects the thermometer from sunlight (Piirinen et al. 2012).

Pannujärvi wind conditions being assessed in section 3.2.3 are using wind data from the closest two stations, FDD/TDD values being calculated using temperature measurements in section 3.3.4 from the closest corresponding station and wind field interpolation being applied in section 3.3.3 use all available weather stations measuring wind. The corresponding stations and data types are listed in table 9.

Table 9 *Meteorological observations used for waterbodies studied in this thesis.*

Study area	*Waterbody*	*FMI stations used to calculate Pannujärvi wind conditions*	*Temperatures from FMI stations used to calculate F*DD/TDD values	*FMI stations used for wind field interpolation*
Lake	Pääjärvi	-	"Pappila"	All available
Lake	Suolijärvi	-	"Pappila"	All available
Lake	Pannujärvi	"Evo", "Katinen"	"Pappila"	All available
Lake	Lovojärvi	-	"Pappila"	All available
River	Portion A	-	"Pori Rautatieasema"	All available
River	Portion B	-	"Pori Rautatieasema"	All available

3.1.2 Regarding the selection of IW-mode over EW-mode

Both EW-mode and IW-mode were presented in chapter 2, though IW-mode is used exclusively as compared to EW-mode in this thesis. There are two main reasons for using IW-mode over EW-mode in the scope of this thesis.

First, the pixel spacing of 100 meters for EW-mode restricts its' use for very small lakes such as lake Lovojärvi and other narrow waterbodies such as river portions in the river study area. Second, the method presented in more detail in section 3.4 requires a relatively high number of radar image acquisitions over known open water period for each used relative orbit, which are not available for EW-mode in the study areas (Fig. 29).

For comparison between the EW mode and IW mode, acquisition segments collected during 2017 covering Scandinavia were downloaded from the ESA website. Summing overlaying areas, then converting the resulting polygon to a raster format and finally dividing each pixel value of the raster by 52 gives differences between number of weekly acquisitions for different areas in Finland for EW (Fig. 29) and IW (Fig. 30).

Additionally, if the method were to be applied to lakes in northern parts of Finland using EW-mode, the lack of acquisitions during both winter and summer would make its' use not applicable. The difference in southern and northern Finland EW-acquisitions can be explained by the EW-mode being on sea ice monitoring for the Baltic sea but switched to IW-mode over inland areas.

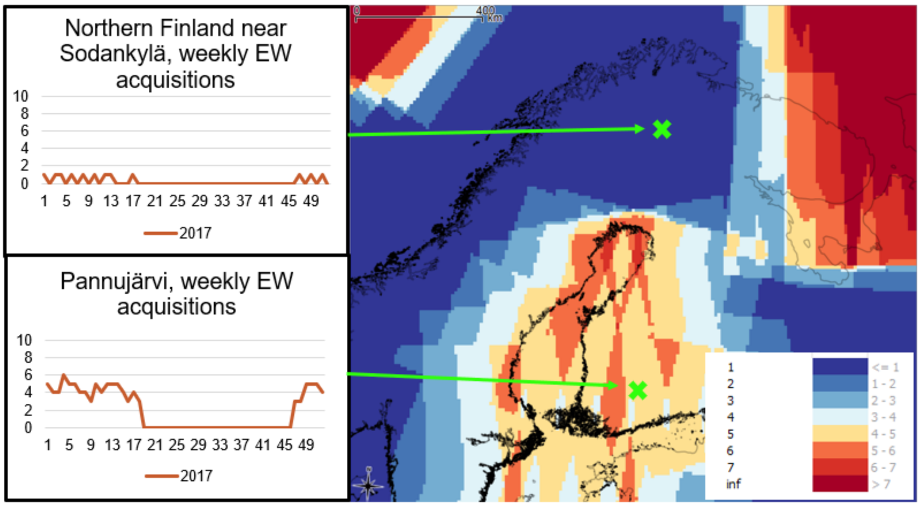

Figure 29 *EW acquisitions on average acquisitions per week (map colour), and comparison of the weekly acquisition rate for two locations in southern and northern Finland.*

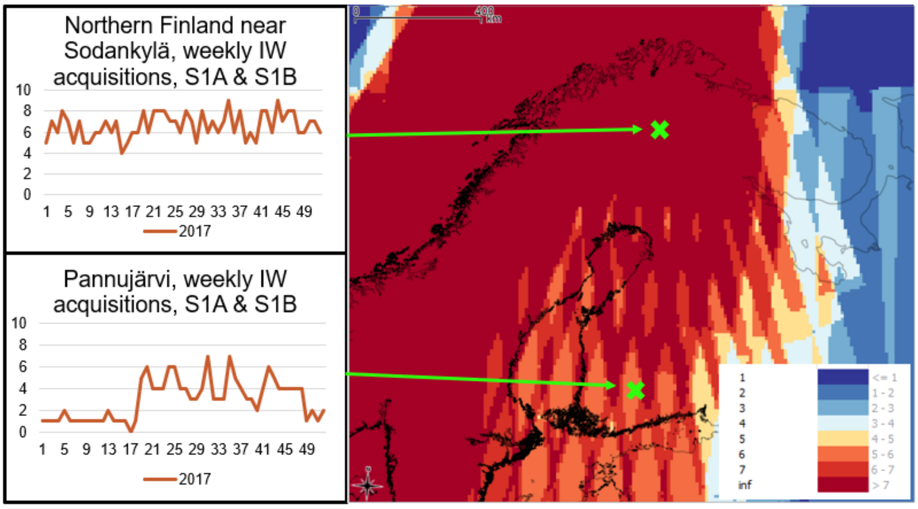

Figure 30 *IW acquisitions on average acquisitions per week (map colour), and comparison of the weekly acquisition rate for two locations in southern and northern Finland.*

3.2 Ice phenology measurements at lake Pannujärvi

3.2.1 Background and system overview

To ensure an adequate amount of data was to be used for different options of applicable methods of radar data processing for ice phenology and to determine freeze-up and break-up periods of a single lake to a greater accuracy than manual observations, a novel measurement station was established by integrating commercially available sensors and components.

The system was installed to the eastern shore of lake Pannujärvi. This lake was chosen by both offering existing facilities in providing DC power, ease of access via roads and the lake being a typical presentation as a typical small lake as compared to manual observations of lake freeze-up and break-up being typically conducted on lakes of medium size and larger.

The complete setup is presented in this section; however, the focus of this thesis is on using data collected by the weather station (wind speed, gust speed and direction) and the images gathered by the cameras. Full list of the system sensors is given below.

- Wireless wind meter (868 MHz)
- Wireless temperature sensors in a semi-submersible pole (868 MHz)
- Wireless rain gauge (868 MHz)
- 2D laser scanner, SICK TiM-551 (ethernet)
- Battery-operated camera (Camera 0) operated during autumn 2017 until 28.11.2017
- Gimbaled high-FOV camera (Camera 1) pointed towards the west (ethernet)
- Fixed high-FOV camera (Camera 2) pointed towards the south (ethernet)

Most sensors were installed on December 9th, 2017. Temperature pole was installed around mid-December after ice thickness reached 5 cm and was solid enough to stand on. A computer (Intel computing stick) operates the sensors and the system is powered by external AC-power. Internet connectivity is achieved via 4G router. Sensitive electronics, AC-DC power converters, relays and the main computer are placed inside an IP65 rated plastic box. Out of this box, ethernet cables and the AC cable go through the box via waterproof panel mounts. A full system chart can be found in Appendix 2.

Temperature-time relay control the power to the cameras and the laser scanner. They are turned off automatically if the outside air temperature falls below -25 C°, since this is lowest stated operating temperature for the laser scanner and the used cameras. System will re-power itself automatically in case of power outage occurs automatically and uses regular DC power from an external power outage for power. Full system power and network charts can be found in the appendices, while the locations of installed sensors and the location in relation to the lake can be seen in figure 31.

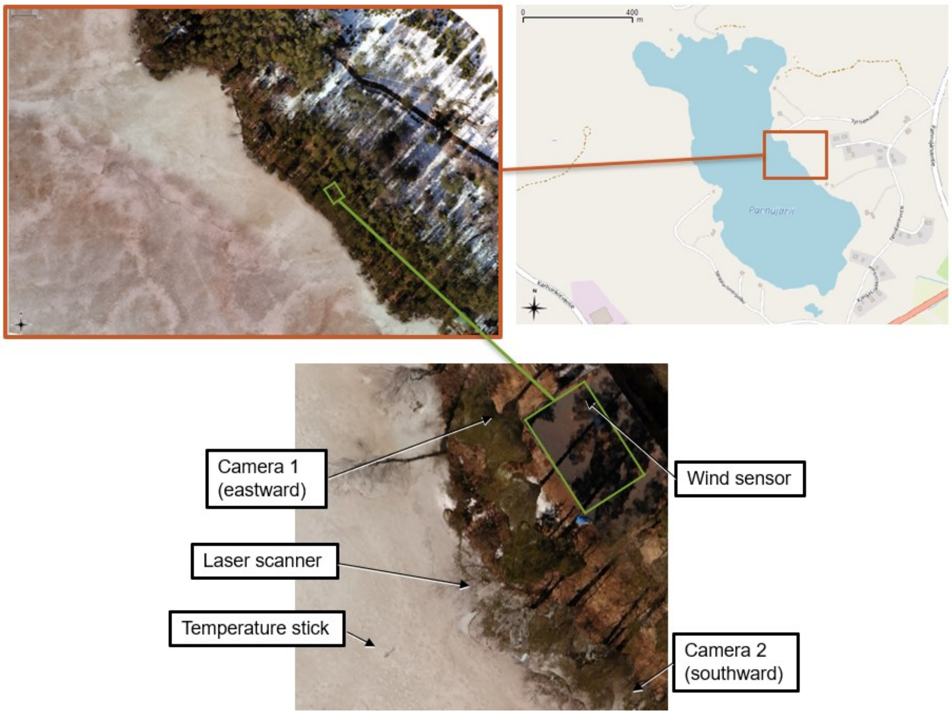

Figure 31 *Top-right: Location of sensor station in OpenStreetMap view; top-left: closer view in a drone aerial image; bottom: detailed locations of sensor placements in drone aerial image.*

The installation location of the wind sensor was ~20 m inland on top of a ~4 m high flat roof on top of a ~1.5 m pole. The location was not optimal for measuring unobstructed flow of wind but did offer the possibility to study the local similarity and sheltering of wind from the North-Eastern direction while South-Eastern direction was relatively unobstructed. Local wind was measured to measure local maximum wind speed, average wind speed and wind direction every 7 minutes. The wind direction is split into 15 sectors, at a multiple of 22.5° starting from 0/360° equalling north.

A temperature pole was to be intended to gather data on the temperature gradient above and underneath the ice. This data was intended to be used to determine the layering and depth of ice, slush and snow by the measured temperatures. There are 13 waterproof thermistors in total, with sensitive electronics within a waterproof casing and featuring visible length markings (Fig. 32). The system is similar as used in the study conducted in by Ohata et al. (2017) studying lake ice thickening processes.

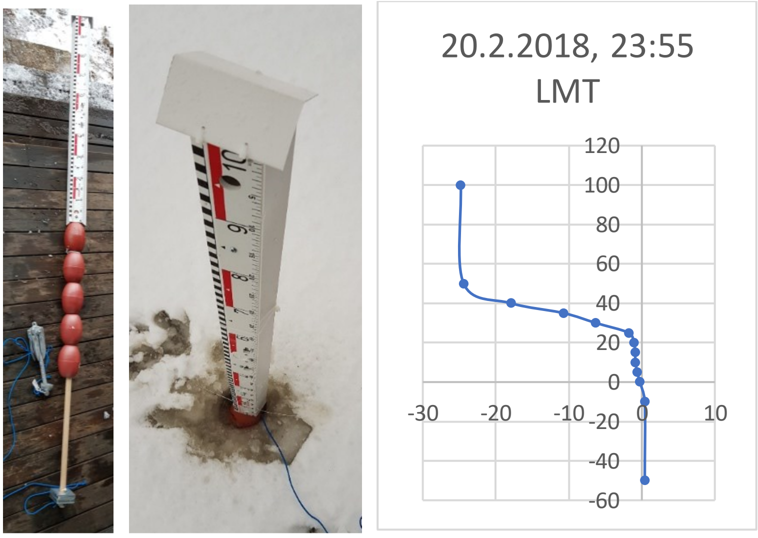

Figure 32 *Left: temperature pole prior to installation; middle: temperature pole after installation; right: data extracted for date 20.2.2018 at 23:55 local time, with horizontal scale indicating measured temperature (°C) and vertical scale in temperature sensor elevation (cm) from the lowermost ice surface.*

Single battery-operated camera gathering data from the lake since late-Autumn 2017 taking pictures every 6 hours until failing after midday of 28.11.2017. Two new cameras were installed 8.12.2017, taking pictures every 5 minutes with a higher FOV and quality. The cameras are placed in trees with slight overlap between the two (Fig. 33). Camera 1 faces approximately south-west and was installed to ~5 meters above the ground to a tree and was programmed to turn at regular intervals for a wider range of images. South-facing Camera 2 took pictures from around ~3 meters above the water surface, also being installed to a tree.

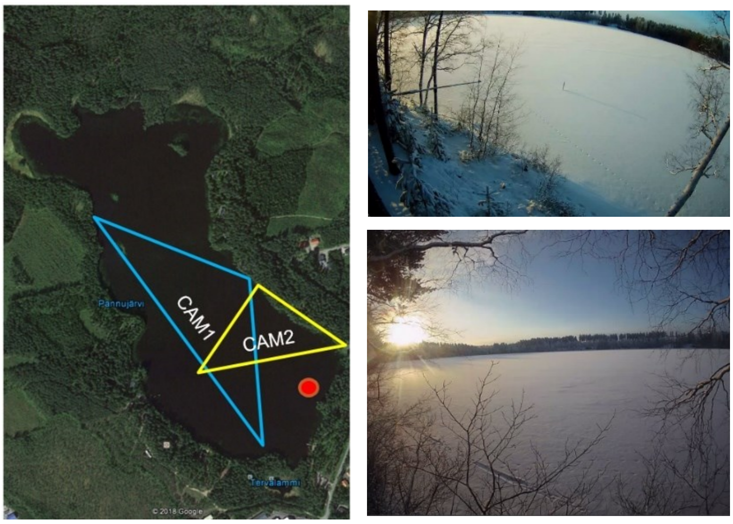

Figure 33 *Left: camera field of views on Google Earth base map with red dot indicating the oxidization station location; top-right: camera-1 example image; bottom-right: camera 2 example image.*

A SICK TiM-551 laser scanner was placed to ~2 meters above the lake surface, ~2 meters from the lake shore on a wooden pole covered by a plastic hut ensure no snow accumulates in the field of view of the scanner (Fig. 34). The laser scanner was turned on every two hours for 15 minutes, and laser scans were conducted at 5-minute intervals during these time windows.

The laser scanner was intended to measure the snow-ice surface properties such as the coarseness, reflectivity on IR-wavelengths, changes in snow depth and possibly even lake water surface geometry during the open water period. The scanner is capable of measuring distance up to ten meters and intensity values every 0.333° in a total opening angle of 270°.

Figure 34 *Left: laser scanner before installation; right: after installation above the lake using a wooden pole.*

It was noted after ice break-up that the laser scanner was not suited for measurements of the water surface geometry, as the laser penetrated the water surface without reflecting from the surface. It was however capable of measuring changes in snow reflectivity, snow depth and even detecting snowfall due to reflections from snowflakes.

The measurements for the station were conducted up to several weeks after ice break-up. The setup was uninstalled and prepared for storage around midday local time of 09.05.2018.

3.2.2 Timeline on ice phenology events of lake Pannujärvi

The images from the cameras were used to deduct ice phenology events of lake Pannujärvi over the course of winter of 2017-2018. The complete timeline is shown in Fig. 35.

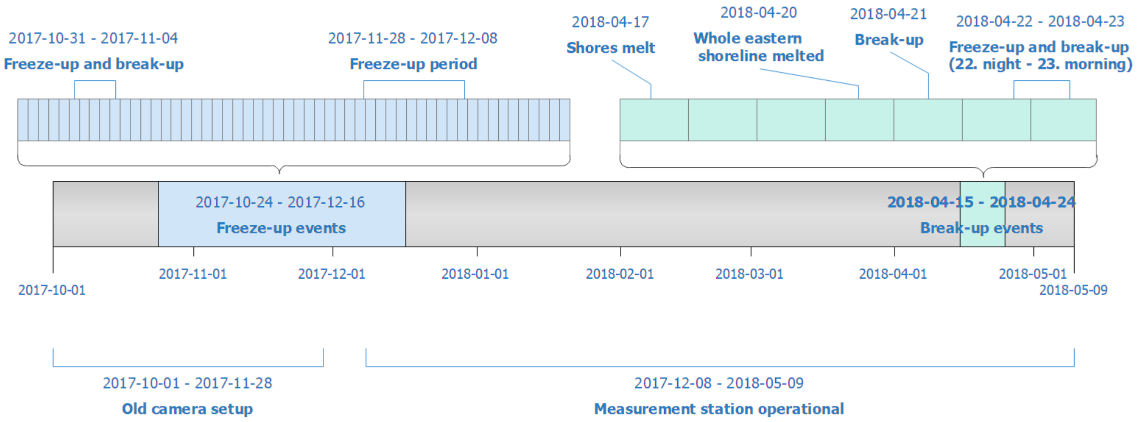

Figure 35 *Lake Pannujärvi ice phenology for winter 2017-2018 determined using the old camera and two new cameras.*

The old, battery operated camera failed to take images between 28.11.2017 and until the new cameras were installed on 8.12.2017. Over the course of this period, the lake had frozen, resulting in a 10-day duration when the freeze-up had occurred.

The lake underwent thawing (Fig. 36) during spring 2018 starting from shorelines becoming open water at the camera-side 17.4.2018, after which the thawed shoreline expanded to a distance of around 10-20 meters from the shore until 20.4.2018. Lake ice broke up during moderate wind speeds on the 21st of April, and lake had ice floes present until the 24th. The northern end of the lake not covered by the cameras was presumed to be either ice free or nearly ice-free the 24th.

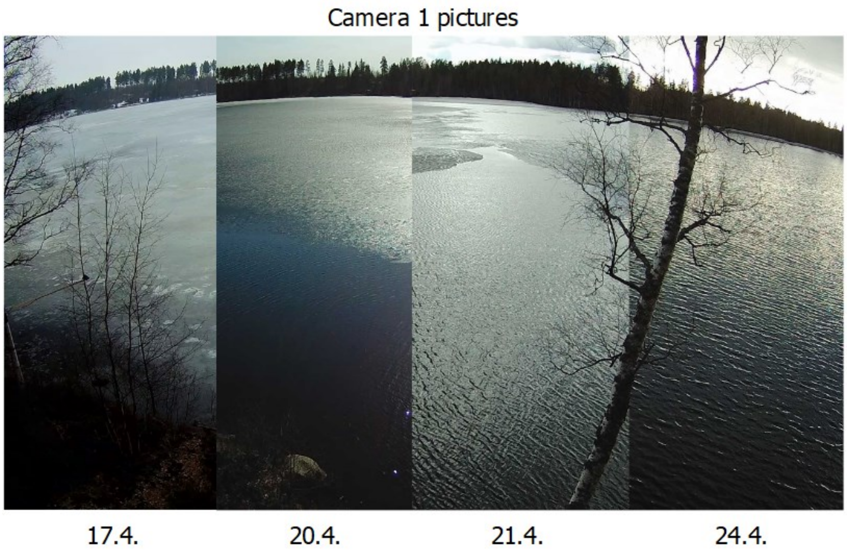

Figure 36 *From left to right: ice thawing over 17.4.-20.4.2018, break-up on 21.4.2018 and ice-free date at 24.4.2018*

The old camera captured a brief lake freeze-up over the night of 31.10. – 1.11.2017. The freeze-up occurred over a cold night with calm wind followed by few days of negative average temperatures. The ice break-up and the lake being free-of-ice occurred after daily average temperatures went well above zero. Similar temporary seasonal ice was noted in the images over spring over the course of night of 23rd of April - after the ice formed last December had underwent break-up and only few ice floes remained. Over a cold, calm night the lake fully froze-up and promptly broke up around midday the same day. During the evening of the same day, the broken ice floes had already fully melted. The events are shown in Fig. 37.

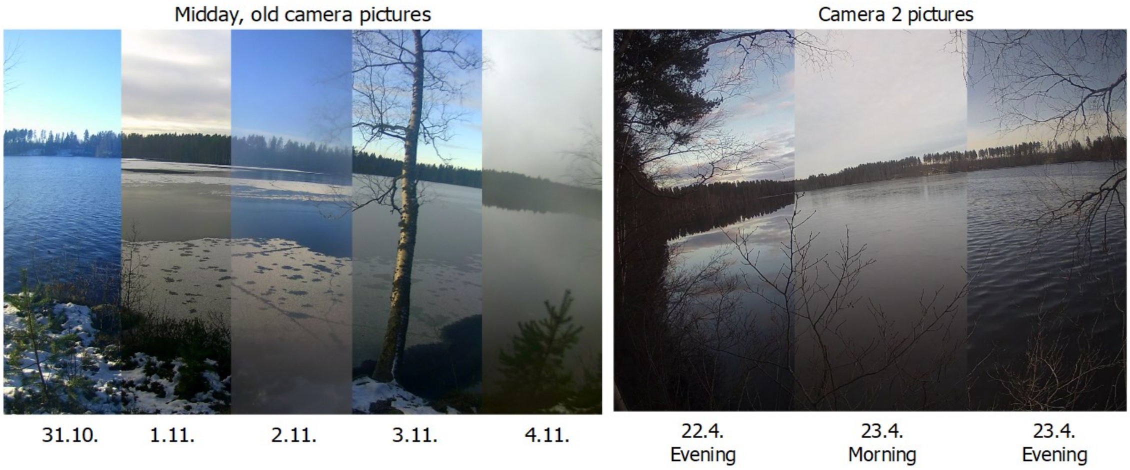

Figure 37 *Left: lake Pannujärvi briefly frozen and thawed during autumn of 2017 prior to main freeze-up; right: frozen after main ice break-up during spring 2018.*

3.2.3 Wave similarity in similar wind conditions at lake Pannujärvi

The method described in this thesis is based on the hypothesis that similar wind conditions for waterbodies result into similar wave conditions, which in turn result in similar SAR backscattering from the waterbody surface at the exact moment of acquisition. Therefore, few examples are analysed in the results chapter where the interpolated wind values are compared against images and against local wind measurements of Pannujärvi. Following data is used.

- Wind measurements from Pannujärvi measurement station
- Wind measurements from “Hämeenlinna Lammi Evo” and “Hämeenlinna Katinen” FMI weather stations over April – May 2018
- Images from camera 1 and camera 2 from Pannujärvi measurement station

Wind data used were interpolated between the two closest stations Lammi and Katinen stations by averaging the measurements. Lake Pannujärvi is located approximately between the two stations, so averaging the wind direction (wd), wind speed (ws) and wind gust speed (wg) is considered well justified.

Changes in the lake surface waves of lake Pannujärvi within a time window of 5-10 minutes happen relatively slowly, except for gusty wind conditions. The gustier the conditions, the less evenly distributed the waves were causing rippled areas at seemingly random locations. This phenomenon was only observed when wind speeds exceeded 1 m/s but was less than 4 m/s. Beyond 4 m/s areas of ripple were visible but barely discernible, as the lake surface waves were visually evenly distributed beyond the sheltered areas. As expected, as the wind speed grew so did the waves grow, while it was also possible for completely calm water surfaces to also occur (Fig. 38).

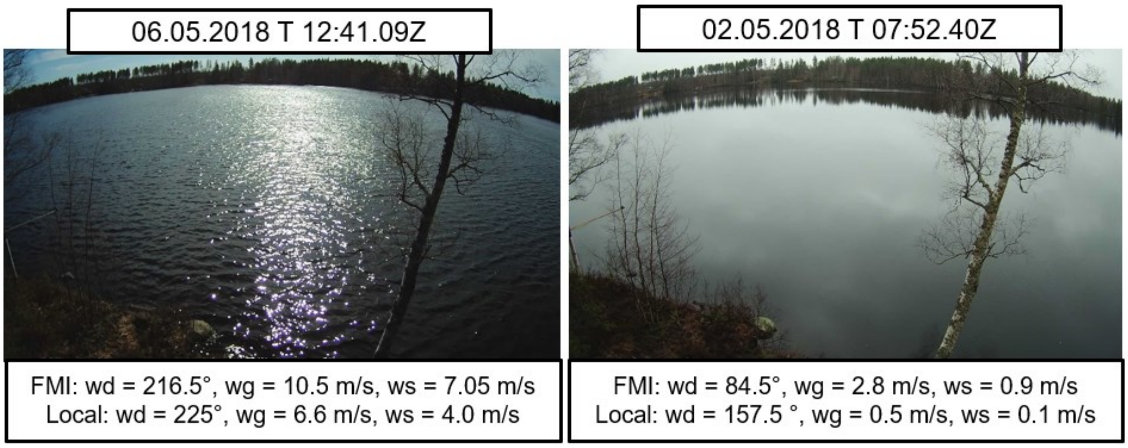

Figure 38 *Left: lake Pannujärvi lake surface during moderate wind conditions; right: during calm wind conditions seen from camera 1.*

The wind sheltering effect was also observed in most of the images, especially noticeable in the opposite facing side of the lake (Fig. 39). Taller, thicker vegetation caused longer sheltered areas in comparison to short vegetation. As the wind direction and speed changed, the sheltered area also varied considerably in the images.

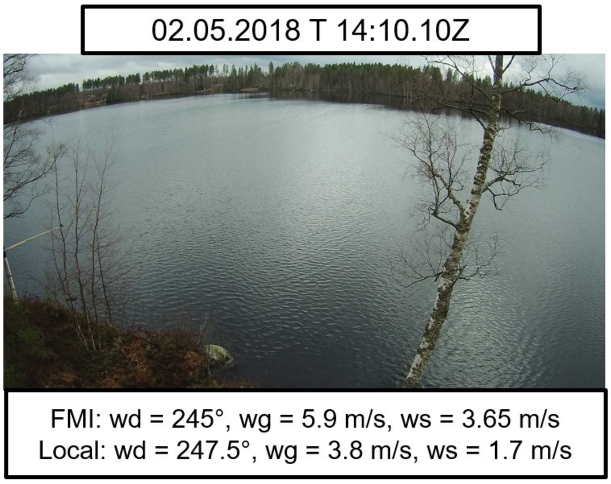

Figure 39 *Wind sheltering effect clearly visible at the opposite end of the lake. Wind is flowing approximately from South-West, a direction towards camera 1.*

At the exact moment of observation, the locally measured wind speed and gust speed values are expectedly lower as compared to interpolated weather station values. However, the wind speed and gust speed measured locally by the station are also similar when the FMI wind conditions are similar. An important factor for the developed method is that during these similar wind conditions the waves also feature similarity, which was observed in the camera images. Wind-wave similarities are demonstrated in Fig. 40.

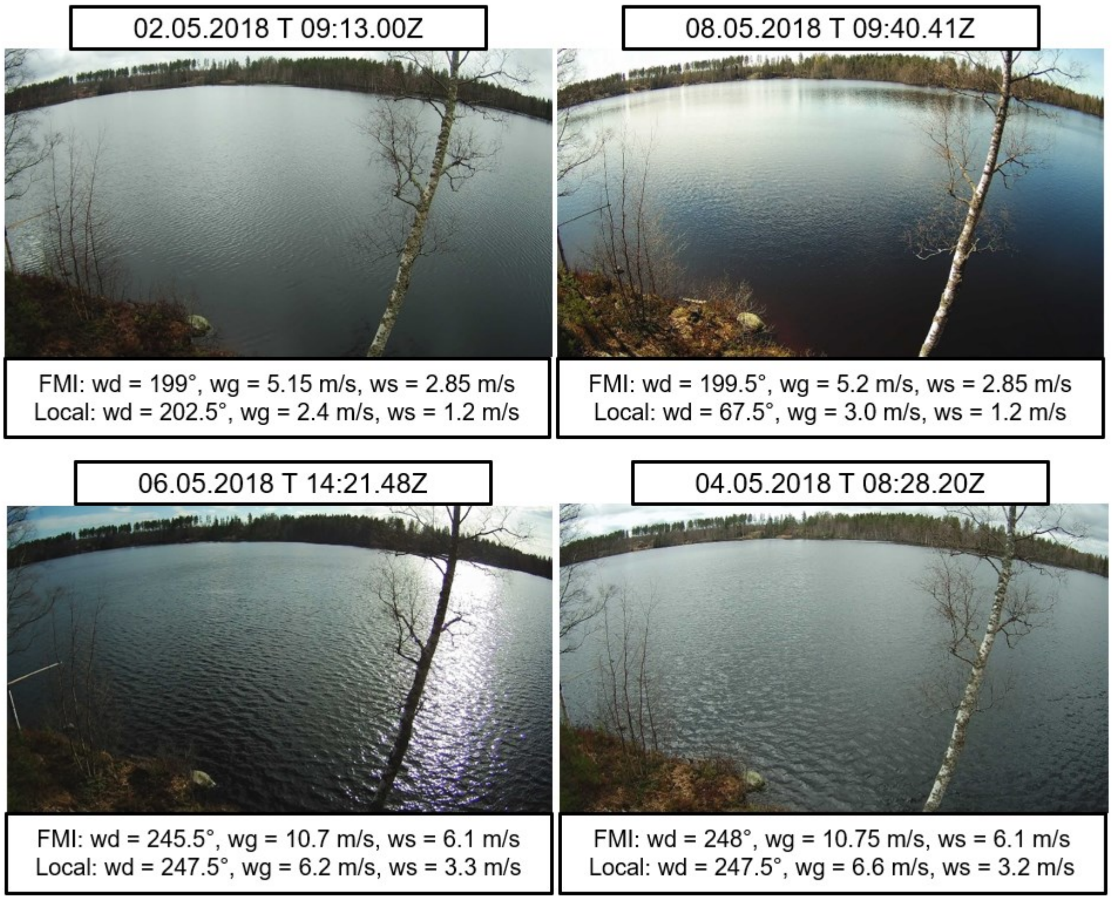

Figure 40 *Noting the similarities following interpolated FMI wind values in comparison with similarities in local measurements. Top left and right: similar nearly calm wind conditions; bottom left and right: similar moderate wind conditions.*

The changes to the water surface by rain were also observed. For wind conditions similar both to the local measurements and FMI weather observation interpolated data, even light rain was seen to completely change how the water surface ripple looked (Fig. 41). The effect was however seen to be less for higher wind speeds, where the waves are more pronounced in comparison.

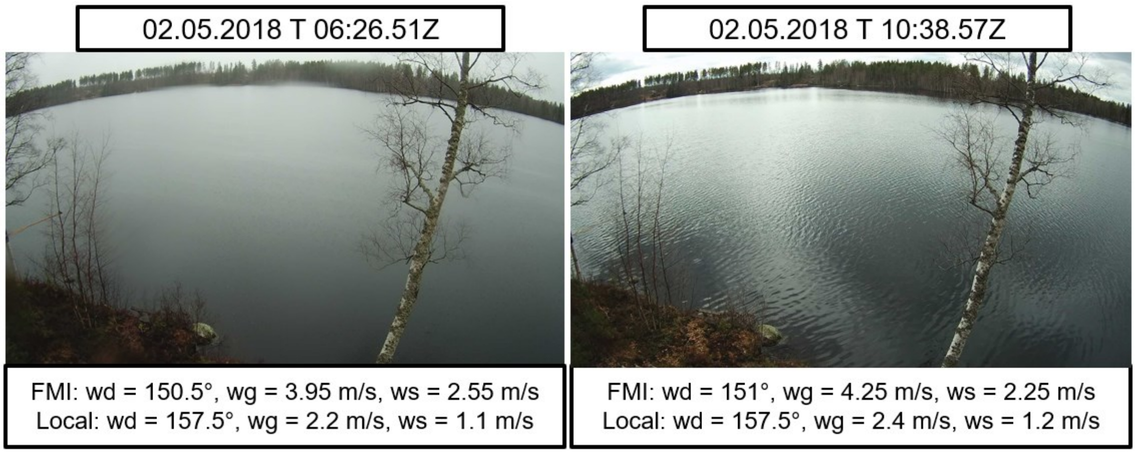

Figure 41 *Images of similar wind conditions. Left: during light rain; right: no rain.*

3.3 Data pre-processing

3.3.1 DEM and Jarvi-10 polygon preparation

NLS 10m DEM uses the N2000 height system. For use in ESA SNAP which requires DEM's to have heights above the WGS84 ellipsoid, N2000 heights were converted to GRS-80 ellipsoid using a FIN2005N00 geoid. The geoid in a polynomial format was converted to a raster format, then applying an addition between the two heights (Saaranen et al. 2006). The difference between the two ellipsoid is small enough for GRS-80 ellipsoid heights to be used in place of WGS84 ellipsoid heights (Louis 1986). The following data is converted to a "Geoid-corrected 10-m DEM" in GIS software, used in section 3.3.2.

- NLS 10m DEM, acquired via NLS open access portal in June 2017
- FIN2005N00 geoid, acquired from http://coordtrans.fgi.fi/

Waterbody areas of interest were selected from the Jarvi10 and River10 areas by their respective waterbody ID's, and rest of the areas were filtered out. To create a mask for radar rasters, a negative buffer of 50 m was applied to the selected lake areas and 30 m for river areas, resulting in later steps in masking leaving out any pixels containing land, manmade water structures or thick shoreline vegetation such as reeds (Fig. 42). Using the following data, "Buffered Jarvi-10 polygons" and "Buffered River-10 polygons" are formed used in section 3.3.2. using GIS software.

- Jarvi-10 polygons for lakes, River-10 polygons for rivers

In case waterbodies have islands such as Pannujärvi and Pääjärvi, the negative buffer is essentially applied "away" from the island leaving an empty area around it. It is also to be noted that since the river portions are originally a single large area, they have been manually limited to a length of around 1 000 meters for each.

Figure 42 *An example of a negative buffer of 50m shown in light blue line and original jarvi-10 area in red, applied for lake Suolijärvi. A vast majority of shoreline vegetation has been removed from the internal buffered area except for the south-eastern end of the lake. Base map view using Google Earth.*

3.3.2 Pre-processing Sentinel-1 data

Several types of data are required to create suitable terrain corrected rasters for later processing. DEM, subset polygon and mask preparation is done in GIS, and Sentinel-1 GRD dataset processing in ESA SNAP version 5.0 and S1TBX.

- GRD-datasets and their corresponding precise orbits
- Geoid-corrected 10-m DEM
- Buffered Jarvi-10 polygons
- List of waterbody-ID's or other identifiers of waterbodies being studied

Sentinel-1 datasets were acquired from the Copernicus Open Access portal. The service allows the user to search and download datasets by a selected area, dates and relative orbits. All datasets since the availability of datasets after the data first became available in late 2014 and until April 24th of 2018 were downloaded for the specified relative orbits for the study areas. As GRD-datasets have been split along the acquisition direction to smaller portions from the full flyover acquisition, two datasets split through the study area were acquired and merged using ESA SNAP S1TBX Slice Assembly functionality.

Sentinel-1 GRD datasets are processed individually using ESA SNAP graph builder and batch processing but saved to the same location for the same relative orbit. As the first step, a subset is applied to the radar image to significantly reduce time required for later processing steps. An orbit file is applied to the dataset, making later terrain correction more accurate. Thermal noise is removed from the data using included noise vectors, and data is calibrated to sigma-zero equivalent intensity for an ellipsoid. The radar images are calibrated to sigma0.

A boxcar speckle filter is applied with a window size of 3 × 3 to the radar image. As the pixel spacing in GRD-data is 10 × 10 meters, this equals a window size of 30 × 30 m. For next steps, original GRD 10 × 10 pixel spacing is preserved though the resolution is reduced due to the filtering. Next, terrain correction is applied using the ellipsoid-corrected DEM calculated earlier in this section, using bilinear interpolation for determining values between the radar image and the DEM. The terrain corrected raster projected into ETRS-TM35FIN coordinate reference system with an approximate pixel spacing of 10 × 10 meters.

Applying the second subset, all rasters are subsetted using the same border coordinates. The second subsampling step is important to be done prior to resampling in order to ensure the resampled pixels are properly overlaid within an acceptable range of ± 5 meters in latitude and longitude when comparing to other rasters and land masking can be done at a suitably high resolution (Fig. 43). If resampling is applied to data with varying border coordinates, this would result in the lower resolution resampled raster also varying by pixel location – meaning the rasters would be not properly overlaid in the later steps converting raster values into matrices.

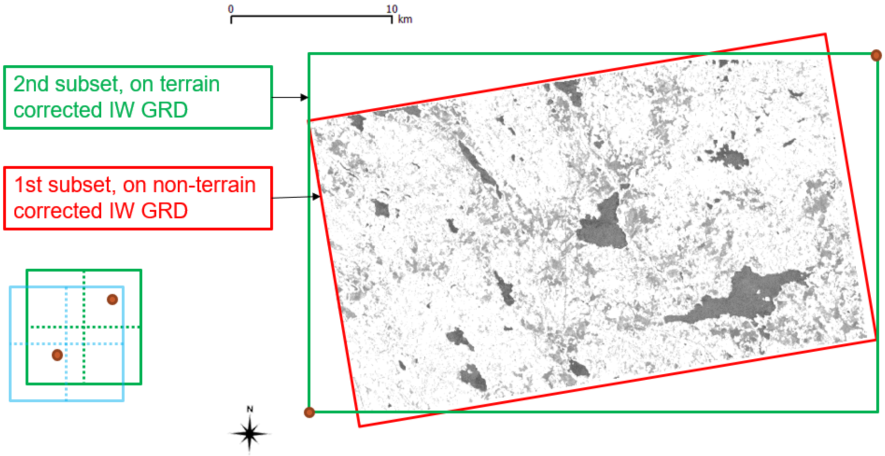

Figure 43 *Resampling steps visualized for the lake study area. The first subset area is skewed due to the subsetting being applied prior to terrain correction.*

Another important step prior to waterbody area resampling is land masking. Masking is applied by determining whether a pixel centre is within the specified Jarvi-10 areas, where the suitable areas can be selected using a list of waterbody-ID's being analysed. As the resampled pixel value in the 50 × 50 m pixel spacing (30 × 30 m for rivers) equals to the mean of underlying speckle filtered pixels, including high-backscattering shorelines, land, exposed rocks or even thick shoreline vegetation, would greatly increase the backscattering strength of the respective resampled pixel. As these partly non-water areas over summertime very likely to feature a different backscattering strength as compared to other seasons, raster comparisons without land masking would indicate differences between the seasons instead of the actual water.

After masking, resampling is applied to the data, resulting in lower pixel-spacing rasters (Fig. 44). As a final step prior to saving the data in a geotiff format for further steps is converting the intensity values of each pixel to decibels. The pre-processed Sentinel-1 dataset output is indicated as a "VV-polarity sigma0"-raster in later use.

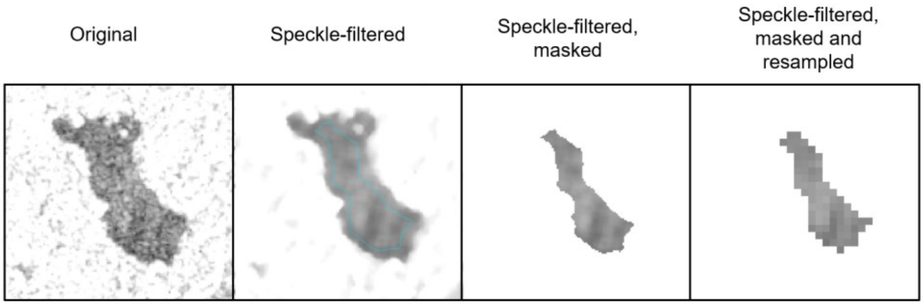

Figure 44 *Radar image speckle filtering, masking and resampling visualized for lake Pannujärvi. Darker values indicate lower backscattering coefficient.*

For output, geotiff format is used for individually storing the VV-polarity sigma0 rasters. The complete processing chart for Sentinel-1 pre-processing presented in this section can be found in figure 45.

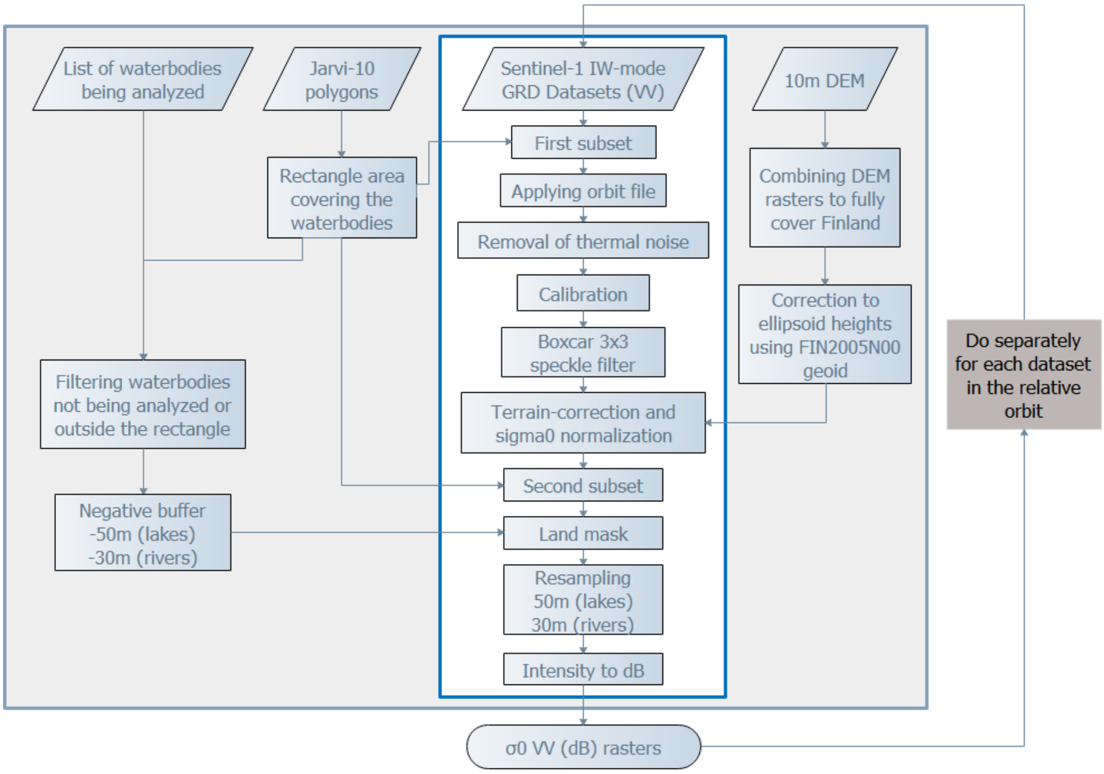

Figure 45 *Processing waterbody shape masks, subsetting areas, DEM's and pre-processing Sentinel-1 GRD datasets.*

3.3.3 In-situ weather data

Using the epoch date-times for each Sentinel-1 flyover, the below three types of values from FMI weather observation stations are acquired prior to processing this data to rasters for later steps. The observations for each measurement location are categorized by the flyover and converted to shapefile format.

- Wind speed, wind gust speed, wind direction measurements from all available FMI stations in Finland during the satellite flyover, including a timestamp and station location

Inverse distance weighted interpolation is used to form an approximation of the wind field in between the observations. The interpolation is applied individually to wind speed, gust speed and wind direction. Though not the most accurate method of interpolation for wind, it has been found in that inverse distance weighted interpolation is a relatively accurate approximation of the wind field (Palomino & Martin 1994).

The following equation is used for inverse distance interpolation.

$$z_j = \frac{\sum_{i=1}^{N} {d_{ij}}^{-a} z_i}{\sum_{i=1}^{N} {d_{ij}}^{-a}} \tag{4}$$

Where z_j is the estimated value at grid location j and z_i is the known control point location value. d_{ij} denotes the distance between the grid location j and the control point location i. Value a is the exponent of the interpolation (Armstrong & Marciano 1994).

For the calculations of the interpolated rasters, calculations for angle sine and cosine components, gust speed and wind speed were applied separately with the same parameters. At a pixel spacing of 1 km, value of exponent a was set to 2 and selection of the points used in each raster pixel interpolated was determined by a maximum search radius of 150 km and using 10 closest points. The output raster covers the entire Finland and uses the ETRS-TM35FIN coordinate reference system.

To calculate the angle from the sine and cosine components, a raster calculation using atan2 with interpolated rasters of sine and cosine was applied. This results in wind angle being converted back to degrees from the two components used in interpolation.

$$atan2(y, \mathrm{x}) = \frac{2y}{\sqrt{x^2+y^2+x}} \tag{5}$$

Where y is the sine component of wind direction and x the cosine component of wind direction.

The result from processing all observations categorized by the epoch date-time are three rasters for each flyover that indicate approximate windspeeds above the waterbodies. The complete process above is visualized below – as an example showing how nearby measurements affect interpolated values more than far-away values.

3.3.4 Accumulating degree-day calculations

Temperature observations via accumulating degree-days, TDD and FDD, are compared in the results chapter against ice phenology dates determined using the method described in later parts of this section. As some waterbodies do not have freeze-up and break-up date observations, one can compare the dates since autumn 2014 to the occurring temperatures.

- Daily air temperature observations from closest FMI weather station (“Hämeenlinna Lammi Pappila” for lake study area, “Pori Rautatieasema” for river study area)

The starting dates for the accumulations have been selected to be the same as in the lake ice phenology report by J. Korhonen (2005), with FDD being the sum of negative average temperatures over autumn starting from the September 15th and TDD the sum of positive average temperatures since the 1st of February. The average temperature of the specific date the FDD and TDD is calculated for is included in the accumulated sum.

3.4 Calculating lake phenology from pre-processed data

3.4.1 Wind raster to a similarity matrix for each waterbody

In this section a wind similarity matrix is determined for each waterbody. The following data is used.

- Interpolated wind speed, gust speed and wind direction rasters from section 3.3.3
- Jarvi10 areas (study lakes) and portions of Kokemäenjoki

As the interpolated wind surfaces are relatively coarse in estimating the wind field above waterbodies and the sizes of the waterbodies in study areas being relatively small, it is seen that there are no significant benefits from using the entire wind rasters covering the whole lake to estimate their similarity. Therefore, the polygon centroid serves as a single point while the nearest neighbouring pixel provides the value used for wind speed, gust speed and wind direction. For comparing wind similarity, a single unitless value is calculated between two compared wind conditions with the following formula.

$$\Delta v_{ab} = \frac{|v_{GUST,b} - v_{GUST,a}|}{3} + \frac{|v_{WIND,b} - v_{WIND,a}|}{3} + \frac{\Delta\theta_{a,b}}{90} \tag{6}$$

Where v_{GUST} values are gust speeds in m/s, v_{WIND} wind speed in m/s for the corresponding two wind conditions. $\Delta\theta_{a,b}$ is the positive angle difference in degrees (always between 0-180°). These are visualized in Fig. 46.

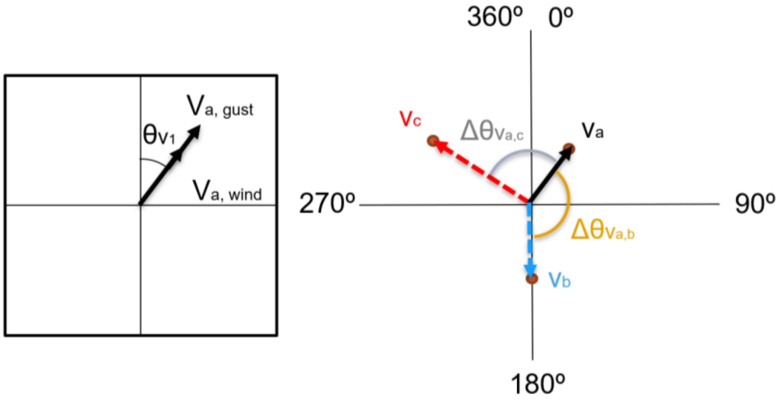

Figure 46 *Left: wind direction, gust, windspeed components; right: wind similarity angle difference*

This value is then calculated for each scene being analysed forming a matrix, with columns and rows both equalling to N.

$$W = \begin{bmatrix} \Delta v_{aa} & \Delta v_{ab} & \dots & \Delta v_{aN} \\ \Delta v_{ba} & \Delta v_{bb} & \dots & \Delta v_{bN} \\ \dots & \dots & \dots & \dots \\ \Delta v_{Na} & \Delta v_{Nb} & \dots & \Delta v_{NN} \end{bmatrix} \tag{7}$$

The ordering of values in matrices W found in Eq. (7) should be determined in a fashion that is identical to matrices D from Eq. (10) in the section 3.4.2, or matching epoch timestamps from vector E from Eq. (19).

Only in case where the two wind conditions are completely identical, Eq. (6) will obtain a value of zero. More similar conditions indicate smaller values and less similar conditions higher values. Least similar conditions give a value of around 10 when comparing opposite direction wind conditions of no-wind to 10 m/s wind, 12 m/s gusts.

When comparing calculated values for relative orbit 160 for lake Pannujärvi, the values vary between two most similar wind conditions reaching a value 0.08 and two least similar ones reaching a value of roughly 8. On average similarity between the radar images is around 2.5, with 95% of the values being above 0.15 and 95% of the values below 7. A higher average difference for all comparisons of a single wind condition mean it is less likely to occur in the area – however for all scenes the most similar scene can be found below a value of 1.

3.4.2 Converting VV-polarity sigma0 rasters to similarity matrices

In this section, two matrices are calculated that both indicate similarities of two Sentinel-1 datasets covering a single waterbody. Following data is used from section 3.4.3.

- Sentinel-1 scenes, using “VV-polarity sigma0” raster values, dB

Let us name two Sentinel-1 rasters from the same relative orbit as “a” and “b”. Two matrices are formed from two compared Sentinel-1 rasters, with each matrix value corresponding to the VV-polarity sigma0 (dB) by same row and column as the raster. Both matrices have the same number of columns (n) and rows (m) and start from the first pixel of the uppermost left corner, as the Sentinel-1 datasets have been processed for each waterbody to feature same raster dimensions (Fig. 47). Pixels including no data are not taken into accord in later calculations and should be indicated as no-data values in the matrices.

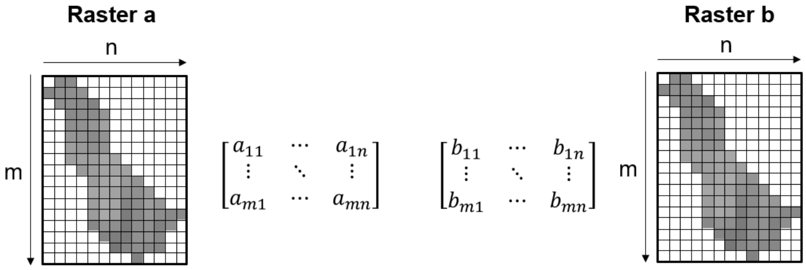

Figure 47 *Matrix formation from raster values.*

Two values are calculated to compare the two rasters - an averaged pixel difference d_{ab} between the two rasters and a Pearson correlation coefficient r_{ab}. Starting from the pixel difference, a matrix is formed with each pixel values indicating an absolute value

$$M_{diff,ab} = \begin{bmatrix} |a_{11} - b_{11}| & \cdots & |a_{1n} - b_{1n}| \\ \vdots & \ddots & \vdots \\ |a_{m1} - b_{m1}| & \cdots & |a_{mn} - b_{mn}| \end{bmatrix} \tag{8}$$

Where values of a and b correspond with Fig. 47. These values are converted to a single unitless average of all matrix $M_{diff,ab}$ values

$$d_{ab} = \frac{\sum_{i=1}^{m}\sum_{j=1}^{n}|a_{ij}-b_{ij}|}{mn} \tag{9}$$

Now, when comparing several rasters, a matrix with difference values *d* in their respective row and column is formed. The number of columns and rows in the matrix is the same and is determined by the amount of rasters (denoted by N) to compare.

$$D = \begin{bmatrix} d_{aa} & d_{ab} & \dots & d_{aN} \\ d_{ba} & d_{bb} & \dots & d_{bN} \\ \dots & \dots & \dots & \dots \\ d_{Na} & d_{Nb} & \dots & d_{NN} \end{bmatrix} \tag{10}$$

Each value in the matrix is then normalized. Mean and standard deviation values are calculated for preparation for the whole matrix.

$$\mu_D = \frac{\sum_{i=1}^{N}\sum_{j=1}^{N} d_{ij}}{N^2} \tag{11}$$

$$\sigma_D = \sqrt{\frac{\sum_{i=1}^{N}\sum_{j=1}^{N}\left(d_{ij}-\mu_D\right)^2}{N^2-1}} \tag{12}$$

By using the above values a following equation for normalization is used.

$$n\left(d_{ij}\right) = \frac{d_{ij}-(\mu_D-2\sigma_D)}{(\mu_D+2\sigma_D)-(\mu_D-2\sigma_D)} \tag{13}$$

The normalization is then applied for each value of the matrix.

$$D_{norm} = \begin{bmatrix} n(d_{aa}) & n(d_{ab}) & \dots & n(d_{aN}) \\ n(d_{ba}) & n(d_{bb}) & \dots & n(d_{bN}) \\ \dots & \dots & \dots & \dots \\ n(d_{Na}) & n(d_{Nb}) & \dots & n(d_{NN}) \end{bmatrix} \tag{14}$$

To calculate Pearson correlation coefficient r_{ab}, the following equation is used pairwise for each corresponding pixel between two rasters

$$r_{ab} = \frac{\sum_{i=1}^{n}\sum_{j=1}^{m}(a_{ij}-\bar{a})(b_{ij}-\bar{b})}{\sqrt{\sum_{i=1}^{n}\sum_{j=1}^{m}(a_i-\bar{a})^2}\sqrt{\sum_{i=1}^{n}\sum_{j=1}^{m}(b_i-\bar{b})^2}} \tag{15}$$

The correlation is calculated pairwise between each compared raster. The number of columns and rows in the matrix yet again is the same and is determined by the amount of rasters in total to compare.

$$R = \begin{bmatrix} r_{aa} & r_{ab} & \dots & r_{aN} \\ r_{ba} & r_{bb} & \dots & r_{bN} \\ \dots & \dots & \dots & \dots \\ r_{Na} & r_{Nb} & \dots & r_{NN} \end{bmatrix} \tag{16}$$

The correlation values are also normalized using Eq. (13) where μ_D is replaced by μ_R and σ_D by σ_R from Eq. (11) and Eq. (12) applied to matrix R.

$$n\left(r_{ij}\right) = \frac{r_{ij}-(\mu_R-2\sigma_R)}{(\mu_R+2\sigma_R)-(\mu_R-2\sigma_R)} \tag{17}$$

Resulting in a normalized correlation matrix.

$$R_{norm} = \begin{bmatrix} n(r_{aa}) & n(r_{ab}) & \dots & n(r_{aN}) \\ n(r_{ba}) & n(r_{bb}) & \dots & n(r_{bN}) \\ \dots & \dots & \dots & \dots \\ n(r_{Na}) & n(r_{Nb}) & \dots & n(r_{NN}) \end{bmatrix} \tag{18}$$

As normalization is applied for the separate orbits for both matrices, it will reduce the differences due to varying incidence angle to the values.

3.4.3 Calculating similarity value in comparison to open water

The single wind difference matrix calculated section 3.4.1 and the raster difference and correlation matrix from section 3.4.2 are used to determine ice-phenology events.

- Difference matrix for Sentinel-1 dataset wind conditions, W
- Correlation matrix between Sentinel-1 datasets, R_{norm}
- Averaged raster difference matrix between Sentinel-1 datasets, D_{norm}

To start the analysis, two vectors are formed. First one contains the epoch in seconds for each column indicating the date-time of the acquisition of Sentinel-1 data. The second the acquisition month of each column, M. The wind difference matrix W and the two matrices calculated from Sentinel-1 rasters should correspond to the same date-times.

$$E = [a_{epoch} \quad \cdots \quad N_{epoch}] \tag{19}$$

$$M = [a_{month} \quad \cdots \quad N_{month}] \tag{20}$$

For matching the months for rows, one can simply transpose matrix M.

$$M^T = \begin{bmatrix} a_{month} \\ b_{month} \\ \cdots \\ N_{month} \end{bmatrix} \tag{21}$$

For southern Finland, summer months with no ice can be beginning of June (the 6th month) up to October (the 10th month). Now, creating a new matrix from $M^T$with summer months indicated by 1 and winter months as 0.

$$M_{summer}^T = \begin{bmatrix} a_{summer} \\ b_{summer} \\ \cdots \\ N_{summer} \end{bmatrix} \tag{22}$$

Where values $a_{summer} \dots N_{summer}$ are determined using Eq. (23) and Eq. (24).

$$a_{summer} \dots N_{summer} = 0, if \begin{cases} a_{month} \dots N_{summer} < 6 \\ \quad or \\ a_{month} \dots N_{summer} > 10 \end{cases} \tag{23}$$

$$a_{summer} \dots N_{summer} = 1, if\ 6 \leq a_{month} \dots N_{summer} \leq 10 \tag{24}$$

Using the matrix M_{summer}^T, each value of a row of the wind difference matrix W from Eq. (7) are set to zero if the corresponding value of M_{summer}^T is zero. This essentially filters out wind comparisons between two winter scenes but leaves the comparisons between winters and summers and vice versa. Summer-summer comparisons also remain.

$$\begin{array}{cccccc} & & & & & \text{Rows} \\ & a_{summer}\Delta v_{aa} & a_{summer}\Delta v_{ab} & \cdots & a_{summer}\Delta v_{aN} & r_a = 0 \\ W_{summer} = & b_{summer}\Delta v_{ba} & b_{summer}\Delta v_{bb} & \cdots & b_{summer}\Delta v_{bN} & r_b = 1 \\ & \cdots & \cdots & \cdots & \cdots & \cdots \\ & N_{summer}\Delta v_{Na} & N_{summer}\Delta v_{Nb} & \cdots & N_{summer}\Delta v_{NN} & r_N = N \\ \text{Columns} & c_a = 0 & c_b = 1 & & c_N = N & \end{array} \tag{25}$$

Next, five smallest values for each column are listed for each column c and their row and column are determined using Eq. (25). Let's determine these values to be in rows numbered $r_a \dots r_e$ where r_a contains the smallest value found in column c_a throughout to value c_e being the fifth smallest value of the column.

If any of the above five smallest W_{summer} values exceed the wind filtering threshold, in this thesis a value of 1.0, they are excluded from the latter Eq. (26) and Eq. (27). If all values in a single column exceed the threshold, the column is excluded from later steps.

The corresponding rows and columns above are used to determine raster difference and correlation values from matrices R_{norm} and D_{norm}. In this case, they would equal to $R_{norm}(r_a, c_a) \dots R_{norm}(r_e, c_a)$ and $D_{norm}(r_a, c_a) \dots D_{norm}(r_e, c_a)$.

The average of these R values and D values is determined using a following equations

$$d_A = \frac{D_{norm}(r_a,c_a)+D_{norm}(r_b,c_a)+D_{norm}(r_c,c_a)+D_{norm}(r_d,c_a)+D_{norm}(r_e,c_a)}{n(D_{norm}(r_a,c_a)\dots D_{norm}(r_e,c_a))} \tag{26}$$

$$r_A = \frac{R_{norm}(r_a,c_a)+R_{norm}(r_b,c_a)+R_{norm}(r_c,c_a)+R_{norm}(r_d,c_a)+R_{norm}(r_e,c_a)}{n(R_{norm}(r_a,c_a)\dots R_{norm}(r_e,c_a))} \tag{27}$$

The above two values can be considered the most similar scenes regarding the wind conditions of the single column. As each column corresponds to a single Sentinel-1 dataset, both scenes during winter and summer are compared to the five most similar scenes.

Another set of averages is calculated by choosing corresponding correlation and raster difference values between the similar wind scenes themselves, by forming two matrices.

$$D_B = \begin{bmatrix} NA & D_{norm}(r_a, c_b) & D_{norm}(r_a, c_c) & D_{norm}(r_a, c_d) & D_{norm}(r_a, c_e) \\ NA & NA & D_{norm}(r_b, c_c) & D_{norm}(r_b, c_d) & D_{norm}(r_b, c_e) \\ NA & NA & NA & D_{norm}(r_c, c_d) & D_{norm}(r_c, c_e) \\ NA & NA & NA & NA & D_{norm}(r_d, c_e) \\ NA & NA & NA & NA & NA \end{bmatrix} \tag{28}$$

$$R_B = \begin{bmatrix} NA & R_{norm}(r_a, c_b) & R_{norm}(r_a, c_c) & R_{norm}(r_a, c_d) & R_{norm}(r_a, c_e) \\ NA & NA & R_{norm}(r_b, c_c) & R_{norm}(r_b, c_d) & R_{norm}(r_b, c_e) \\ NA & NA & NA & R_{norm}(r_c, c_d) & R_{norm}(r_c, c_e) \\ NA & NA & NA & NA & R_{norm}(r_d, c_e) \\ NA & NA & NA & NA & NA \end{bmatrix} \tag{29}$$

A threshold of >1.0 is used corresponding to W_{summer} wind difference values for each value in matrices R_B and D_B, and these are excluded from later steps. If all values in above matrices are filtered, here the corresponding column c_a is to be excluded from later calculations. Finally, the average of all non-excluded or NA values of the matrix D_B are calculated as d_B and matrix R_B as r_B.

Next, the difference between the two points is calculated. This can be considered the length or distance between points (r_A, d_A) and (r_B, d_B).

$$l = \sqrt{(r_A - r_B)^2 + (d_A - d_B)^2} \tag{30}$$

By applying Eq. (30) following steps from the start of section 3.4.3, beginning from the first column and ending at the last column of matrices W, R_{norm} and D_{norm} for a single relative orbit's radar images, a new matrix with difference values l can be formed.

$$L = [l_a \quad \dots \quad l_N] \tag{31}$$

The values can be compared to the flyover dates of the matrix E containing the epochs. In case more than a single relative orbit is used for calculations, one can combine the observations by joining the matrices, then sorting the data according to the epoch date-time which increases over time. Though there are no technical limitations for the number of relative orbits to be used, single areas in southern Finland around the study areas typically have around 4 relative orbits with enough observations.

For the next step, following combined and ordered matrices are used with the first dataset being "a" and last R.

$$L_{all} = [l_a \quad \dots \quad l_R] \tag{32}$$

$$M_{all} = [m_a \quad \dots \quad m_R] \tag{33}$$

$$E_{all} = [e_a \quad \dots \quad e_R] \tag{34}$$

As the filtering from previous steps results in some of the columns being neglected from latter steps, these columns are removed in matrix L_{all}. Therefore, R is not direct addition of the combined relative orbits.

3.4.4 Using similarity values to determine ice phenology dates

For data presented in more detail in the results chapter indicates it is difficult to distinguish between a freezing date and a freeze-up date – or break-up dates and clear of ice dates. Therefore, instead of dates, freeze-up period and break-up period are used, during both of which all relevant changes to the waterbody ice cover are likely to occur.

Ice phenology events are determined using the similarity values for each Sentinel-1 epoch, using the three single-row matrices. Three different methods are presented in this section.

- The difference values L_{all}
- Corresponding epoch date-times for each difference value in epoch E_{all}
- Month of the Sentinel-1 date-times M_{all}

A method to determine ice phenology based on noisy data was presented in the study of J. Du. (2017) by applying a temporal filter to the data to reduce the possibilities of misclassifications due to outliers, then determining the waterbody to be either water dominant or ice dominant by a suitable threshold for each average-filtered value.

First a threshold is calculated using the averages for summer and winter l values. An average for summer, $l_{mean,summer}$, is calculated for values corresponding values of one in M_{all} that are June – November, meaning matrix M_{all} values equal to months 6-10. However, winter months are determined to be January, February and March of which it is highly likely waterbodies are frozen in southern Finland, meaning M_{all} values equal to months 1-3. The average for winters, $l_{mean,winter}$ is determined from these values.

A middle threshold is an average of the summer and winter means is calculated with Eq. (35).

$$l_{middle} = \frac{l_{mean,winter} + l_{mean,summer}}{2} \tag{35}$$

Since the difference values and thresholds are using the same, they can be visualized together by setting horizontal axis as the time, or epoch, and vertical axis as the difference value (Fig. 48).

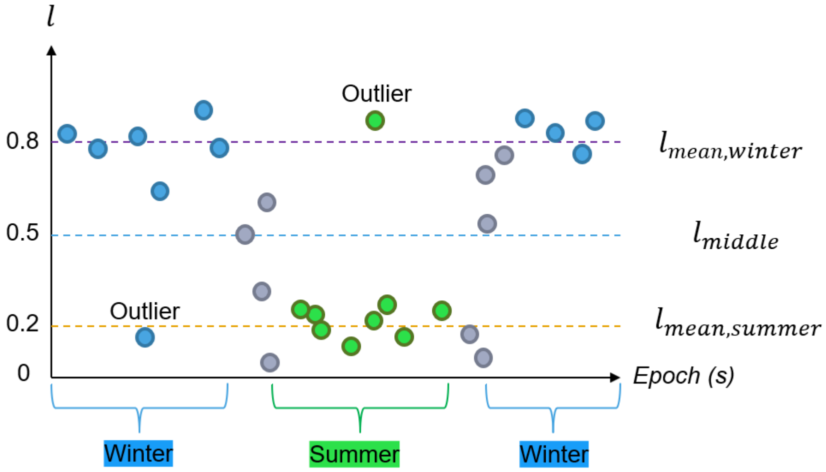

Figure 48 *Visualization of the thresholds (dotted lines) and calculated difference values l for each flyover (points). Grey points are values that cannot be assumed to be either frozen or open water.*

A temporal median filter is applied to suppress high peaks and outliers in the data. A temporal window with a total length of n, results in n_1 equal amount of days backwards in timeline and n_2 forwards in timeline. To determine a smoothed $L_{all,i}$, each l value of L_{all} becomes the smoothed value l_i which is an average of values within a range of $[\, l - \frac{n_1}{2} \,, l + \frac{n_2}{2}\,]$, where $n_1 = n_2 = n$. A temporal window size n of 20 days is used for lakes and 30 days for rivers.

Given corresponding day i starting from zero for the first l_i value, waterbody ice conditions can be determined for each value of l_i where $\frac{n_1}{2} \leq i < \frac{n_2}{2}$. This means that values not fulfilling the full window of the average filter are left out from the following ice detection. The ice phenology for each radar image's l_i value is then determined using the following equation.

$$\begin{aligned} &\text{Waterbody is ice dominant if } l_i \geq l_{middle} \\ &\text{Waterbody is water dominant if } l_i < l_{middle} \,, \end{aligned} \tag{36}$$

The freeze-up periods and break-up periods are determined when temporally adjacent points l_i have a different ice status. Both the duration and date-time of the freeze-up and break-up periods can be determined by using corresponding matrix E_{all} epoch values from Eq. (34). In the example below (Fig. 49), the red graph represents the average and similar representation of freeze-up and break-up periods as presented in later results chapter.

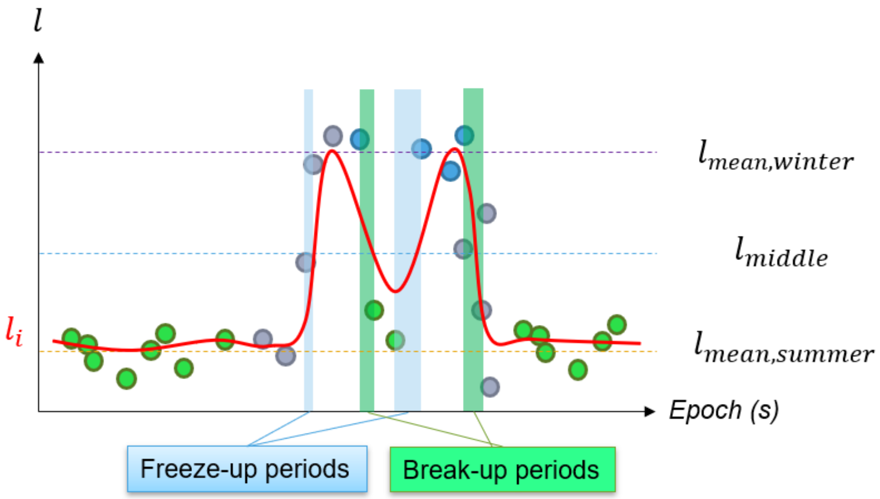

Figure 49 *How ice break-up and freeze-up periods are indicated. Red average graph is not visualized in results.*

4 Results

In this chapter, ice phenology changes calculated for both river study areas and lake areas by the method are compared against available observations and FDD's / TDD's, with the focus being assessment of the accuracy of freeze-up and break-up dates and correct classification during both frozen and open water periods. For simplification, the change between open water to partially frozen or fully frozen is considered the freeze-up period, and final transition between a fully frozen or partially frozen lake to clear of ice the break-up period. This is because the method is unable to reliably distinguish between a partially frozen waterbody and a fully frozen waterbody.

For lakes in the study area, there are most Sentinel-1 acquisitions from relative orbits 51, 58 and 160. Out of these three relative orbits, 51 has significantly more acquisitions than the other two for the river study area so orbit 51 is exclusively used for river portions. The total number of unfiltered datasets for each orbit are given in table 10.

The local incidence angle projected using the corrected DEM for the two river portions is approximately 44°, with relative orbit 51. Similarly, the local incidence angle for study lakes varies between 32° and 45°, depending on the relative orbit, study lake location and the lake's elevation.

Table 10 *Sentinel-1 IW-mode radar images 2014-2018, without wind threshold filtering, used in pre-processing for each waterbody.*

Study area	*Waterbody*	*Datasets from orbit 51*	*Datasets from orbit 58*	*Datasets from orbit 160*
Lake	Pääjärvi	112	75	105
Lake	Suolijärvi	112	75	105
Lake	Pannujärvi	112	75	105
Lake	Lovojärvi	112	75	105
River	Portion A	92	-	-
River	Portion B	92	-	-

4.1 Lake study area

The lake results are presented in order individually for each lake, from largest to smallest. Lake Pääjärvi comparison is based on ice thickness observations and lake Suolijärvi observations have been conducted by Vanajavesikeskus. Lake Pannujärvi observations are based on the reference data station. Lake Lovojärvi has no manual observations, so FDD's and TDD's are used to estimate the sensibility of the results. Lake Pannujärvi observations during winter 2017-2018 were presented in section 3.2.2.

In total 112 radar images from relative orbit 51, 75 images from relative orbit 58 and 105 images from orbit 160 were pre-processed, and the portion of radar images not filtered by the wind similarity threshold 1.0 are shown in table 11 for each lake. Around 50% of the radar images for relative orbits 58 and 160 were collected between June-November, while the same amount is around 40% for relative orbit 51. The relative number of images filtered during each season was around the same.

Table 11 *Percentage of all radar images used for each lake, and relative orbit.*

Lake	*Relative orbit 51*	*Relative orbit 58*	*Relative orbit 160*
Pääjärvi	95%	91%	96%
Suolijärvi	95%	93%	97%
Pannujärvi	95%	95%	97%
Lovojärvi	95%	95%	97%

As relative orbit 58 has less scenes collected as compared to summer, it results overall in less matches for wind conditions seen in table 11. On the other hand, while relative orbits 51 and 160 have around the same amount of radar images, the ratio of summer scenes is higher with relative orbit 160 resulting in a higher matching wind conditions and therefore percentage of the images used in the method. There are minor lake-wise differences, as their interpolated wind conditions have resulted in different wind-threshold filtering of radar images.

4.1.1 Lake Pääjärvi

The buffered polygon for lake Pääjärvi was split to three parts, an “inner area”, “middle area” and “outer area” (Fig. 50), with the outer area featuring the 50-meter buffer but covering only the first 300 meters from the buffer edge. Inner area started at around 600 meters from the 50-meter buffer and covered the innermost area of the lake. The middle area covers the area between the middle and outer areas.

The inner area and middle areas should indicate whether the method is applicable for this specific area presumed to freeze later than the outer area. The method output is compared against ice thickness observations at the western side of lake Pääjärvi (Fig. 50) that do not equal to zero. This means that the ice has been thick enough to stand on and to perform the observation.

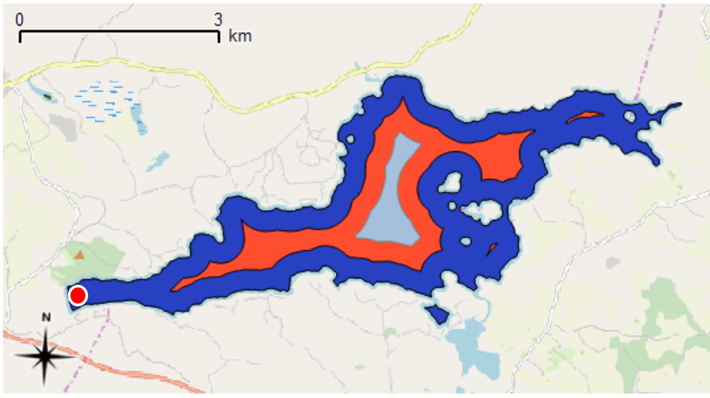

Figure 50 *Lake Pääjärvi mask areas, inner area in light blue, middle area in orange and outer area in dark blue. Red dot at the western side of the lake indicates the location of ice thickness measurements.*

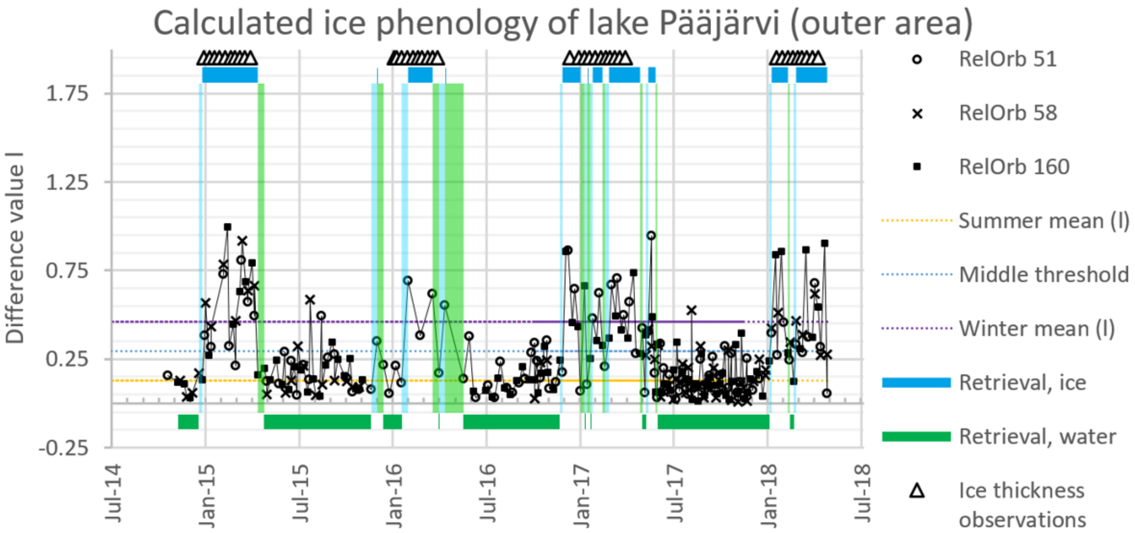

Figure 51 *Lake Pääjärvi outer area difference values from each relative orbit, ice phenology retrievals along with used thresholds, freeze-up and break-up periods and ice thickness observations.*

Table 12 *First and last ice phenology change with FDD's and TDD's for Pääjärvi outer area, in addition to first and last non-zero ice thickness observations for Pääjärvi.*

Winter	*Beginning of freeze-up period*	*End of freeze-up period*	*Freeze-up period FDD (°C d)*	*First non-zero ice thickness observation*
2014-2015	2014-12-20	2014-12-27	-42…88	2014-12-30
2015-2016	2015-12-20	2015-12-03	-4…11	2016-01-05
2016-2017	2016-11-22	2016-11-27	-67…73	2016-12-13
2017-2018	2018-01-04	2018-01-09	-46…56	2018-01-19
Winter	Beginning of break-up period	End of break-up period	Break-up period TDD (°C d)	*Last non-zero ice thickness observation*
2014-2015	2015-04-14	2015-04-26	+95…145	2015-03-30
2015-2016	2016-04-13	2016-05-19	+85…379	2016-03-30
2016-2017	2017-05-27	2017-06-01	+308…356	2017-04-10
2017-2018	-	-	-	-

The first freeze-ups for all winters except for winter 2015-2016 have around the same FDD over the freeze-up period, indicating there could be an offset in the freeze-up of autumn 2015. It would also seem that the ice break-up was determined to be too late for spring 2017, as the TDD is considerable higher than the two other TDD values.

Comparing the first calculated freeze-ups and break-ups with the ice thickness observations, the changes in ice occurred before the ice thickness observations were begun and also after they were ended. This however only indicates that the annual freeze-ups were not determined considerably too late nor break-ups considerably too early.

Except for winter 2014-2015, the frozen water during ice thickness was at several points misclassified as open water. During winter of 2015-2016 the lake has been misclassified as open water for extended periods of time, during which ice thicknesses have been gathered and the lake has had to been at least partially frozen. However, open water during summer was not classified as frozen at any point throughout studied time range.

There is a clear outlier seen on 6.8.2017 at relative orbit 58, 16:00Z. No outliers are visible on the 25.7.2017, 16:00Z, seen in lakes Pannujärvi and Suolijärvi.

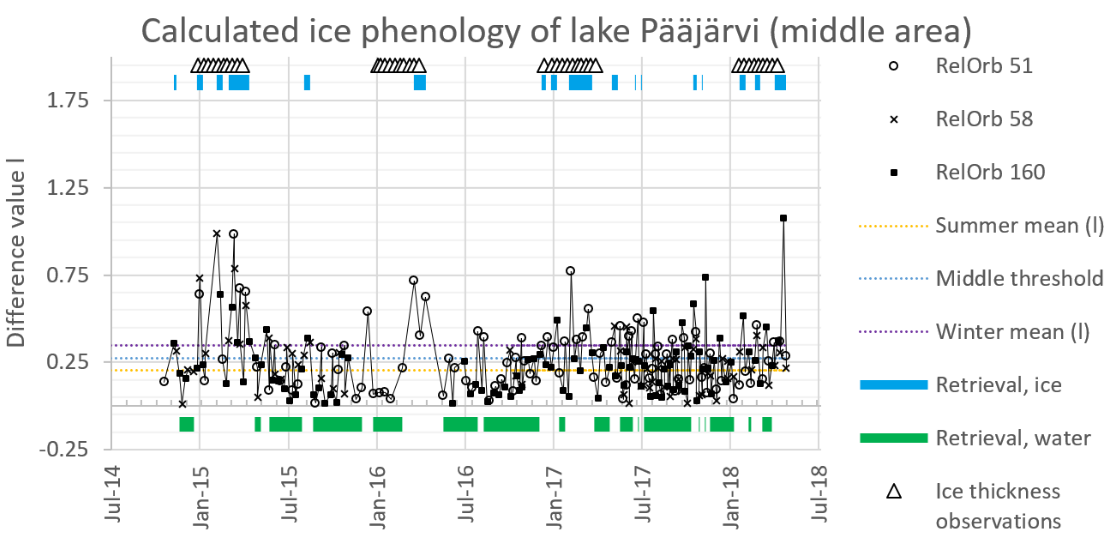

Figure 52 *Lake Pääjärvi middle area difference values from each relative orbit, ice phenology retrievals along with used thresholds and ice thickness observations.*

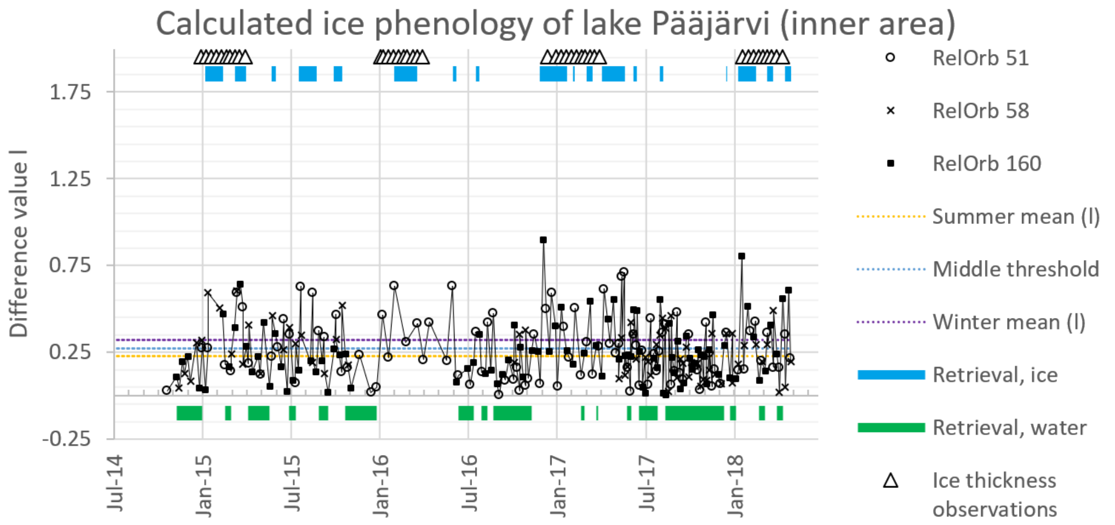

Figure 53 *Lake Pääjärvi inner area difference values from each relative orbit, ice phenology retrievals along with used thresholds and ice thickness observations.*

Both by visual interpretation and by assessing misclassifications of the known frozen period as open water and known open water as ice, the method output quality has higher variance throughout all seasons as compared to the outer area. In addition, the difference between the mean values over known open water during summer and known frozen period of winter is significantly smaller, resulting in misclassifications as the temporal average falls above and below the middle threshold. Both the middle area and inner area feature successful classification as compared to the outer area.

As the quality in results differs considerably between the outer area, and the middle and inner area, this indicates the necessity of inclusion of waterbody areas near the shorelines in the method. Possible reasons are discussed in the discussion chapter.

4.1.2 Lake Suolijärvi

Lake Suolijärvi is surrounded by ridges and agricultural fields to its eastern side and forests and agricultural fields to its western side (Fig. 54). Instead of comparing first manual observations of autumn 2015 and 2017 for the four-day temporary ice, table 13 contains the permanent seasonal ice freeze-up for the years.

As compared to other studied lakes, table 13 also contains two different offsets for comparing the available manual observations between calculated freeze-up and break-up periods. The offset in days indicates how many days the closest of the two period dates differs from the observed date, where positive offset values indicate the period was determined to too late, for negative too early, and nil value meaning the observation date was within the calculated period. With identical distinction between negative, positive and nil values, a radar image offset indicates the offset in radar images instead of days.

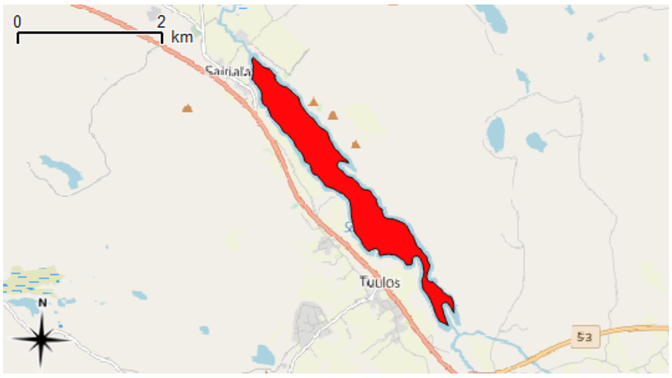

Figure 54 *Lake Suolijärvi area used for selecting radar image pixels.*

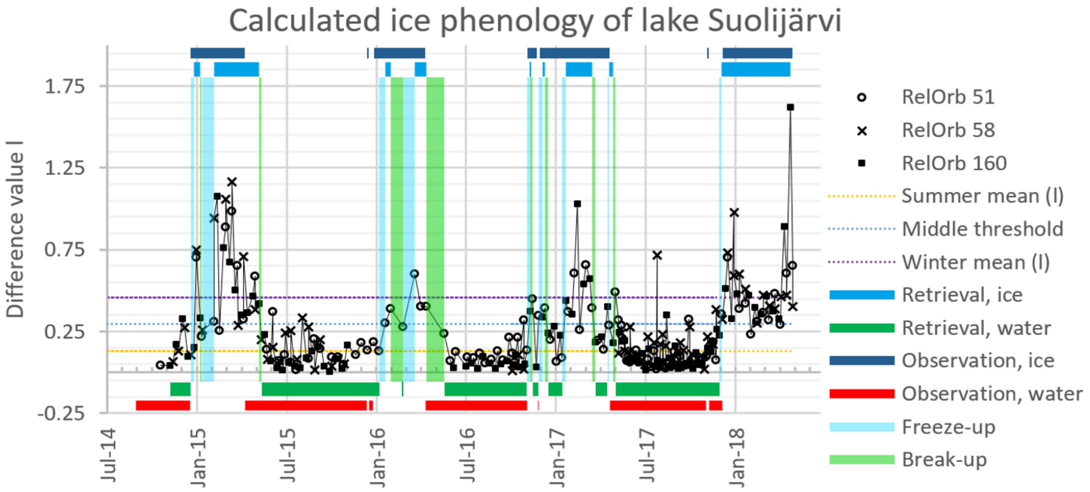

Figure 55 *Lake Suolijärvi difference values from each relative orbit, ice phenology retrievals along with used thresholds and manual observations.*

Table 13 *First calculated freeze-up and break-ups of each year compared to manual observations and FDD's / TDD's for lake Suolijärvi.*

Winter	*Start of freeze-up period*	*End of freeze-up period*	*Freeze-up FDDs (°C d)*	*Manual observation*	*Observation FDD (°C d)*	*Offset in days*	*Radar image offset*
2014-2015	2014-12-20	2014-12-27	-42…88	2014-12-21	-44	0	0
2015-2016	2016-01-08	2016-01-20	-186…270	2015-12-28	-30	+11…23	+4
2016-2017	2016-11-03	2016-11-10	-5…46	2016-11-11	-55	-1…8	-2
2017-2018	2017-11-29	2017-12-04	-16…18	2017-12-06	-22	-2…7	-1
Winter	*Start of break-up period*	*End of break-up period*	*Break-up FDD (°C d)*	*Manual observation*	*Observation FDD (°C d)*	*Offset in days*	*Radar image offset*
2014-2015	2015-05-08	2015-05-13	+239…277	2015-04-11	+88	+27…36	+4
2015-2016	2016-04-13	2016-05-19	+85…379	2016-04-12	+90	+1…36	+1
2016-2017	2017-04-27	2017-05-02	+84…102	2017-04-21	+70	+6…11	+1
2017-2018	-	-	-	-	-	-	-

The FDD's seem to fall within the same range for years except the first freeze-up of winter 2015-2016. Except for year 2015, all observations during freeze-up are consistently estimated too early and observations during spring are estimated too late. Possible explanations for this are presented in the later discussion chapter.

As presumed from the FDD's and TDD's, there are considerable offsets more than ten days in determining the freeze-up of autumn 2015 and the break-up of spring 2015 as compared with the manual observations. Possible reasons for this are discussed in the later chapters.

There are clear outliers seen on 25.7.2017 16:00 UTC at relative orbit 58 and 13.8.2017 16:00 UTC at relative orbit 160. Both are also analysed in discussion chapter in detail.

4.1.3 Lake Pannujärvi

Lake Pannujärvi is mostly surrounded coniferous forest of different densities and heights. It has notably narrowed areas only few 50-meter pixels wide due to an island in the north-eastern side of the lake, also showing how a negative buffer is applied in case there are islands the Jarvi-10 polygons (Fig. 56).

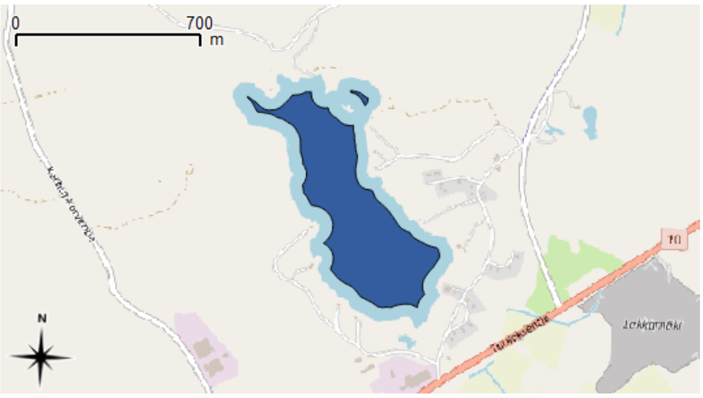

Figure 56 *Lake Pannujärvi area used for selecting radar image pixels.*

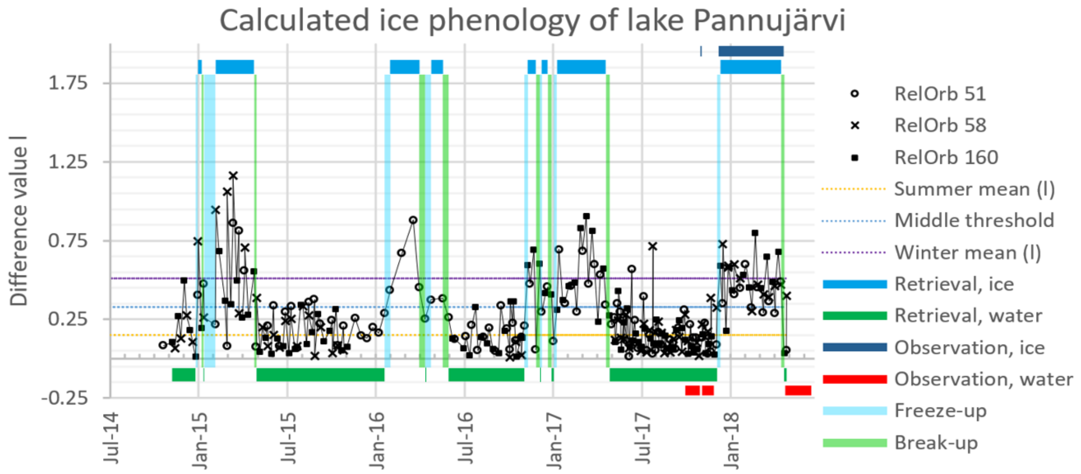

Figure 57 *Lake Pannujärvi difference values, ice phenology and station-observations.*

Table 14 *First calculated freeze-up and break-ups of each year compared to FDD's / TDD's and reference station observations for winter 2017-2018 for lake Pannujärvi.*

Winter	*Beginning of freeze-up period*	*End of freeze-up period*	*Freeze-up period FDD (°C d)*	*Freeze-up observation*
2014-2015	2014-12-27	2015-01-01	-88…122	-
2015-2016	2016-01-20	2016-02-01	-382…440	-
2016-2017	2016-11-03	2016-11-10	-5…46	-
2017-2018	2017-12-04	2017-12-11	-18…27	2017-11-28…12-08
Winter	Beginning of break-up period	End of break-up period	Break-up period TDD (°C d)	Break-up observation
2014-2015	2015-04-26	2015-05-01	+145 … +178	-
2015-2016	2016-05-19	2016-05-31	+379 … +557	-
2016-2017	2017-04-20	2017-04-27	+63 … +80	-
2017-2018	2018-04-15	2018-04-22	+39 … +86	2017-04-21

The lake was observed to freeze between 28.11.2017 – 8.12.2017. The method calculated the freeze-up date to be between these two dates, from 04.12.2017 to 11.12.2017, meaning the calculated freeze-up period was fully within the observation. Similarly, ice break-up was observed to occur on 21.04.2018, with some ice floes on 22.04. and lake being completely ice-free on the 24.04. The method calculated the break-up to occur between the flyovers on the 15th and the 22nd of April, indicating a correct detection of ice break-up period.

The Lake was fully frozen between 1.10.-3.10. with two closest flyovers occurred on 29.10.2017 and 4.11.2017. No ice floes remained after this cycle on the lake on 4.11. This occurrence was not captured in radar images. Similar freeze-up was observed over the early hours of 23.04. promptly resulting in a break-up around midday the same day. Closest satellite flyovers occurred on the 22nd and the 27th, meaning this temporary seasonal ice layer was also not captured in radar images.

As Pannujärvi freeze-up and break-up periods were accurately determined for winter 2017-2018, presuming the periods are also relatively accurate shows a trend of the lake ice breaking up sooner than in previous years as compared to TDD values. One explanation for this is that the oxidization station installed to lake Pannujärvi in 2016, causing a wide melted area, has in fact caused the lake ice to break-up earlier than in previous years.

There is a seemingly a transition in TDD’s between the first two winters and the last two winters. This could be explained by the oxidization station installed into the lake in early 2016 resulting in the lake break-up to occur earlier in comparison to the situation before. A clear outlier is seen on 25.7.2017 at relative orbit 58, 16:00Z, the same as for Suolijärvi.

4.1.4 Lake Lovojärvi

Lake Lovojärvi is smallest of four studied lakes with a surface area of around 5 ha, with an elongated shape similar to that of lake Suolijärvi. Due to its small size in the negative buffer area (Fig. 58), only four pixels with the 50-meter pixel spacing were analysed.

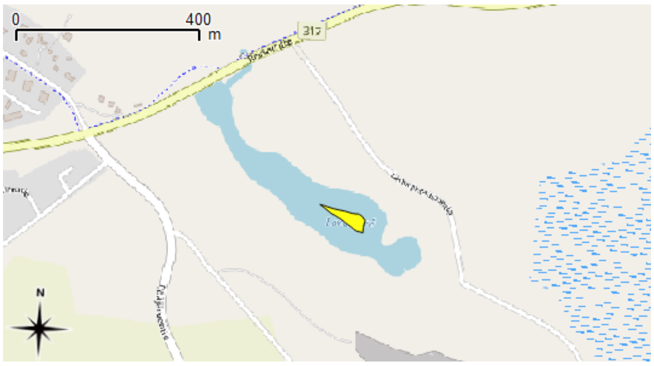

Figure 58 *Lake Lovojärvi area used for selecting radar image pixels*

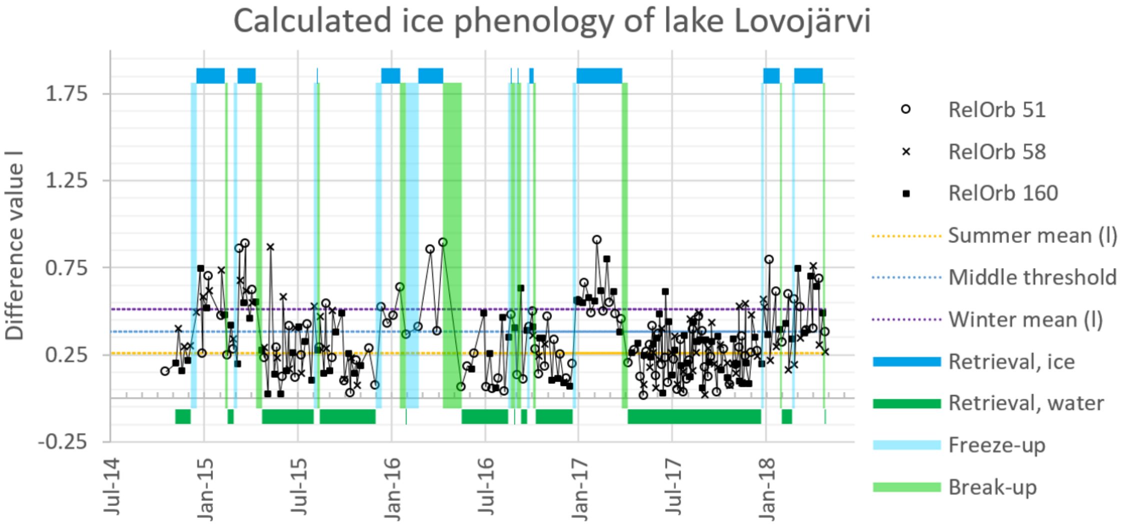

Figure 59 *Lake Lovojärvi difference values from each relative orbit and ice phenology retrievals along with used thresholds.*

Table 15 *First and last ice phenology change with FDD’s and TDD’s for Lovojärvi.*

Winter	*Beginning of freeze-up period*	*End of freeze-up period*	*Freeze-up period FDD (°C d)*
2014-2015	2014-12-08	2014-12-20	-40…42
2015-2016	2015-12-03	2015-12-15	-11…16
2016-2017	2016-12-21	2016-12-28	-168…-171
2017-2018	2017-12-23	2017-12-28	-36…44
Winter	Beginning of break-up period	End of break-up period	Break-up period TDD (°C d)
2014-2015	2015-04-14	2015-04-26	+101…152
2015-2016	2016-04-13	2016-05-19	+104…389
2016-2017	2017-03-27	2017-04-08	+34…51
2017-2018	-	-	-

The variance in the data is considerably higher as compared to lake Pannujärvi or Suolijärvi, and there are misclassifications during mid to late summer over years 2015-2016 when freeze-up was not possible. However, when compared to inner and middle areas of Pääjärvi, the variance in the data is lower and the difference between the mean of summer and mean of winter much larger.

The corresponding FDD's and TDD's fall within reasonable range for winters, except for freeze-up of winter 2016-2017 being considerably higher than during rest of the winters, and break-up during the same year occurring seemingly far earlier as compared to the TDD of the previous years. These periods do most likely have a considerable offset, for freeze-up to be estimated too late and break-up too early.

Both incorrect detections of freeze-up and break-up over the course of summers 2015 and 2016 occur around August. A reasonable explanation for this could be the impact of water vegetation in the lake over the course of this period, though this was not ascertained from optical satellite images or other observation sources.

4.1.5 FDD and TDD comparison for each ice year

Calculated first freeze-up and last break-up dates of each year for all lakes along with selected corresponding FDD and TDD values were compiled to Fig. 60 to analyse trends in the data and overall visualize the results for all four lakes.

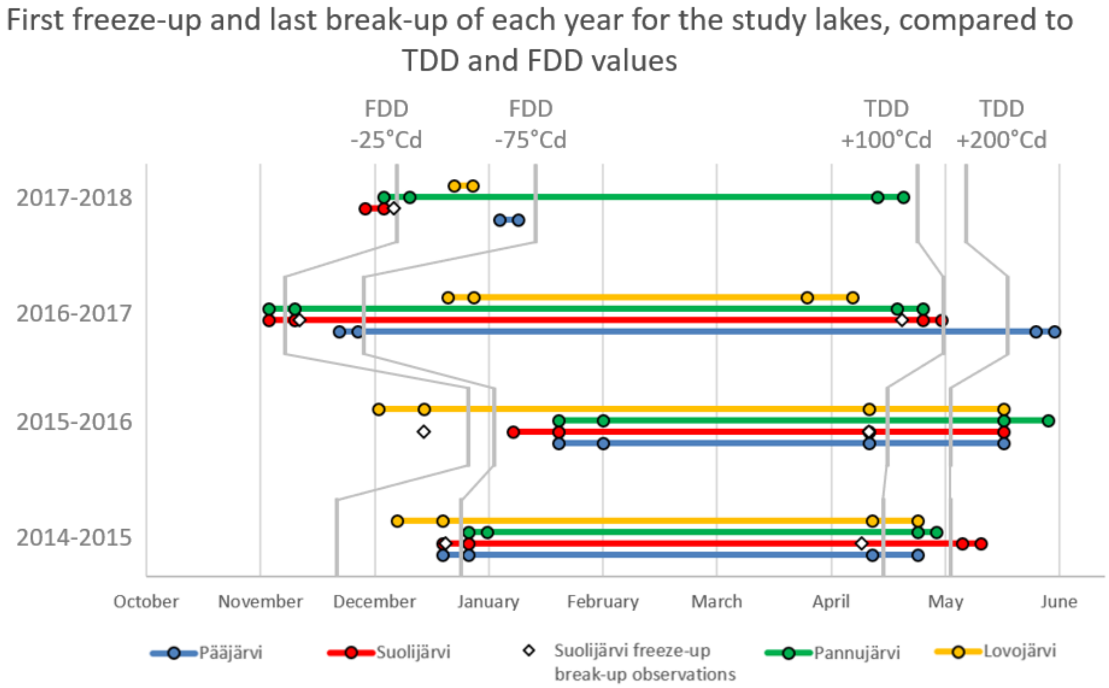

Figure 60 *FDD/TDD values compared with freeze-up and break-up of each lake.*

Lake Lovojärvi should freeze sooner or at the same time as other lakes due to its small area and volume. This is found to be correct for winters 2014-2015 and 2015-2016, but the lake freeze-up is calculated significantly later than in winters 2016-2017 and 2017-2018 indicating these dates are likely inaccurate for lake Lovojärvi. From the other end of the lake sizes, freezing of Pääjärvi as the largest lake should occur later than other lakes. The first freeze-up periods determined by the method shown in Fig. 60 do support this, as the lake is determined to freeze either the last or the second last as compared during all covered four winters.

As Pannujärvi freeze-up and break-up periods were accurately determined for winter 2017-2018, presuming the periods are also relatively accurate shows a trend of the lake ice breaking up sooner than in previous years as compared to TDD values. An explanation for this phenomenon was presented in the section 4.1.3 as being caused by the installation of the oxidization station in 2016. For lake Suolijärvi, the observations marked as inverted white squares in the graph can be seen to match the freeze-up periods and break-up periods calculated by the method relatively well.

Overall, assuming lake Lovojärvi results to have a larger offset in its freeze-up and break-up periods as compared to other lakes, the first freeze-up of lake Suolijärvi, Pannujärvi and Pääjärvi do consistently occur later when FDD values shown in the figure 59 are reached later in the winter, and earlier when the same FDD values occur earlier. For spring, any similar trends in the data cannot be properly assessed due to the long freeze-up period of more than one month during spring of 2016 and the break-up periods not having occurred as of spring 2018 when the method's calculations were processed.

4.2 River study area

The differences to the lake study area for lakes in data pre-processing were a shorter negative buffer of 30 meters instead of 50 meters used for lakes, and a resampled pixel spacing of 30 meters instead of 50 meters. Due to the frequency of radar images being lower than the combined three relative orbits for lakes, a temporal window of 30 days is used instead of the 20-day window for lakes. FDD's / TDD's are used to estimate whether freeze-up and break-up periods for each year were within sensible limits between each year.

Only relative orbit 51 was used, because the number of overlapping acquisitions between the lake study area for which the data was initially acquired is the highest. This also allows for assessing the method when used for a single relative orbit as compared, to multiple relative orbits. From a total of 92 radar images from relative orbit 51, for both portion A and portion B of Kokemäenjoki 9 were not used and the rest were filtered by the wind similarity threshold of 1.0. In total, this equals to 90% of the total scenes used.

The number of scenes used for the lake study area for relative orbit 51 is not equal to the lake study area as both may not be captured within the same radar image as the satellite flyovers are split in GRD processing. Additionally, EW mode acquisitions of Sentinel-1 take up more measurements as from IW mode acquisitions this close to the sea when compared to inland lake study area.

4.2.1 Portion A

River portion A from the buffered JokAlue-10 data (Fig. 61) has a surface area of around 0.10 km^2. The surrounding area is mainly suburban settlement, sparse trees and farmland.

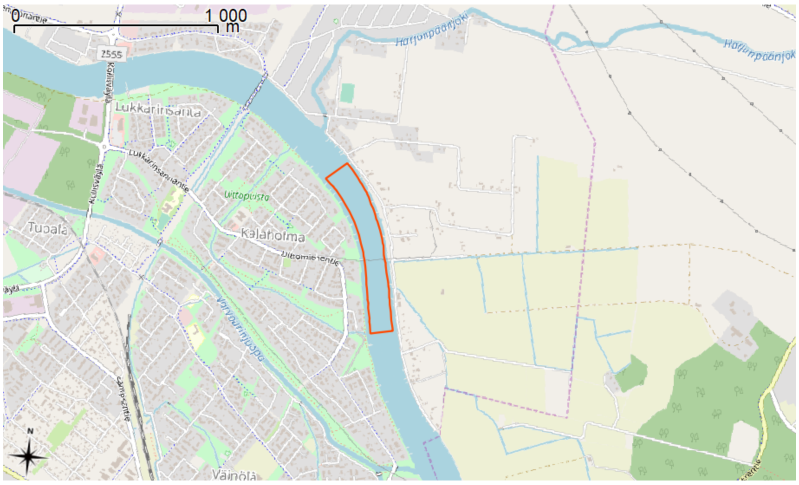

Figure 61 *River Kokemäenjoki portion A area used for selecting radar image pixels.*

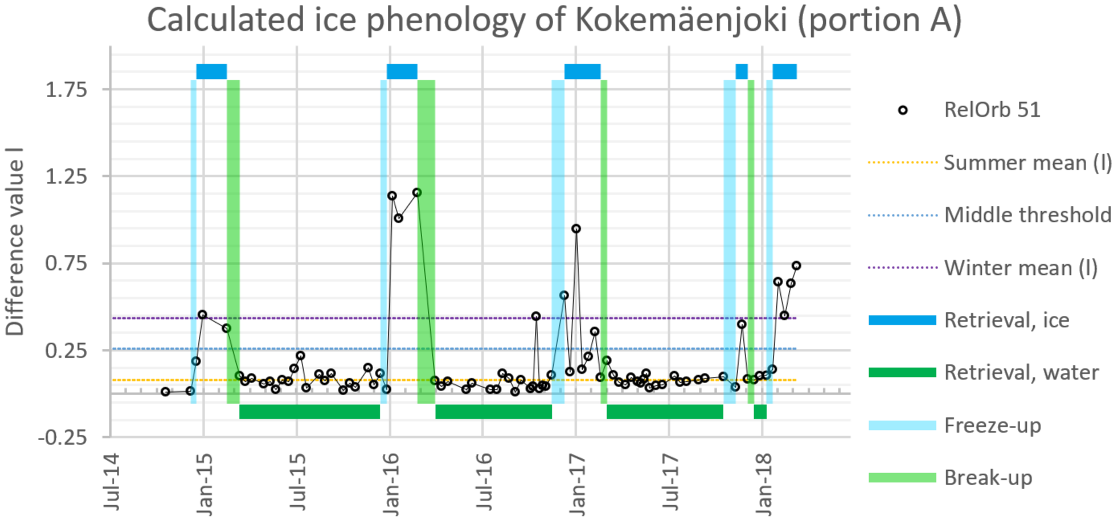

Figure 62 *River Kokemäenjoki portion A difference values from each relative orbit and ice phenology retrievals along with used thresholds.*

Table 16 *First and last ice phenology changes with FDD's and TDD's for portion A.*

Winter	*Beginning of freeze-up period*	*End of freeze-up period*	*Freeze-up period FDD (°C d)*
2014-2015	2014-12-08	2015-12-20	-40…42
2015-2016	2015-12-15	2015-12-27	-16…24
2016-2017	2016-11-15	2016-12-09	-67…124
2017-2018	2017-10-17	2017-11-10	0…-13
Winter	*Beginning of break-up period*	*End of break-up period*	*Break-up period TDD (°C d)*
2014-2015	2015-02-18	2015-03-14	+0…25
2015-2016	2016-02-25	2016-04-01	+0…34
2016-2017	2017-02-19	2017-03-03	+2…31
2017-2018	-	-	-

By visible interpretation of the difference values, the first freeze-up period is seemingly calculated early during winters 2015-2016 and 2017-2018, while break-up is calculated late for winter 2017-2018. This is likely cause by the larger temporal averaging window of 30 days, which means that a large amount of low values over summer will also lower the temporally averaged difference and therefore also causing an offset to the method.

FDD values for freeze-ups do indicate that the freeze-up occurred later in year 2016 and earlier in 2017. Assessing the data in the figure 61, however, shows that it is likely that in year 2016 a temporary freeze-up was missed causing an increased FDD and in year 2017 this was indeed detected causing a decreased FDD. All TDD values seemed to be within the same approximate range, which could indicate that the freeze-up was determined close to correct for these years.

4.2.2 Portion B

River portion B from the buffered JokiAlue-10 data (Fig. 63) has a surface area of around 0.12 km^2. The surrounding area consists of wetland, shoreline vegetation and sparse trees with the Baltic sea on the north-western side.

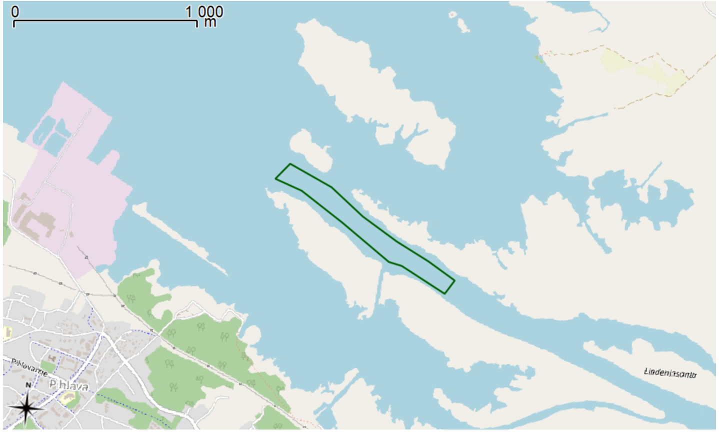

Figure 63 *River Kokemäenjoki portion B area used for selecting radar image pixels. The water area covering majority of the map is the Baltic sea as this is the river's discharge location.*

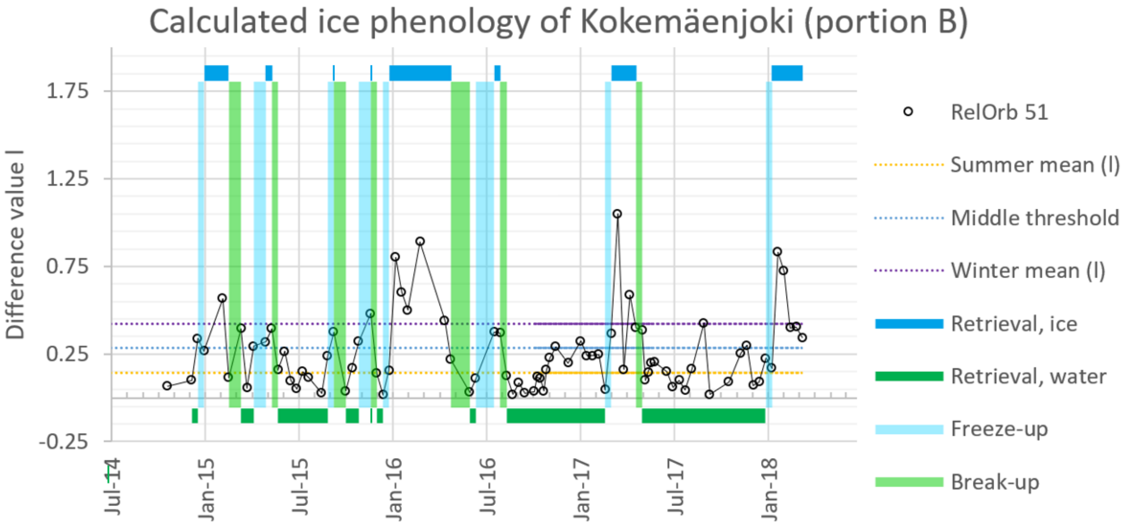

Figure 64 *River Kokemäenjoki portion B difference values from each relative orbit and ice phenology retrievals along with used thresholds.*

Table 17 *First and last ice phenology changes with FDD's and TDD's for portion B.*

Winter	*Beginning of freeze-up period*	*End of freeze-up period*	*Freeze-up period FDD (°C d)*
2014-2015	2014-12-20	2015-01-01	-42…122
2015-2016	2015-10-28	2015-11-21	-3…4
2016-2017	2017-02-19	2017-03-03	-400…440
2017-2018	2017-12-28	2018-01-09	-44…56
Winter	Beginning of break-up period	End of break-up period	Break-up period TDD (°C d)
2014-2015	2015-05-13	2015-05-25	+270…467
2015-2016	2016-04-25	2016-05-31	+128…558
2016-2017	2017-04-20	2017-05-02	+77…143
2017-2018	-	-	-

Portion B featured a higher variance in difference values as compared to portion A results. The likelihood of incorrectly determined freeze-up and break-up periods is considered high, as misclassifications have occurred throughout all seasons such as mid-summer. This is supported by the vastly varying FDD and TDD values for calculated freeze-ups and break-ups of ice. Possible reasons for the differences in the quality of data produced by the method for the two similar portions in size and shape are discussed in the discussion chapter.

5 Discussion

5.1 Outliers in results of studied lakes

In this section, a short analysis is made on outliers detected for the lake study area. One important factor to mention is that due to the implementation of the method the difference values for the same relative orbit do vary as wind speeds and wind directions change. To define outlier values, they could be attributed both significantly lower than expected difference values during frozen waterbody period whereas significantly higher values may be observed during open water period.

An outlier over the summer of 2017 was identified for lakes Pannujärvi and Suolijärvi on 25.7.2017 at approximately 16:00 UTC. By opening the corresponding radar image (Fig. 65), the backscattering from lake Pannujärvi and Suolijärvi seem to be higher than for the lakes in the surrounding area, at around -17dB. Lake Pääjärvi, which also did not feature an outlier for this date, had a backscattering coefficient of around -25dB. In addition, the outlier was not visible in lake Lovojärvi difference values, though the method output data was also noisier than the three other lakes.

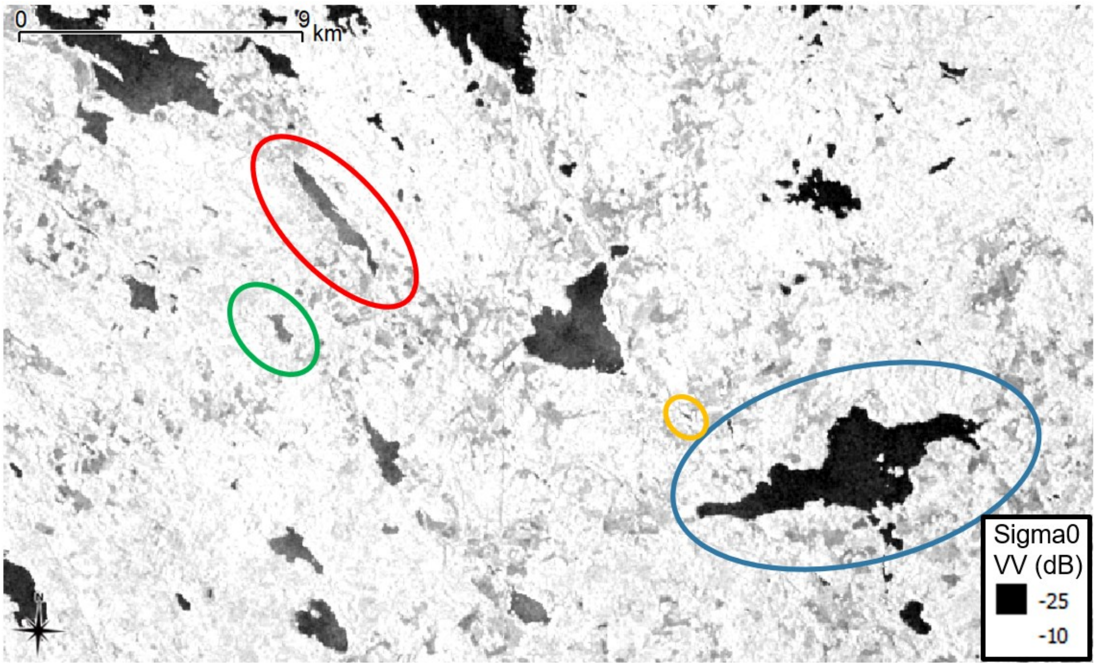

Figure 65 *Lake study area in a Sentinel-1 radar image from 25.7.2017, around 16:00 UTC. Red ellipse indicates lake Suolijärvi, blue ellipse Pääjärvi, green ellipse Pannujärvi and yellow ellipse lake Lovojärvi.*

It is presumed that this was a local weather phenomenon of a diameter of 10-20 kilometres affecting lake surface backscattering. Lakes on the northern, eastern and western sides of the study area seem less affected, with considerably lower backscattering in relation to Suolijärvi and Pannujärvi. Possibilities of both wind and rain, and rain clouds, could be suggested for causing the phenomena.

In order to assess the possibility of rain that day, no rain was measured by the local stations during the period of flyover, occurring 16:05 UTC. Light rain of 1.8 mm/h was observed by the Hämeenlinna Katinen station, closest one to the area measuring rain intensity, later that day at 16:40 UTC. Rain radar data was not openly accessible from FMI for summer 2017, as the date of analysis in May 2018 exceeded the radar data availability of 6 days, nor were the reference measurements at that point yet begun at lake Pannujärvi. Therefore, it is inconclusive if rain was a contributor in this outlier.

In case local difference in wind speed, wind direction or both were the cause of the phenomena seen in the radar image, it would have changed the waves and therefore radar backscattering of affected lakes. A difference in wind direction could also change the backscattering via direction of waterbody waves and therefore Bragg scattering in relation to the range-direction of the SAR sensor.

There are no wind observations conducted within the affected region shown in the radar image (Fig. 65). Therefore, the phenomenon cannot be measured with the used interpolation method using data from the two closest weather stations conducting wind observations, located around 20 km to north-east and 20 km south-west from Pannujärvi. Comparing interpolated values for lake Pannujärvi and Pääjärvi as a reference, the difference in gust speed and wind speed were close to equal, around 3.2 m/s and 1.6 m/s respectively for both lakes. Lake Pääjärvi wind direction was calculated to be around 2 degrees and for lake Pannujärvi 27 degrees.

Another outlier was identified on lake Suolijärvi on 13.8.2017, around 16:00 UTC (Fig. 66). This unexpected peak in difference values was not detected in other lakes, meaning the phenomenon is more likely local than the outlier on 25.7.2017 analysed previously. A speckle-filtered radar image with pixel spacing of 10 meters can be seen in figure 66. An area of high backscattering has appeared on lake Suolijärvi, sigma0 backscattering being around -12…-16 dB as compared to other lakes in the area and southern end of Suolijärvi being around -18…-20 dB.

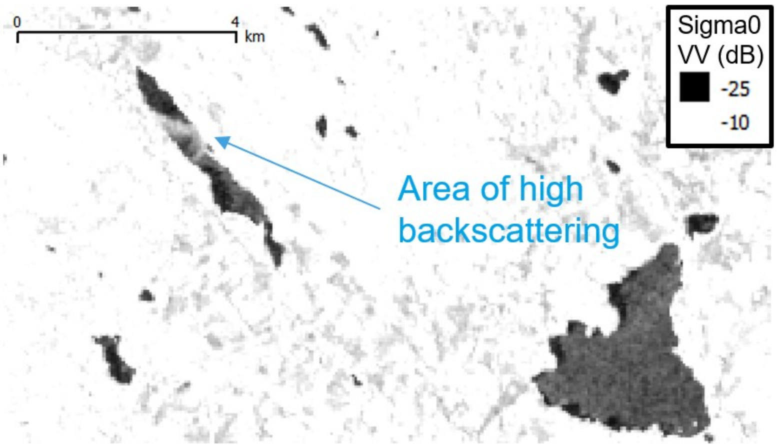

Figure 66 *Portion of the lake study area in a Sentinel-1 radar image from 13.8.2017, around 16:00 UTC. The possible area caused by local rain or raincloud is shown for lake Suolijärvi.*

The area of high backscattering does not appear on any of the other lakes within the study area, supporting the assessment that this is an outlier only found in lake Suolijärvi. Localized weather phenomena such as a downdraft of a thunderstorm, a cloud of rain or rain impacting the water – or a combination such factors – are suggested as the main cause.

Rain is certainly a possibility, as comparing Hämeenlinna Katinen rain observations during that period do indicate moderate rain around Hämeenlinna city, with 16:00 observation showing 11.9 mm/h rain intensity. Rain observations are higher in intensity and occur more often when compared to observations of the previous outlier analysed on 25.7.2017. The distance between the station is however more than 20 kilometres, only indicating that localized rainfall was possible in the nearby region during that day. Radar images were again not available for analysis due to the 6-day limitation in open access availability.

It is preferable to filter outliers, as an outlier value will impact both the radar image correlation and raster average difference being analysed, (r_A, d_A), and the corresponding values in for the similar raster images (r_B, d_B) seen in Eq. (30). In case these occur within the temporal averaged window near the freeze-up or break-up, it could cause an offset to ice freeze-up or break-up periods. Filtering of values in matrices R_B and D_B from Eq. (28) and Eq. (29) could be done by simple thresholds, with higher correlation values in D_B and lower average raster difference values in R_B being preferred.

Above filtering method cannot be applied to R_A and D_A, or (r_A, d_A) values as they are the correlation and average raster difference of the radar image compared to summer open water values and an offset between the values is being used in the method itself. Localized wind and showers are not accurately determined from using weather station observations, as their distance between them is usually tens of kilometres. For future works, it is suggested weather radar data to be studied for investigating outliers caused by rain and localized wind abnormalities.

5.2 Differences in the two river portions

For analysing the differences in the ice break-up of the two portions of Kokemäenjoki, an optical Sentinel-2 satellite image acquired in April 2018 is shown in appendix 5 showing close-ups of portions A and B separately. Comparing the two portions shows that portion B has only partially thawed, while portion A has fully thawed.

The above observation of different break-up dates does indicate that it is possible for portion B to fully thaw later than portion A, supporting the results where portion B break-up was also calculated to occur later than portion A for each studied year. As the TDD's for each years' break-up vary more for portion B as compared to portion A, it is either possible that this is contributed to inaccuracies in the method, or to a phenomenon during break-up is present for portion B but not portion A. The possibility of partial thawing affecting the accuracy of the method also cannot be excluded.

There were false detections of freezing over the course of summers 2015 and 2016 for portion B, which could not be attributed to partially frozen waterbodies. It is possible that a closer proximity to sea causes high sea waves to traverse to the portion B, or the wind field changes in such a fashion that the used method of interpolation does not match actual similarity in radar images. The two areas are also located in vastly different environments, where portion A located inland has manmade structures and fields surrounding it and portion B is in wetland. These result in wind sheltering effect to likely differ considerably between the areas.

5.3 Identifying limitations and improvements of the method

As the method compares radar images for regions of waterbodies instead of pixels, the method is sensitive to any changes in waterbodies. Even a partially frozen waterbody is likely to be identified as frozen, an example seen in section 5.1.1 explaining plausible differences in the two river portions. The method should therefore be considered sensitive to the timing of beginning of the freeze-up period, the freezing date, and similarly when the whole waterbody has become open water, the clear of ice date. As an example, if the outer area of Pääjärvi were to be frozen on one side and still being open water on the other, the lake is more likely to be estimated as frozen than open water. Within the scope of this thesis a scenario would be possible where the location of lake Pääjärvi ice thickness measurements is frozen while a vast majority of the rest of the lake is not.

One important limitation to consider is the possible occurrence of similar backscattering is featured by a waterbody surface both when frozen and not frozen and wind conditions are matched. This would result in that specific radar image to be misclassified. This phenomenon was not studied in this thesis, meaning the likelihood of occurrences at different incidence angles, waterbodies and wind speeds could be studied in the future and for developing suitable methods for filtering. Additionally, necessity of filtering of waterbodies falling under Sentinel-1 noise floor should be studied, as it is a possibility that waterbodies near or below the noise floor are more likely to be similar between open water and ice or snow at a wider range of similar wind conditions.

For lake Pääjärvi, the method was found to be limited in estimation of freezing and thawing for internal parts of the lake. It is therefore presumed that the wind sheltering effect near the shorelines is of importance to the method to work correctly. This effect could be studied in more detail by splitting studied waterbodies to multiple separate or overlapping areas horizontally and vertically in a fashion that shoreline is present in each. Also, as a relatively large 50-meter negative buffer was used for buffered lakes, this distance could potentially be reduced for lakes as with the 30 meters used for rivers. As calm water features homogenous low backscattering and thick shoreline vegetation or land a higher backscattering, the buffered area for each waterbody could be potentially be fine-tuned from using radar images from periods where water height is at minimum and shoreline vegetation at its thickest during late-summer.

As the freeze-up and break-up in the internal parts of a lake Pääjärvi were not suited to be estimated by the presented method, more robust methods could be developed for estimating the spatial ice phenology of lakes either medium size or larger IW-mode. As EW-mode of Sentinel-1 is used for operative ice mapping of the Baltic sea, it would be of interest to study to cover such larger lakes, though not processed using the method as presented in this thesis. The limitations of EW-mode are still to be considered the lower acquisition rate, no seasonal coverage whatsoever in some parts of Finland and late beginning of satellite acquisitions on autumn.

Fixed temporal averaging window size could contribute to offsets in freeze-up and break-up dates, where the satellite acquisition interval changes considerably. As the interval of radar images was generally lower during summer than during winter, this led to the summer difference values being over-represented in the temporal average window against the higher winter values. For the above scenario, this would cause freeze-up to be estimated late and break-up early – possibly at least partially explaining the similarly occurred offsets for lake Suolijärvi results for the freeze-up. Therefore, the averaging method used for filtering outliers could be improved or alternative methods used from the one described in this thesis.

Additionally, fixed temporal filter window caused misclassifications for most studied waterbodies when the acquisition interval exceeded the window size, especially throughout winter 2015-2016 since Sentinel-1B was not yet operational. Due to the fixed window size, the outlier-filtering effect of the average filter did not function as intended since as few as a single radar image were used to determine the ice phenology. For improving the filtering, it is possible that the temporal filter window size could vary in size by set rules, or certain portions of the acquisitions not meeting quality requirements could be excluded from the method.

If wind sheltering around a waterbody is changed seasonally, this would change the waves detected in radar images as well. These could be categorized as seasonal changes due to vegetation, such as deciduous trees shedding leaves, and other factors such as snow covering the surrounding areas prior to freeze-up or after break-up. In case a waterbody's waves are not similar in similar wind conditions over late changes occurring before ice break-up in autumn or the wind conditions remain inconsistent after ice break-up, this would result the break-up to be estimated too early and break-up too late. As around half of lake Suolijärvi break-ups were estimated too late, possibly explained by this phenomenon, it is of high interest to be studied in the future.

Non-seasonal changes in wind sheltering could also be considered. As a maximum difference of nearly four years exists between the first radar images and the last ones studied in this thesis, a possibility exists of rapid changes in vegetation such as logging, building or other structures affecting the wind near the studied waterbodies. Slowly occurring natural changes such as forest growth could also occur over time, though likely not prevalent in this study. Preference over selection of either lowest possible threshold of wind similarity as compared to less similar wind conditions from adjacent seasons could be studied in the future.

Accuracy of the interpolation method used to determine similar wind conditions is a key factor in the method. Though it was shown that similar wind conditions in the interpolated FMI weather station data resulted in the similarity in local measurements using the sensor station data, the interpolation method presented in this thesis has limitations leading to inaccuracies such as interpolating wind speed, gust speed and direction separately and not taking into accord the wind as a flow-field. In addition, one could take the wind conditions both before and after the acquisition of the radar image into accord, and for larger lakes apply a more robust raster sampling method than the applied nearest neighbour using waterbody polygon-centroids. The numerical estimation of wind similarity could potentially be fine-tuned with the radar image similarity of waterbodies over open water periods.

A phenomenon of multiple freeze-ups and break-ups in small lakes was observed in lake Pannujärvi measurement station and recorded in the lake ice observations of lake Suolijärvi. For Pannujärvi, these events occurred fast enough not to be seen in radar images over 2017-2018 winter, but for Suolijärvi these were visible in radar images and registered as a brief freeze-up and break-up cycle in for 2016 autumn. Short periods of temporary seasonal ice occurring between satellite flyovers would have no effect to the method. However, if such events are captured in one or more radar images in short succession, they can potentially cause an offset to the freeze-up and break-up periods. Decreasing the window size of temporal averaging will enable these events to be detected more easily, but filtering effect of outliers is reduced. Use of air temperature data to distinguish between outliers and short frozen periods could be studied in the future.

The results for very small waterbodies such as lake Lovojärvi included in the thesis, could be affected by the low number of pixels after resampling – lake Lovojärvi in total had 4 pixels used in the method. As radar images are masked at 10 × 10-meter pixel spacing and then resampled to 50 × 50 meters, this will result in some resampled pixels to be a mean of a varying number of 10 × 10-meter pixels, without being weighted when correlation and averaged raster difference are calculated. Therefore, alternative resampling resolutions for small lakes could be studied in the future, such as the 30 × 30-meter resolution used for the river study area with relatively good results.

Since only four lakes and two river portions were studied in this thesis, it would be necessary to study the accuracy of the method for a larger sample of waterbodies featuring a variety of different sizes and shapes. As an example, none of the waterbodies in this thesis had highly irregular outer shapes or notable amounts of islands. These waterbodies would preferably feature manual ice phenology observations, and when studying very small to small lakes few of which manual observations are being conducted, ice break-up could be studied using optical Sentinel-2 and Landsat data over one or several springs where the break-up period is mostly cloud-free.

Alternatives and improvements for the numerical comparison between rasters, currently using correlation and averaged raster values, could be studied. As an example, additional similarities between open water surfaces and dissimilarities between open water and frozen surfaces could potentially be found from the radar image texture via grey-level co-occurrence matrix, as studied by Karvonen (2017) using EW-mode in sea ice classification. For studying the optimal method of determining the similarity between rasters, expansion from current study areas and using a number different of waterbodies with more variation in size, shape and type is suggested. Alternative variants of data normalization for relative orbits and introduction of VH-polarity rasters to the method could be studied as well.

Regarding the amount of processing involved in the method, the current method calculates correlation, raster average difference and wind difference between each radar image of which some are not necessary to determine ice phenology. Though done in this thesis for demonstrating the effectiveness of the method, after estimating freeze-up and break-up dates for each winter it is not necessary to calculate additional values during summer or winter when it is known that a waterbody is either thawed or frozen. As an example, knowing the TDD or FDD from previous years to relatively good accuracy could be used to narrow down the time being analysed by the presented method. Additionally, to save storage space, radar images that do not have corresponding similar wind conditions could be left out even prior to radar data pre-processing.

5.4 Advantages and potential applications of the method

In several methods developed for classifying between open water and lake ice using backscattering from spaceborne SAR on C-band, the distinction between calm water and new lake ice was found to be difficult due to both being similar in being backscattering. Both feature similar, weak backscattering signal due to being specular reflectors, with the signal falling routinely below respective spaceborne SAR's noise floor (e.g. Sobiech & Dierking 2013, Surdu et al. 2015). Additionally, as cross-polarities such as VH routinely fall below the noise floor for waterbodies at most incidence angles, this will limit the above methods to only using co-polarized VV or HH for classification (Jackson & Apel 2005).

As small to very small lakes can be completely calm, they cannot be reliably classified as either ice or open water for low wind speeds using the above methods. At medium wind speeds, especially below the VH-noise floor, the co-polarity backscattering between open water and frozen lake surface at different parts of a waterbody due to wind sheltering could be near identical resulting in misclassification between the two. Averaging the backscattering for a whole waterbody and then comparing the value with the wind speed would still provide varying results, as areas of high backscattering due to Bragg-scattering and low backscattering due to wind sheltering would vary by the wind direction for the waterbody.

The developed method does overcome the limitations stated above for the most part. Misclassification can be considered possible for the method at low wind speeds where wind sheltering does not create reproducible spatial variation in radar images, occurring only in circumstances where both the compared frozen surface and open water surface are nearly identical during matching wind speeds. At medium and high wind speeds the spatial variation due to wind sheltering does result in circumstances that are rarely reproduced in frozen surfaces – such as the side opposing the wind having routinely lower backscattering than the central areas. In comparison, additional advantages of the developed method can be listed as the ability to use portions of radar images falling even below co-polarities' noise floor at low incidence angles, as this increases the number of relative orbit acquisitions usable for each waterbody.

Provided the improvements for future development presented for the method, its applicability to operational use in Finland is attributed to five factors.

- The method was found to be applicable for a wide size range of different waterbodies, including river portions and very small lakes
- The method does not require manual processing steps provided the input data quality, such as buffered waterbody areas, is sufficient
- Sentinel-1 IW-mode temporal coverage was found to be high enough to be used by the method in southern Finland, while increasing even further in northern Finland
- The method was found to be able to estimate ice phenology for any winter since satellite acquisitions begun
- Unlike optical sensors, Sentinel-1 data is independent from solar illumination. It enables the detection of freezing event which typically occurs during polar darkness at high latitudes. Likewise, the possible cloud cover does not prevent the Sentinel-1 observations, enabling the effective monitoring of lake/rive ice status

These five factors in combination mean that the method could be used to calculate the beginning of freeze-up and free of ice dates of a vast number of waterbodies, including sufficiently wide portions of rivers and lakes between very small to medium in size. As was found in the report by J. Korhonen (2005), there is a statistically significant correlation between the freeze-up, break-up dates and latitude. Lakes nearly identical in their properties such as area and depth in the same latitude can be expected to freeze and thaw around the same time. By categorizing these lakes by their properties and latitude, one could both distinguish trends related to degree-days and better find incorrectly determined ice phenology dates. For additional improvements, instead of latitudes one could use numerical modelling for the heat fluxes affecting lakes, their thermal insulation and solar flux reflection by snow layer and accumulated ice thickness over the winter, as an example stated by Martynov et al. (2010) in their work.

For numerical models such as CLIME (Leppäranta 2009), being able to determine how air temperature affects timings of freezing – melting events for different lakes would be beneficial in improving the accuracy of the model. It is however also seen that certain modelled phenomena by CLIME, such as mechanical ice-breakage due to wind exposing open water areas in lakes, cannot be detected by the method, as it is not able to distinguish a partially frozen lake from a fully frozen lake.

Since the WSFS system is used in Finland for watershed modelling includes ice break-up forecasting for select waterbodies featuring historical break-up observations (Vehviläinen & Huttunen 2001), one application of the method-calculated freeze-ups is to supply necessary observation data to apply forecasting for waterbodies, or parts of them, without observations. Timing of river ice break-up affects river flooding (Helama et al. 2013), so monitoring and forecasting for such events could be a potential – and very needed – application for the method as it is able to determine when inland river portions become free of ice. It is also to be noted that WSFS watershed models and their calibration data is affected by seasonal lake and river ice (Vehviläinen 1994), so the application of wide-scale freeze-up and break-up data could be studied in relation with WSFS.

Since the timing of snow onset on new lake ice has been found to have a great impact on the early ice thickness accumulation rate in the work by Yang et al. (2012) using HIGHTSI model for lake Vanajavesi, it is a possibility that the timing of freeze-ups for various waterbodies could be used for ice thickness estimates and forecasting using the WSFS. Ice thicknesses calculated by the WSFS in turn are currently used by various users for as an example determining the safety of ice for pedestrian and ice road use.

6 Conclusion

A method for estimating waterbody freeze-up and break-up dates using both in-situ weather station measurements and Sentinel-1 radar images was presented in this thesis, based on the phenomenon where nearly identical wind conditions produce similar wave conditions in waterbodies. Wave similarity is estimated using Sentinel-1 IW-mode radar images and wind conditions being assessed through weather station observations.

A sensor station was set up at one of the studied lakes for collecting detailed data in preparation for the thesis. The images and local wind data collected were used to ascertain the proposed similarity waterbody waves in similar wind conditions, and to accurately determine ice phenology dates of the lake. Overall, wind sheltering effect near waterbody shorelines produced by vegetation and manmade structures around waterbodies is very likely to feature a key role in the similarity of waves in similar wave conditions.

Based on a limited amount of accurate observation samples for comparison for lake Pannujärvi and lake Suolijärvi, more than half of the determined ice phenology dates indicated the freeze-up and break-up period either fully correctly or within one flyover of the satellite. Some misclassifications of ice phenology occurred during winters for all waterbodies, while open water classification during open water period was consistent with the exception of only a few waterbodies.

The method was found to be both limited in both distinguishing between partially frozen and fully frozen waterbodies, and in estimating the freeze-up and break-up of inner areas of lakes of medium size and larger. Several improvements and suggestions for future development were introduced, such as noting the importance of using a more accurate method of wind interpolation, along with listing likely sources of outliers such abnormal weather conditions introducing various ways how these could be filtered. Expanding the number of different waterbodies with accurate observations analysed by the method is suggested in case the method is further developed.

The major advantages of the method were found to be the capability of using most of the incidence angle range featured in Sentinel-1 radar images and the being able to combine radar images from different relative orbits for a high temporal frequency of ice phenology determination. Freeze-up and break-up dates can also be calculated since the beginning of Sentinel-1 acquisitions. The method should also become more accurate as more radar images are collected, since more similar wind conditions can be found between compared radar images. As examples of the potential applications of the method, the freeze-up and break-up dates of very small to medium size lakes could be used in lake ice and watershed models without the need for manual observations, while estimating river ice break-up dates can be used in improving forecasting of river ice break-up and flooding.

7 References

Ali, I. et al., 2018. Methods to Remove the Border Noise From Sentinel-1 Synthetic Aperture Radar Data: Implications and Importance For Time-Series Analysis. *IEEE Journal of Selected Topics in Applied Earth Observations and Remote Sensing*, 11(3), pp.777-86.

Alpers, W. et al., 2016. Rain footprints on C-band synthetic aperture radar images of the ocean - Revisited. *Remote Sensing of Environment*, 187, pp.169-85.

Andre, D., Hill, R.D. & Moate, C.P., 2008. Multipath simulation and removal from SAR imagery. *Proceedings of SPIE, 2008*. ResearchGate.

Armstrong, M.P. & Marciano, R., 1994. Inverse-Distance-Weighted Spatial Interpolation Using Parallel Supercomputers. *Photogrammetric Engineering and Remote Sensing*, 60(9), pp.1097-103.

Ashton, G.D., 1989. Thin Ice Growth. *Water Resources Research*, 25(3), pp.564-66.

Aurthur, R.S., 1951. The effect of Islands on Surface Waves. *Bulletin of the Scripps Institution of Oceanography of the University of California*, 6(1), pp.1-26.

Barton, D.K., 2005. *Radar System Analysis and Modelling*. 1st ed. Norwood: Arttech House, Inc.

Bilello, M.A., 1980. *Maximum Thickness and Subsequent Decay of Lake, River, and Fast Sea Ice in Canada and Alaska*. CRREL Report 80-6.

Bourbigot, M., Johnsen, H. & Piantanida, R., 2016. *Sentinel-1 Product Definition*. European Space Agency.

Brockmann, C. & Fomferra, N., 2015. *SNAP - The Sentinels Application Platform*. ESA ESRIN.

Campbell, J.B. & Wynne, R.H., 2011. *Introduction to Remote Sensing*. 5th ed. New York: Springer.

Charnock, H., 1955. Wind stress on a water surface. *Quarterly Journal of the Royal Meteorological Society*, 81(350), pp.639-40.

De Zan, F. & Guarnieri, A.M., 2006. TOPSAR: Terrain Observation by Progressive Scans. *IEEE Transactions on Geoscience and Remote Sensing*, 44(9), pp.2352-60.

Dierking, W., Carlström, A. & Ulander, L.M.H., 1997. The Effect of Inhomogeneous Roughness on Radar Backscattering from Slightly Deformed Sea Ice. *IEEE Transactions on Geoscience and Remote Sensing*, 35(1), pp.147-59.

Doerry, A.W. & Dickey, F.M., 2004. Synthetic Aperture Radar. *Optics and Photonics News*, 15(11), pp.28-33.

Duguay, Y., Bernier, M., Lévesque, E. & Tremblay, B., 2015. Potential of C and X Band SAR for Shrub Growth Monitoring in Sub-Arctic Environments. *Remote Sensing*, 7(7), pp.9410-30.

Du, J. et al., 2017. Satellite microwave assessment of Northern Hemisphere lake ice phenology from 2002 to 2015. *The Cryosphere*, 11(47), pp.47-63.

Ekholm, P., 1992. Reversibly absorbed phosphorus in agriculturally loaded rivers in southern Finland. *Aqua Fennica*, (22), pp.35-41.

ELY-keskus, kalatalouspalvelut, 2018. *Kokemäenjoki*. [Online] Available at: http://www.kokemaenjoki.fi/etusivu/kokemaenjoki [Accessed 15 September 2018].

Engman, E.T., 1993. *Handbook of Hydrology Chapter 24 - Remote Sensing*. 1st ed. McGraw-Hill.

ESA, 2007. *Sentinel-1, The Radar Mission for GMES Operational Land and Sea Services*. European Space Agency.

ESA, 2012. *Sentinel-1 - ESA's Radar Observatory Mission for GMES Operational Services*. Noordwijk: European Space Agency.

ESA, 2018. *Radar Course II*. [Online] Available at: https://earth.esa.int/web/guest/missions/esa-operational-eo-missions/ers/instruments/sar/applications/radar-courses [Accessed 15 September 2018].

Foumelis, M., 2015. *6th ESA Advanced Training Course on Land Remote Sensing - Sentinel-1 Toolbox RGB Composite for Land Cover/Use Monitoring*. Bucharest.

Franceschetti, G. & Lanari, R., 1999. *Synthetic Aperture Radar Processing*. 1st ed. CRC Press.

Gade, M., 2015. Synthetic Aperture Radar Applications in Coastal Waters. Varna, Bulgaria, 2015.

Geldsetzer, T., 2010. *Mapping and monitoring lake ice using SAR Satellites*. CCRS.

Goldman, C.R. & Horne, A.J., 1983. *Limnology*. 1st ed. New York: McGraw-Hill College.

Greer, J.D., 1975. Ground Dimension from Slant-Range Radar. *Photogrammetric engineering and remote sensing*, 41(8), pp.1043-46.

Greidanus, H. & Santamaria, C., 2014. *First Analyses of Sentinel-1 Images for Maritime Surveillance*. Ispra, Italy: European Commission.

Guarnieri, A.M., Mancon, S. & Tebaldini, S., 2015. SENTINEL-1 PRECISE ORBIT CALIBRATION AND VALIDATION., 2015. ResearchGate.

Hajduch, G., 2018. *Masking "No-value" Pixels on GRD Products generated by the Sentinel-1 ESA IPF*. ESA Mission Operating Centre.

Helama, S. et al., 2013. Quantifying temporal changes in Tornionjoki river ice breakup dates and spring temperatures in Lapland since 1802. *Journal of Geographical Sciences*, 23(6), pp.1069-79.

Helminen, M.&.a., 1977. *Suomen luonnon tietosanakirja*. Helsinki: Oy Valitut Palat Reader's Digest Ab.

Henderson, F.M. & Lewis, A.J., 1998. *Principles and Applications of Imaging Radar*. 3rd ed. Wiley.

Hindberg, H. & Eirik, M., 2013. Mapping of Lake Ice in Northern Europe Using Dual-Polarization Radarsat-2 Data. Edinburgh, 2013.

Hristov, T.S., Miller, S.D. & Friehe, C.A., 2003. Dynamical coupling of wind and ocean waves through wave-induced air flow. *Nature*, 422(1), pp.55-58.

Isleifson, D. et al., 2010. C-Band Polarimetric Backscattering Signatures of Newly Formed Sea Ice During Fall Freeze-Up. *IEEE Transactions on Geoscience and Remote Sensing*, 48(8), pp.3256-67.

Jackson, C.R. & Apel, J.R., 2005. *Synthetic Aperture Radar Marine User's Manual*. NOAA/NESDIS.

Jeffries, M.O., Wakabayashi, H. & Weeks, W.F., 1993. ERS-1 SAR Backscatter Associated WIth Ice Growth on Shallow Lakes in Arctic Alaska. Tokyo, 1993. IEEE.

Johannessen, J.A. & Collard, F., 2013. *SAR Instrument Principles and Processing*. 3rd ESA Advanced Training on Ocean Remote Sensing Presentations.

Järnefelt, H., 1958. *Vesiemme luonnontalous*. Porvoo.

Karvonen, J., 2017. Baltic Sea Ice Concentration Estimation Using Sentinel-1 SAR and AMSR2 Microwave Radiometer Data. *IEEE Transactions on Geoscience and Remote Sensing*, 55(5), pp.2871-83.

Kellndorfer, J.M., Pierce, L.E., Dobson, M.C. & Ulaby, F.T., 1998. Toward consistent regional-to-global-scale vegetation characterization using orbital SAR systems. *IEEE Transactions on Geoscience and Remote Sensing*, 36, pp.1396-411.

Kettunen, I., Mäkelä, A. & Heinonen, P., 2008. *Vesistötietoa näytteenottajalle*.

Korhonen, J., 2005. *Suomen vesistöjen jääolot*. Helsinki: Finnish Environment Institute.

Kärkäs, E., 2000. The Ice Season of Lake Pääjärvi in Southern Finland. *Geophysica*, 36(1-2), pp.85-94.

Laasanen, O., 1982. *Freeze-up, Break-up, Ice-thickness and Surface Water Temperature Statistics in Lakes and Rivers in Finland*. Helsinki: National Board of Waters.

Lake and Sea Wiki, 2018. *Lake and Sea Wiki*. [Online] Available at: https://www.jarviwiki.fi/ [Accessed 15 September 2018].

Laur, H. et al., 2004. *Derivation of the Backscattering Coefficent σo in ESA ERS SAR PRI Products*. European Space Agency.

Lee, J.S. et al., 1994. Speckle filtering of synthetic aperture radar images: A Review. *Remote Sensing Reviews*, 8(4), pp.313-40.

Leppäranta, M., 2009. Modelling the Formation and Decay of Lake Ice. In *The Impact of Climate Change on European Lakes*. Springer Science+Business Media B.V. pp.63-83.

Leppäranta, M., 2015. *Freezing of Lakes and the Evolution of their Ice Cover*. 1st ed. Berlin: Springer.

Leppäranta, M., Virta, J. & Huttula, T., 2017. *Hydrologian perusteet*. 1st ed. Helsinki: Helsingin yliopisto.

López-Martinez, C., Ferro-Famil, L. & Pottier, E., 2015. *Polarimetry Tutorial*. European Space Agency.

Los, H. et al., 2016. Comparison of C-Band and X-Band Polarimetric SAR Data for River Ice Classification on the Peace River. Prague, 2016.

Louis, D.B., 1986. World Geodetic System 1984. Austin, 1986. Defence Mapping Agency Aerospace Center.

Maidment, D.R., 1993. *Handbook of Hydrology*. 1st ed. McGraw-Hill, Inc.

Markfort, C.D. et al., 2010. Wind sheltering of a lake by a tree canopy or bluff topography. *Water Resources Research*, 46(3).

Markfort, C.D. et al., 2012. Wind Sheltering of Small Lakes by Complex Terrain. Boston, 2012.

Martynov, A., Sushama, L. & Laprise, R., 2010. Simulation of temperate freezing lakes by one-dimensional lake models: performance assessment for interactive coupling with regional climate models. *Boreal Environment Research*, 15, pp.143-64.

McCandless, S. & Jackson, C., 2004. Principles of Synthetic Aperture Radar. In *Synthetic Aperture Radar Marine User's Manual*. Washington DC: NOAA NESDIS Office of Research and Applications. pp.1-24.

Miranda, N. & Rosich, N., 2011. *Sentinel-1 Processor and Core Product Presentation*. Frascati: ESA.

Moreira, A. et al., 2013. A Tutorial on Synthetic Aperture Radar. *IEEE Geoscience and Remote Sensing Magazine*, 1(1), pp.6-43.

Mott, H., 2007. *Remote Sensing with Polarimetric Radar*. 1st ed. Hoboken, New Jersey: John Wiley & Sons.

Mäkelä, S., 2016. *Pakka-hanke, Yleisötilaisuus*. Hämeenlinna: Vanajavesikeskus.

Nghiem, S.V. & Leshkevich, G.A., 2007. Satellite SAR Remote Sensing of Great Lakes Ice Cover, Part 1. Ice Backscatter Signatures at C-Band. *Journal of Great Lakes Research*, 33(4), pp.722-35.

Ohata, Y., Toyota, T. & Fraser, A.D., 2017. The role of snow in the thickening processes of lake ice at Labe Abashiri, Hokkaido, Japan. *Tellus A: Dynamic Meteorology and Oceanography*, 69(1).

Palomino, I. & Martin, F., 1994. A Simple Method for Spatial Interpolation of the Wind in Complex Terrain. *Journal of Applied Meteorology*, 34, pp.1678-93.

Paquier, A., Moisy, F. & Rabaud, M., 2016. Viscosity effects in wind wave generation. *Physical Review Fluids*, 1(8), pp.83901-16.

Park, J.W., Korosov, A. & Babiker, M., 2017. Efficient thermal noise removal of Sentinel-1 image and its impacts on sea ice applications. Vienna, 2017.

Petersen, J.F., Sack, D. & Gabler, R.E., 2016. *Physical Geography*. 11th ed. Cengage Learning.

Phan, X.V. et al., 2014. 1D-Var multilayer assimilation of X-band SAR data into a detailed snowpack model. *The Cryosphere*, 8(5), pp.1975-87.

Piirinen, P. et al., 2012. *Tilastoja Suomen ilmastosta 1981-2010*. Helsinki: Finnish Meteorological Institute.

Raatikainen, M. & Kuusisto, E., 1990. Suomen järvien lukumäärä ja pinta-ala. *Terra (Helsinki, Finland)*, pp.97-110.

Rabus, B., Eineder, M., Roth, A. & Bamler, R., 2002. The shuttle radar topography mission—a new class of digital elevation models acquired by spaceborne radar. *ISPRS Journal of Photogrammetry & Remote Sensing*, 57, pp.241-62.

Richard, J.A., 2008. *Radio Wave Propagation*. 1st ed. Berlin: Springer.

RLS Energy, 2018. *Adjusting Wind Speeds*. [Online] Available at: http://rlsenergy.com/products/wind-power/wind-speed-data/ [Accessed 15 September 2018].

Roberts, B.L., 1984, Rev. 2003. *The Decibel Scale*. Boston: Boston University, Department of Physics.

Saaranen, V. et al., 2006. The New Finnish Height System N2000. Espoo, 2006. ResearchGate.

Schwaizer, G., 2017. *ESA Training course - SAR / Optical Applications to Ice and Snow*. ESA.

Shi, J. et al., 2012. Processes on microwave remote sensing of land surface parameters. *Science China Earth Sciences*, 55(7), pp.1052-78.

Small, D. & Schubert, A., 2008. *Guide to ASAR Geocoding*. Zürich: ESA ESRIN.

Sobiech, J. & Dierking, W., 2013. Observing lake- and river-ice decay with SAR: advantages and limitations of the unsupervised k-means classification approach. *Annals of Glaciology*, 54(62), pp.65-72.

Surdu, C.M., Duguay, C.R., Pour, K.K. & Brown, L.C., 2015. Ice Freeze-up and Break-up Detection of Shallow Lakes in Northern Alaska with Spaceborne SAR. *Remote Sensing*, 7(5), pp.6133-59.

Särkkä, J., 1996. *Järvet ja Ympäristö - Limnologian perusteet*. 1st ed. Tampere: Gaudeamus Kirja.

Tammelin, B. et al., 2011. Production of Finnish Wind Atlas. *Wind Energy*, 16(1), pp.19-35.

Tedesco, M., 2014. *Remote Sensing of the Cryosphere*. John Wiley & Sons, Ltd.

Ulaby, F.T., Moore, R.K. & Fung, A.K., 1981. *Microwave Remote Sensing - Active and Passive, Volume I*. 1st ed. Massachussets: Addison-Wesley Publishing Company.

Wakabayashi, H. & Nishito, Y., 2015. Monitoring of Tundra Lakes with C-Band and L-Band SAR Data. Milan, Italy, 2015. IEEE.

Ward, P.R.B., 1979. Seiches, tides, and wind set-up on Lake Kariba. *Limnology & Oceanography*, 24(1), pp.151-57.

Vehviläinen, B., 1994. *The Watershed Simulation and Forecasting System in the National Board of Water and Environment*. Tammer-Paino.

Vehviläinen, B. & Huttunen, M., 2001. *Hydrological Forecasting and Real Time Monitoring in Finland: The Watershed Simulation and Forecasting System (WSFS)*. Helsinki: Finnish Environment Institute.

Vesilaki, 2011. *Finnish law*.

Wetzel, R., 1983. Periphyton of freshwater ecosystems. Växjö, 1983. Springer Netherlands.

Wiley, C., 1965. *Pulsed Doppler Radar Methods and Apparatus*. United States.

Vuola, P., 2013. *Porin tulvasuojelusta*. Porin kaupunki.

Yang, Y., Leppäranta, M., Cheng, B. & Zhijun, L., 2012. Numerical modelling of snow and ice thicknesses in Lake Vanajavesi, Finland. *Tellus A*, 64(1).

List of appendices

Appendix 1. Ice phenology determination method processing chain

Appendix 2. Pannujärvi measurement station power and network connection figures

Appendix 3. Suolijärvi ice phenology events 2014-2017 provided by Vanajavesikeskus

Appendix 4. Suolijärvi ice thickness observations 2014-2017, acquired from Finnish Environment Institute Hydrology API service

Appendix 5. April 2018 Sentinel-2 RGB composite for river study area portions

Appendix 1

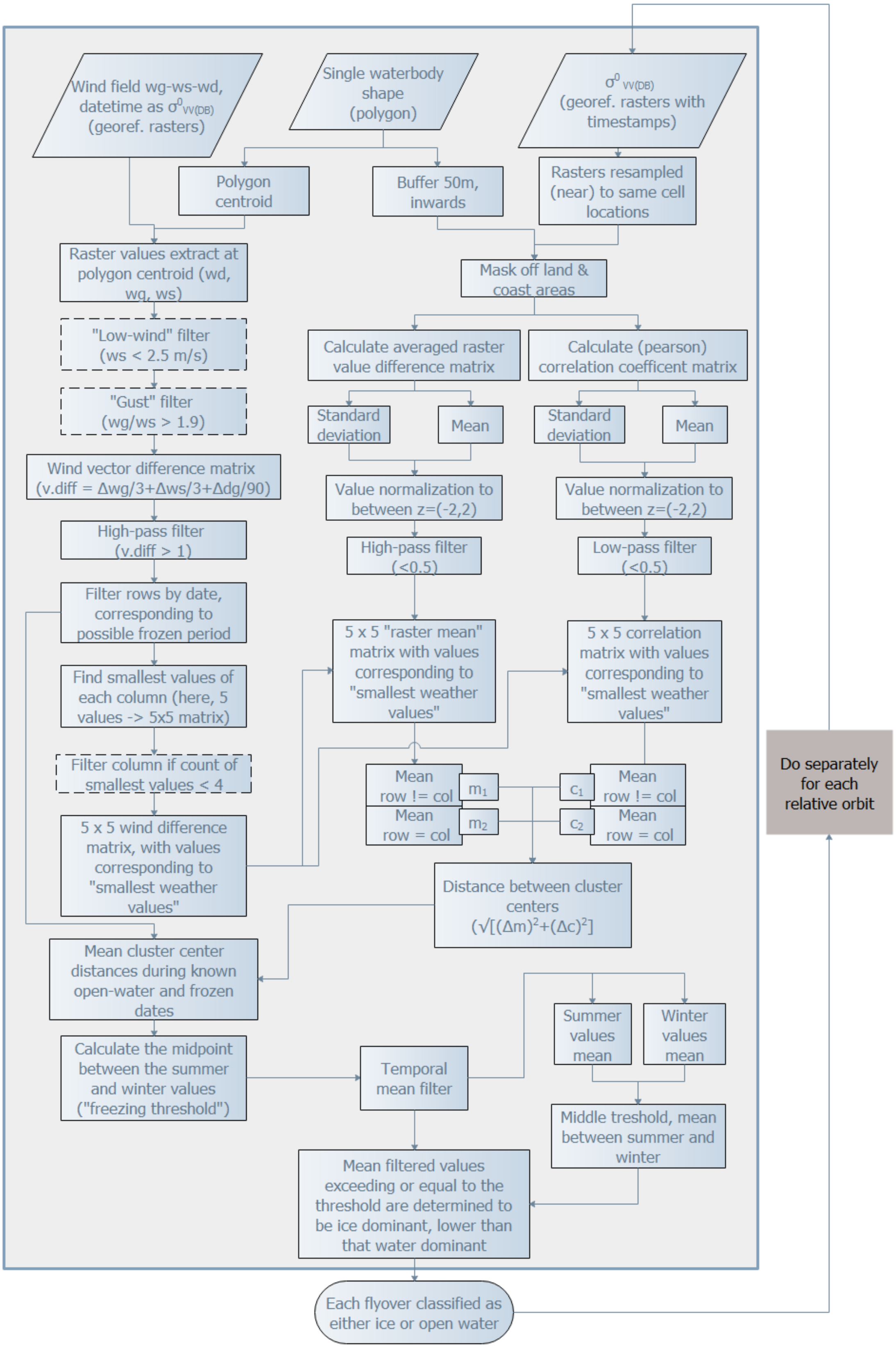
Wind field wg-ws-wd, datetime as $\sigma^0_{VV(DB)}$ (georef. rasters)
Single waterbody shape (polygon)
$\sigma^0_{VV(DB)}$ (georef. rasters with timestamps)
Polygon centroid
Buffer 50m, inwards
Rasters resampled (near) to same cell locations
Raster values extract at polygon centroid (wd, wg, ws)
Mask off land & coast areas
"Low-wind" filter (ws < 2.5 m/s)
"Gust" filter (wg/ws > 1.9)
Calculate averaged raster value difference matrix
Calculate (pearson) correlation coefficent matrix
Standard deviation
Mean
Standard deviation
Mean
Wind vector difference matrix (v.diff = Δwg/3+Δws/3+Δdg/90)
Value normalization to between z=(-2,2)
Value normalization to between z=(-2,2)
High-pass filter (v.diff > 1)
High-pass filter (<0.5)
Low-pass filter (<0.5)
Filter rows by date, corresponding to possible frozen period
5 x 5 "raster mean" matrix with values corresponding to "smallest weather values"
5 x 5 correlation matrix with values corresponding to "smallest weather values"
Find smallest values of each column (here, 5 values -> 5x5 matrix)
Filter column if count of smallest values < 4
Mean row != col
m_1
c_1
Mean row != col
Mean row = col
m_2
c_2
Mean row = col
5 x 5 wind difference matrix, with values corresponding to "smallest weather values"
Distance between cluster centers ($\sqrt{[(\Delta m)^2+(\Delta c)^2]}$)
Do separately for each relative orbit
Mean cluster center distances during known open-water and frozen dates
Summer values mean
Winter values mean
Calculate the midpoint between the summer and winter values ("freezing threshold")
Temporal mean filter
Middle treshold, mean between summer and winter
Mean filtered values exceeding or equal to the threshold are determined to be ice dominant, lower than that water dominant
Each flyover classified as either ice or open water

Appendix 2

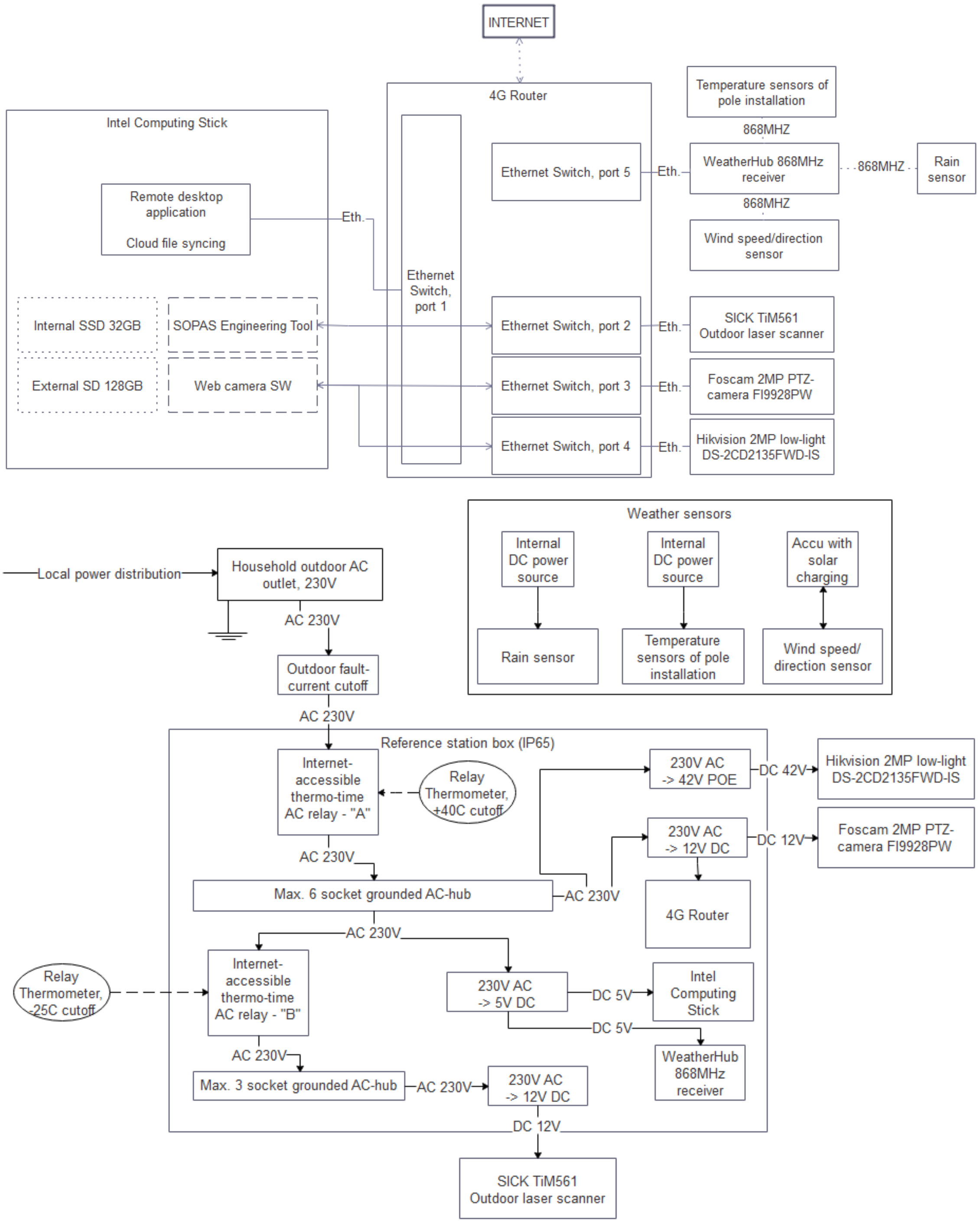
INTERNET
4G Router
Ethernet Switch, port 1
Ethernet Switch, port 5
Ethernet Switch, port 2
Ethernet Switch, port 3
Ethernet Switch, port 4
Intel Computing Stick
Remote desktop application
Cloud file syncing
Internal SSD 32GB
SOPAS Engineering Tool
External SD 128GB
Web camera SW
Eth.
Temperature sensors of pole installation
868MHZ
WeatherHub 868MHz receiver
868MHZ
Rain sensor
868MHZ
Wind speed/direction sensor
SICK TiM561 Outdoor laser scanner
Foscam 2MP PTZ-camera FI9928PW
Hikvision 2MP low-light DS-2CD2135FWD-IS
Weather sensors
Internal DC power source
Internal DC power source
Accu with solar charging
Rain sensor
Temperature sensors of pole installation
Wind speed/ direction sensor
Local power distribution
Household outdoor AC outlet, 230V
AC 230V
Outdoor fault-current cutoff
AC 230V
Reference station box (IP65)
Internet-accessible thermo-time AC relay - "A"
Relay Thermometer, +40C cutoff
AC 230V
Max. 6 socket grounded AC-hub
AC 230V
230V AC -> 42V POE
DC 42V
Hikvision 2MP low-light DS-2CD2135FWD-IS
230V AC -> 12V DC
DC 12V
Foscam 2MP PTZ-camera FI9928PW
4G Router
AC 230V
Relay Thermometer, -25C cutoff
Internet-accessible thermo-time AC relay - "B"
230V AC -> 5V DC
DC 5V
Intel Computing Stick
DC 5V
WeatherHub 868MHz receiver
AC 230V
Max. 3 socket grounded AC-hub
AC 230V
230V AC -> 12V DC
DC 12V
SICK TiM561 Outdoor laser scanner

Appendix 3

Winter	*Beginning of freeze-up period*	*End of freeze-up period*	*Beginning of break-up period*	*End of break-up period*	*Notes*
2014-2015	2014-12-21	2014-12-21	-	-	
2014-2015	-	-	2014-04-10	2014-04-11	
2015-2016	2015-12-15	2015-12-15	-	-	
2015-2016	-	-	2015-12-19	2015-12-19	
2015-2016	2015-12-28	2015-12-28	-	-	
2015-2016	-	-	2016-04-12	2016-04-12	
2016-2017	2016-11-11	2016-11-11	-	-	
2016-2017	-	-	2016-11-25	2016-11-25	
2016-2017	2016-11-29	2016-11-29	-	-	
2016-2017	-	-	2017-04-21	2017-04-21	
2017-2018	2017-11-04	2017-11-04	-	-	
2017-2018	-	-	2017-11-05	2017-11-09	
2017-2018	2017-12-06	2017-12-08	-	-	
2017-2018	-	-	2017-12-10	2017-12-10	Only partially thawed
2017-2018	2017-12-22	2017-12-22	-	-	

Appendix 4

2014-2015	*2015-2016*	*2016-2017*	*2017-2018*
30.12.2014	5.1.2016	13.12.2016	19.1.2018
10.1.2015	10.1.2016	30.12.2016	30.1.2018
20.1.2015	20.1.2016	10.1.2017	10.2.2018
30.1.2015	30.1.2016	20.1.2017	20.2.2018
10.2.2015	10.2.2016	30.1.2017	1.3.2018
20.2.2015	20.2.2016	10.2.2017	10.3.2018
28.2.2015	28.2.2016	20.2.2017	19.3.2018
10.3.2015	10.3.2016	28.2.2017	30.3.2018
20.3.2015	20.3.2016	10.3.2017	10.4.2018
31.3.2015	30.3.2016	20.3.2017	
10.4.2015		30.3.2017	
13.4.2015			

Appendix 5

The following Sentinel-2 image was downloaded from the ESA Open Access Portal, then processed into an RGB-composite using bands 2, 3 and 4 using ESA SNAP.

- S2B_MSIL2A_20180414T101019_N0207_R022_T34VEP_20180414T121058

River study area polygons for portion A and portion B were overlaid to the RGB-composites of the satellite images. Scale and north-arrow were added, and the view was exported using GIS software. These two views are shown below.